SEISMIC DEFORMATION ANALYSIS OF EARTH DAMS:

A SIMPLIFIED METHOD

Thesis by

Liping Yan

In Partial Fulfillment of the Requirements

for the Degree of Civil Engineer

California Institute of Technology

Pasadena, California

1992

(Submitted November 6, 1991)

ACKNOWLEDGEMENTS

This work was funded by the National Science Foundation under Grant No. ECE-8610887. The support from the National Science Foundation, Converse Scholarship and the California Institute of Technology is gratefully acknowledged.

ABSTRACT

Motivated by the dynamic behaviors of two earth dams, named La Villita Dam and El Infiernillo Dam in Mexico, during an earthquake on September 19, 1985, a seismic deformation analysis is elaborated in this study.

Firstly, a simplified method is developed by applying a rigid block model to study the major characteristics of an earth dam during an earthquake and calculate the seismic permanent displacements. In this method, the sliding mass is modeled as a rigid body along a well defined surface. Both inclined plane and circular arc slip surfaces are considered.

Secondly, in order to validate the numerical procedure of the simplified method and study the dynamic response of the rigid block on an inclined plane experimentally, shaking table tests are performed on the model used in the simplified method. Comprehensive numerical simulations are carried out with the computer programs developed, and comparisons with the test results are made.

Finally, applying the developed method to La Villita Dam and El Infiernillo Dam, seismic deformation analyses are carried out. In addition, an attempt to reproduce some of the motions recorded on La Villita Dam during the 1985 earthquake is made in this study.

TABLE OF CONTENTS

Page

LIST OF TABLES AND FIGURES

Chapter 1
INTRODUCTION

1.1 Motivation

An earthquake occurred off the Mexican coast on September 19, 1985. This earthquake not only caused extensive damage to buildings, especially in Mexico City (EEFIT, 1986), but also affected several dams, two of which were La Villita Dam and El Infiernillo Dam. An investigation of the behaviors of La Villita and El Infiernillo Dams during this earthquake led to this study on the seismic deformation analysis of earth dams.

1.2 Seismic Deformation

Seismically-induced deformation has been a major concern for earthquake-resistant design of earth dams in seismic areas both in the academic field and in engineering practice. This is because seismic deformation is the most frequent source of damage caused by earthquakes and also it provides a better design criterion than a conventional factor of safety for evaluation of dynamic stability of earth dams.

1.2.1 Damage Caused by Earthquakes

Experience of damage caused by earthquakes in earth dams shows that the main consequences are permanent deformations in the form of lateral movements and settlement. The major deformation patterns are shown in Figure 1.1, which is taken from Ambraseys (1958).

Lateral movements could occur in the form of a sliding circle or wedge involving a part of or the entire embankment slope. A slide of significant extent could lead to the failure of the dam.

Settlement of the dam or slumping of the slopes causes the loss of freeboard of dam crest. Large settlements could result in overtopping and possible destruction of the dam.

The following are some examples of dams which experienced deformation by earthquakes. Cases where the deformation was caused mainly by liquefaction are not included.

Ono and Lower Murayama Dams / 1923, Kwanto Earthquake

The Ono and Lower Murayama Dams near Tokyo, Japan (Ambraseys, 1960a) were 120-ft. and 80-ft. high, respectively. Both of them were compacted in layers and had a central clay core. The dams were subjected to severe shocks as a result of the Kwanto Earthquake on September 1, 1923, the estimated intensity being 10 on the Rossi-Forel scale.

At the time of the earthquake the water in the Ono Reservoir was 19 ft. below the top of the dam. The crest settled nearly a foot. The embankment

developed serious cracks varying in width from 2 to 10 inches on the surface and extending to depths of 35 to 70 ft. The cracks in general ran parallel to the dam axis, most appearing on or near the crest directly above or to one side of the clay core. Two local slides about 60 ft. long also occurred on the downstream face. Ono Dam was evidently very badly shaken even though it was located 60 miles from the epicenter. No leakage was reported. Following the earthquake the dam was repaired by filling the cracks with a clay-sand grout, and the dam continued in use.

At the Lower Murayama Dam, where the water level was 30 ft. below the crest at the time of the earthquake, it was observed that the crest settled about 8 in., longitudinal cracks opened in the upper portion of the embankment, and the downstream slope bulged about 6 ft. No leakage was reported either, and the dam continued in use.

Otani Dam / 1946, Nankai Earthquake

The Otani earth dam with a height of 89 ft. was completed in 1920, being constructed from compacted fill with a central clay core extending into the sandstone foundation (Ambraseys, 1962).

Resulting from the 1946 Nankai Earthquake, a 250-ft. long longitudinal crack appeared on the crest with additional cracks varying in length between 30 ft. and 180 ft. developing in the higher regions of the upstream slope and running parallel to the axis. Apparently, an incipient slide involving the upper third of the central portion of the upstream slope developed, resulting in considerable movements in the upstream direction. The dam was successfully repaired following the earthquake, using cement grout and recompacting some of the fill.

Hebgen Dam / 1959, West Yellowstone Earthquake

Hebgen dam was constructed in 1914 to a height of 90 ft. The dam was founded on the existing ground surface and consisted primarily of a gravelly clay rolled fill, with a thick central concrete core extending an additional 16 ft. into the foundation material to bedrock (Sherard et al., 1963).

The dam was badly shaken by the 1959 earthquake (with magnitude 7.6) associated with a main fault passing along the north shore of the reservoir within about 700 ft. of the dam. The intensity was estimated as at least 10 on the Modified Mercalli scale. As a result of the earthquake, several large waves were generated in the reservoir, overtopping the dam on several occasions. The earth fill settled on both sides of the concrete core wall, the maximum relative settlement being 4 ft. Several longitudinal cracks having an average width of 2 to 3 in. opened on the dam crest. Similar cracks several hundred feet long also appeared on the upstream slope exposed above the high water line.

Dou River Dam / 1976, Tangshan Earthquake

Dou River Dam is a homogeneous earth dam. It was badly damaged by the Tangshan earthquake on July 28, 1976, which is the most disastrous earthquake in Chinese history. The earthquake had 7.8 magnitude on the Richter scale. The intensity was estimated as 9 on the Modified Mercalli scale. As a result of the earthquake, cracks due to sliding occurred in both the upstream and downstream slopes with a maximum width of 2.2 meters, and the maximum settlement was about 1.6 meters (Zhang and Tamura, 1984). The damaged dam caused much

terror to the survivors of Tangshan Earthquake since it was in imminent danger of collapse (Qian, 1989).

Upper San Fernando Dam / 1971, San Fernando Earthquake

On the morning of February 9, 1971, five to ten million residents of southern California were awakened by the sudden and frightening shock of an earthquake. This earthquake had a Richter magnitude of 6.6. Two of the serious effects of the earthquake were the complete failure of the Lower San Fernando Dam and the partial failure of the Upper San Fernando Dam (Scott, 1971). The Upper San Fernando Dam was built in 1919-1921 of hydraulic fill, and has a concrete-faced upstream slope of 2.5 to 1, and the same downstream slope interrupted by a berm 100 ft. wide. The dam is 1200 ft. in length along the axis and has a height of about 60 ft. As a result of the earthquake, severe longitudinal cracks were clearly evident running along the full length of the dam body on the upstream slope. At the time of the earthquake, the water level in the reservoir was above these cracks so that they became visible after the reservoir had been drawn down (Seed et al., 1975b). The cracks were apparently caused by a general downstream slide and settlement of the top portion of the dam with respect to its foundation, since pressure ridges were visible at the toe of the slide, where the sliding mass encountered passive resistance. Careful survey showed that the crest of the dam at its central portion moved about 5 ft. downstream and settled vertically about 3 ft. The field studies of the Upper San Fernando Dam indicated that the slide was concentrated in a few well-defined slip surfaces going deep into the dam body. The dam is no longer in service.

1.2.2 A Better Criterion for Dynamic Stability of Earth Dams

For the past forty years or more, the pseudo-static approach has been widely used in dynamic stability analysis of earth dams. It is called pseudo-static because, in this approach, the seismic force is assumed to act as a static external load on the mass of each element of the dam. This approach is also called the seismic coefficient method, since the effects of an earthquake on a potential slide mass are represented by an equivalent static horizontal force determined as the product of a seismic coefficient k and the weight of the potential slide mass. Here, the change of inertia force with the dynamic process is ignored. The analysis proceeds in the same way as the conventional slope stability analysis (e.g., Bishop, 1955; Morgenstern and Price, 1965), which involves the calculation of the minimum factor of safety against sliding during an earthquake by examining a number of trial failure surfaces, but includes a horizontal force as calculated above.

Although the pseudo-static method has the advantage of simplicity, it has some limitations. Under static loading, a factor of safety less than unity means failure. However, under dynamic loading, that is not necessarily the case since the seismic force is dynamic or transient; thus, a factor of safety briefly less than unity may not really mean the dam suffers significant damage. Furthermore, in dynamic loading, the value of soil strength changes with time. The change of soil strength cannot be incorporated in the pseudo-static analysis. This makes it very difficult to assess the dynamic stability of an earth dam using a static calculation with a factor of safety. On the other hand, many researchers (e.g., Newmark, 1965; Seed, 1979) have shown that seismic permanent deformations or displacements are the real threat to the stability of earth dams.

Owing to the serious limitations of the seismic coefficient method, the research mentioned above, and the development of computer techniques which can account for realistic soil behavior, it has gradually been accepted that the magnitude of seismically-induced permanent deformations rather than the factor of safety should be the criterion for assessing seismic stability of earth dams.

1.3 Dynamic Approach of Seismic Deformation Analysis

The principle of the dynamic approach is to assess the magnitude of deformations likely to occur during a seismic event by considering the whole dynamic process and the dynamic response characteristics of earth dams. The approach includes the following two aspects.

1) The time-varying inertia forces which result from the earthquake excitation are calculated.

2) The calculated seismic forces are then incorporated in an analysis to estimate the seismic permanent displacements. Because the entire dynamic process or history is considered, changes in soil strength, if they are known, can be accounted for.

In the dynamic approach, it is necessary to estimate the time-varying inertia forces induced in an earth dam by an earthquake. Therefore, determination of the response is very important. Evaluation of the response of flexible structures such as earth dams to arbitrary dynamic loads normally involves a mathematical model of the structure by the method of discretization (Clough et al., 1975). Through discretization, the equilibrium of the dynamic system can be described

by a finite number of ordinary differential equations instead of the partial differential equation required to represent the actual distributed-mass system.

Dynamic response analysis can be placed in two categories: methods based on the use of the system's natural modes of vibration previously estimated; and methods which make use of the direct step-by-step integration of the general governing equation. Limited to a linear dynamic system, methods of the first category are the spectral analysis method and the method of integration of uncoupled equations. The spectral analysis method is based on the use of seismic response spectra. In these methods, the time-history response is determined by summing the responses calculated separately for each natural mode (i.e., mode-superposition method). With a nonlinear dynamic system, direct step-by-step integration must be used.

In the development of the dynamic approach to seismic deformation analysis, many different basic dynamic models have been used (Gazetas, 1985). Depending on the dynamic model employed, the dynamic approach can be classified as the following major methods: 1) shear-beam method, 2) finite difference method, 3) finite element method and 4) simplified method. These will be briefly described in the following section.

1.3.1 Shear-Beam Method

The shear-beam method was first proposed by Mononobe, Takata and Mutumura (1936). In this method, a dam is modeled as a shear beam or shear wedge along its height. In the 20 years after it was proposed, it was fully explored and became a complete engineering theory following the work of

Hatanaka (1955) and of Ambraseys (1960b). Hatanaka showed that shearing deformations in an earth dam are predominant. He performed two- dimensional (2-D) shear-beam analyses for dams in rectangular canyons and developed a rational design procedure using the response spectrum. Ambraseys extended the shear-beam model to account for a truncated-wedge shape of the dam, rectangular canyon and underlying elastic layer. Martin (1965) did careful parameter studies with a one-dimensional (1-D) shear-beam model and obtained solutions for a shear modulus proportional to the cubic root of depth from the crest. Seed and Martin (1966), Ambraseys and Sarma (1967) applied the 1-D shear-beam model to calculate seismic coefficients on potential slide blocks. In 1979, Abdel-Ghaffar and Scott used 1-D and 2-D shear-beam models to compare calculations with the results of full-scale tests and earthquake shaking. Elgamal et al. (1984) and Prevost et al. (1985b) developed a simplified inelastic Galerkin-type formulation using linear shear-beam 1-D and 2-D eigenmodes as the basis functions. This formulation takes into account the nonlinear, hysteretic, and strain-dependent characteristics of the dam material. Dakoulas and Gazetas (1985) generalized the 1-D inhomogeneous shear-beam to account for modulus increasing as an arbitrary power of depth.

The shear-beam method is a simple and economical dynamic approach. But often it does not agree well with all the observed modes of actual dams. Recently, refining work has been carried out to consider such factors as the canyon geometry and material inhomogeneity.

1.3.2 Finite Element Method

In the 1960's, the finite element model was first implemented in studying the dynamic response of earth dams (Clough and Chopra, 1966; Chopra, 1967). Seed (1966) proposed an approach to evaluate deformations in earth dams. The procedure combines 2-D finite element stress analysis and testing procedures on material samples from the dam. Later this approach was applied to assess the causes of failure of the Sheffield Dam (Seed et al., 1969). In 1973, a computer code called QUAD-4 was developed, in which the iterative "equivalent linear" scheme was incorporated in a 2-D variable-damping finite element analysis (Idriss et al., 1973). Zienkiewicz et al. (1980) used a 2-D finite element visco-plasticity effective-stress model for simultaneously estimating permanent deformation and porewater pressure buildup. Also 3-D finite element analyses have been performed (Makdisi et al., 1982; Mejia et al., 1982, 1983; Prevost et al., 1981). Some new material models such as the multi-surface kinematic plasticity theory (Prevost et al., 1985a) have been developed and incorporated in finite element formulations.

1.3.3 Finite Difference Method

Before the application of the finite element method, the finite difference method was perhaps the main numerical technique employed in geotechnical engineering. At least two finite difference studies in the early 1960's (Ishizaki and Hatakeyama, 1962; Medvedev and Sinitsym, 1965) had recognized the 2-D nature of dynamic deformations experienced by infinitely long embankment dams subjected to vertical S-waves, under plane-strain conditions. Cundall (1976) used a finite difference method with explicit time integration, analyzed several

problems, and compared his calculations with the results obtained from other methods. Roth, Scott and Cundall (1986) used the Mohr-Coulomb elasto-plastic model to test its ability to predict earthquake-induced deformations of earth dams. The numerical analysis was performed with the explicit finite difference program DSAGE; computed deformations and acceleration response were compared with measured data obtained from a centrifuge shaking test of a model embankment of dry sand. In his Ph.D. Thesis, Burridge (1987) studied the failure of slopes using the finite difference method with a dynamic relaxation technique. His material model obeys a trilinear stress-strain relationship and contains strain-softening characteristics. The solution predicts localized shear failure zones which initiate at the slope toe and propagate to the slope crest in the manner and geometry observed in centrifuge tests.

1.3.4 Simplified Method

In the Fifth Rankine Lecture, Professor Newmark first proposed a practical procedure for evaluating the potential displacements of an earth dam due to earthquake excitation (Newmark, 1965). The basic idea of this procedure was originated by Ambraseys (1958). This procedure, which is often referred to as the "simplified method", was later extended by Seed and Martin (1966), Ambraseys and Sarma (1967), and Makdisi and Seed (1978). The simplified method models the dam's sliding mass as a rigid block and considers the displacement that occurs along a certain assumed rupture or slip surface. Displacement starts when the inertia force overcomes the frictional resistant force along the slip surface, and it stops when the relative velocities between the dam body above and below the slip surface become equal.

The dynamic behavior of a rigid block with application to dams has been extensively studied both analytically and experimentally (e.g., Seed and Goodman, 1967; Kutter, 1979; Hencher, 1981).

The simplified method has the merit of being simple and straightforward. Therefore, it is widely applied to seismic deformation analysis for stability evaluation of earth dams.

1.4 Overview of the Present Study

As stated in the previous sections, seismic deformation is a very important factor in the design of earth dams. Mitigating seismic deformation prevents earthquake damage. Also dynamic stability should be evaluated by considering the entire time history of inertia forces acting on an earth dam during a seismic event and assessing them in terms of seismic permanent displacements. Therefore, dynamic deformation analysis of earth dams becomes the theme of the present study.

The present study is intended to: 1) examine simplified procedures to assess the seismic permanent displacements of earth dams as a basis for the evaluation of dynamic stability of earth dams; 2) conduct shaking table tests to observe the dynamic behavior of the model used in the simplified method; 3) perform numerical simulations using the developed computer programs, and compare the results with those of the shaking table tests to verify the computer programs; 4) apply the proposed method to La Villita Dam to compute the displacements induced by the earthquake of September 19, 1985 and compare the computed results with the observed results; 5) explain some peculiar phenomena in the

recorded accelerograms from La Villita Dam; and 6) carry out a preliminary analysis for El Infiernillo Dam by applying the presented method.

Although the simplified procedure developed in the present study is within the frame of the simplified method, it has the following special features: 1) not only an inclined plane slip surface but also a circular arc slip surface is considered; 2) the effect of vertical excitation is included. A new application of the simplified procedure is also presented here regarding investigation of the accelerograms obtained on the crest of La Villita Dam during the September 19, 1985 earthquake.

The shaking table used in testing applies earthquake-type excitations as well as harmonic excitations.

To these ends, Chapter 2 starts by introducing the basic idea of the simplified method and establishing the analytical model. From the basic equations presented, computer programs are developed. By using several examples, verifications of the computer programs are attempted. Since there are several parameters involved in the analytical model (sliding block model), parametric studies are performed to understand their effects on the characteristics of the sliding. The effect of vertical excitation is studied by examining an example problem. Experimentally, the dynamic response of the sliding block is studied by carrying out shaking table tests, details of which are presented in Chapter 3. To show the applications of the proposed method and to return to the motivation of this thesis study, analyses of La Villita Dam and El Infiernillo Dam are conducted and presented in Chapter 4. A preliminary

analysis for El Infiernillo Dam comprises Chapter 5. Conclusions and recommendations are addressed in Chapter 6.

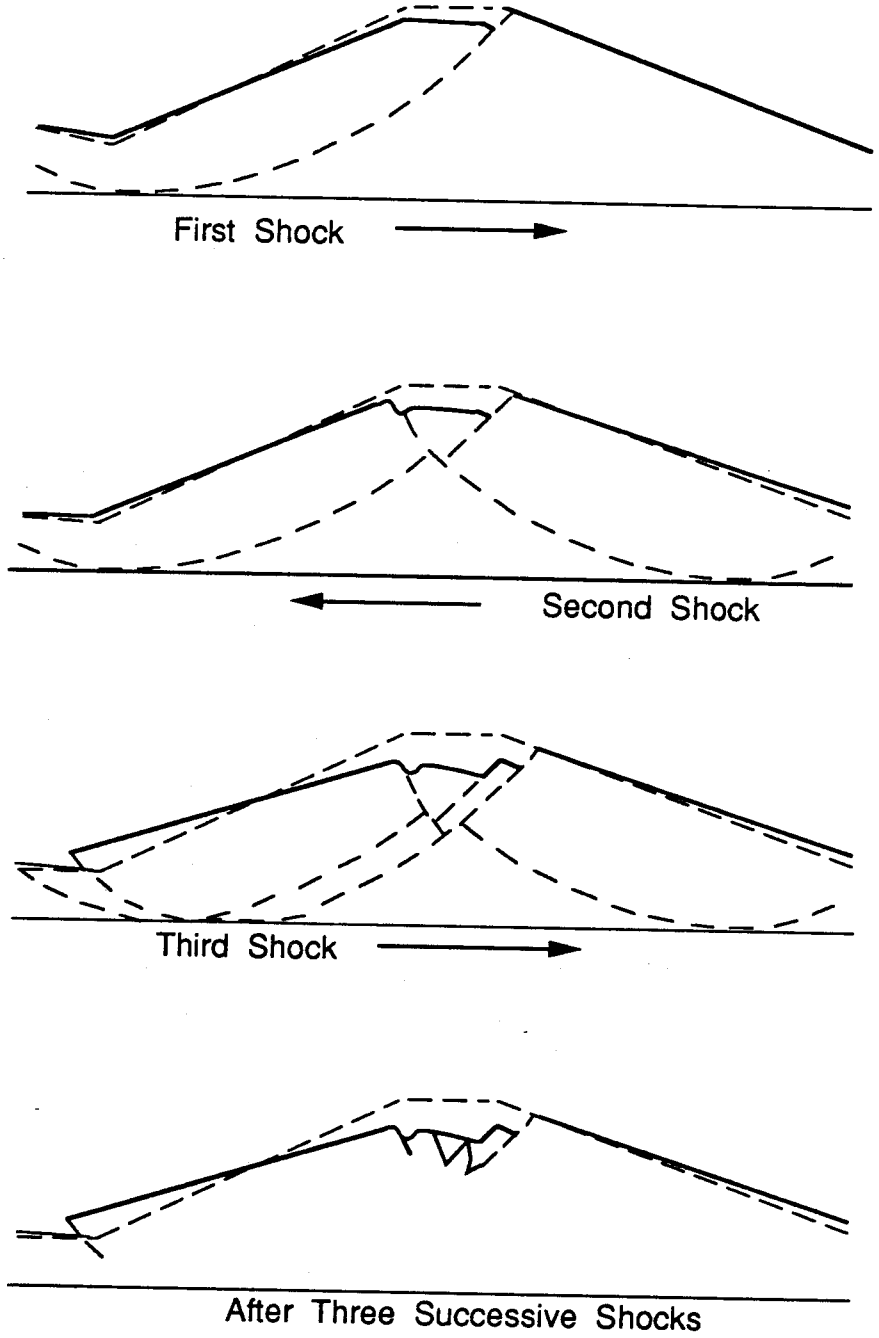

Figure 1.1 Major deformation patterns (after Ambraseys, 1958).

Chapter 2

A SIMPLIFIED METHOD

2.1 Introduction

In order to prevent damage from seismic effects and assess the dynamic stability of an earth dam, it is desirable to evaluate the seismically-induced permanent displacements of the dam during a seismic event. In engineering practice, it is preferable to carry out a preliminary analysis with a simplified method first, to get some idea of the dam behavior before doing any complex analyses such as a dynamic finite element analysis or a finite difference analysis involving an appropriate material constitutive relation. The simplified method is also useful in assuming different dam configurations during the design process. Therefore, in this chapter, a general simplified method is described for analysis of seismic deformation of earth dams. The method is based on the approach proposed by Newmark (1965), which represents the sliding mass as a rigid sliding block. In the procedure developed here, however, not only an inclined plane slip surface but also a circular arc slip surface is considered.

The vertical component of base motion is an important factor in the response of the block. It introduces vertical inertia forces. Downward vertical acceleration will reduce the effective weight of the block, thus reducing the shear forces on the interface or the frictional resistant force in sliding. Under upward

vertical acceleration, the induced inertia force acts downward and thus increases the effect of gravity, thus increasing the shear forces on the interface or the frictional resistant force in sliding. Therefore, in the present study, the vertical excitation is included.

Using this method, the time history of sliding velocity and acceleration of the sliding soil mass can be obtained when an earth dam is subjected to an earthquake excitation. Thus, the seismically-induced transient and permanent displacements in an earth dam can be evaluated.

Hydrodynamic effects from the reservoir water are generally not taken into account. Studies on dam-water-soil interaction (Hall and Chopra, 1982) confirm that for embankment dams such effects are of only secondary importance due to the gradual slope of the upstream face of the dam. Therefore the hydrodynamic effects are neglected in the present study.

2.2 Analytical Model

As shown in Figure 2.1, an earth dam is subjected to an earthquake with horizontal and vertical accelerations, A_h and A_V, as measured from a fixed inertial frame of reference *XOY*. A_h is positive in the direction from the left to the right; i.e., horizontal and tending toward downstream. A_V is positive in the upward direction. Sliding in the earth dam is assumed to occur during the earthquake along a well-defined rupture or slip surface which is either an inclined plane surface or a circular arc surface. The sliding mass is modeled as a single rigid sliding block, which has mass M and mass moment of inertia I_c. The remaining part of the dam below the slip surface moves rigidly with the ground

and is referred to here as the base. Obviously, a number of physical properties of the sliding system are required to completely characterize the model; they include slip surface, mass, overall dimensions, location of the mass center, location of the support points relative to the mass center, sliding resistance (e.g., friction) of the interface material, and characteristics of the base excitations.

2.2.1 Modes of Block Response

In general, a sliding system can have the following different modes of response to a base excitation: rest, slide, rock, slide-rock and free-flight modes (Jones and Shenton, 1990).

A rest mode means no relative movement between the body and base. A slide mode is characterized by a pure translation of the body along the base, where a rock mode is characterized by a pure rotation about one corner of the block. A slide-rock mode is a combination of the previous two, a rotation about, as well as translation of one corner in contact with the base. Free-flight occurs when the block loses all contact with the base.

The mode that a block will be in, or in other words, whether a block under given simultaneous horizontal and vertical base accelerations will remain standing, slide, rock, overturn, or lose contact with the slip surface depends on: 1) the sliding resistance between the block and the slip surface, 2) the dimensions of the block (e.g., aspect ratio of the block (width/height)); 3) geometry of slope; and 4) the magnitude and type of the base motions.

The objective of the dynamic analysis is to determine the resulting motion of the rigid block for a prescribed base motion (constant acceleration, harmonic,

recorded accelerograms, etc.). The dominant modes for an earth dam are rest and slide modes. Therefore, the considerations will be restricted to these two modes.

Friction on the interface between the body and foundation is a complicated phenomenon and many theories exist to model it (Oden and Martins, 1985). In the present study, a Coulomb-type friction is used. The frictional force (F_f) is a function of the normal reaction (N) and the relative velocity ($\dot{x}$) of the point or points in contact on the interface. The coefficient of friction in general is denoted as μ. The coefficient of static friction is denoted as μ_s, and the coefficient of dynamic friction as μ_k.

For a frictional cohesionless material with internal friction angle ϕ, μ is related to ϕ by

$$\mu = \tan\phi \tag{2.1}$$

Therefore μ_s and μ_k are expressed as

$$\mu_s = \tan\phi_s \tag{2.2}$$

$$\mu_k = \tan\phi_k \tag{2.3}$$

where ϕ_s and ϕ_k are the static friction angle and dynamic friction angle of the interface material, respectively.

The forces exerted on the sliding block include inertia forces due to base excitations, normal force and interface frictional resistance force. When sliding is initiated, the inertia forces due to the relative motion of sliding are applied to the block too.

Using D'Alembert's principle and considering the equilibrium of the sliding block, the conditions for sliding are derived and the dynamic equations for the

motion of sliding are established, as described in the following. It is noted that sliding may occur in both upslope and downslope directions.

2.2.2 Basic Equations: Block on an Inclined Plane Slip Surface

Referring to Figure 2.2, consider a rigid block resting on a plane which is inclined at an angle θ. The base is subjected to a horizontal ground acceleration A_h and a vertical ground acceleration A_v. The mass center is at *C*. Since relative movements are considered here, another frame of reference, *xoy*, is used to measure relative movements. Displacements of the block relative to the base are denoted by x(t) and y(t), where x(t) is positive in the downslope direction and y(t) is positive in the outward-normal direction to the inclined plane.

Onset of Slide

Assuming the body is initially at rest, referring to the forces shown in Figure 2.2, which include the inertial and gravity loadings, a slide mode is initiated once the following conditions hold:

$$(- MA_h\cos\theta) + M(A_v + g)\sin\theta = F_f \tag{2.4}$$

$$M(A_v + g)\cos\theta + MA_h\sin\theta = N \tag{2.5}$$

$$|F_f| \geq N\mu_s \tag{2.6}$$

or

$$|- A_h\cos\theta + G\sin\theta| \geq \mu_s(G\cos\theta + A_h\sin\theta) \tag{2.7}$$

where $$G = A_v + g \tag{2.8}$$

and g is the acceleration due to gravity.

If the block starts to slide in the downslope direction, then

$$- A_h\cos\theta + G\sin\theta \geq \mu_s(G\cos\theta + A_h\sin\theta) \tag{2.9}$$

or

$$(\cos\theta + \mu_s\sin\theta)A_h \leq G(\sin\theta - \mu_s\cos\theta) \tag{2.10}$$

i.e.,

$$A_h \leq - G\tan(\phi_s - \theta) \tag{2.11}$$

Define

$$A_e = -A_h \tag{2.12}$$

$$A_{yd} = G\tan(\phi_s - \theta) \tag{2.13}$$

then (2.11) can be written as

$$A_e \geq A_{yd} \tag{2.14}$$

Thus, (2.14) is the condition necessary for downslope sliding to start.

If the block starts to slide in the upslope direction, then

$$-(- A_h\cos\theta + G\sin\theta) \geq \mu_s(G\cos\theta + A_h\sin\theta) \tag{2.15}$$

or

$$(\cos\theta - \mu_s\sin\theta)A_h \geq G(\sin\theta + \mu_s\cos\theta) \tag{2.16}$$

i.e.,

$$A_h \geq G\tan(\phi_s + \theta) \tag{2.17}$$

Define

$$A_{yu} = -G\tan(\phi + \theta) \tag{2.18}$$

then (2.17) can be written as

$$A_e \leq A_{yu} \tag{2.19}$$

Thus, (2.19) is the condition necessary for upslope sliding to start.

Sliding Mode

Once the block is sliding, the dynamic governing equations of motion are

$$MA_e\cos\theta - F_f + MG\sin\theta = M\ddot{x} \tag{2.20}$$

$$MG\cos\theta - MA_e\sin\theta = N \tag{2.21}$$

$$F_f = N\mu_k S(\dot{x}) \tag{2.22}$$

where $S(\dot{x})$ is the signum function in sliding velocity $\dot{x}$, defined as

$$S(\dot{x}) = \begin{cases} 1; & \dot{x} \geq 0 \\ -1; & \dot{x} < 0. \end{cases} \tag{2.23}$$

Simplifying Equations (2.20) to (2.22) leads to

$$\ddot{x} = C_p(A_e - A_y) \tag{2.24}$$

where

$$C_p = \cos\theta + \sin\theta\tan(\phi_k^*) \tag{2.25}$$

$$A_y = G\tan(\phi_k^* - \theta) \tag{2.26}$$

$$\phi_k^* = S(\dot{x})\phi_k \tag{2.27}$$

The absolute accelerations of the block in the *X* and *Y* directions are

$$A_{bh} = A_h + \ddot{x}\cos\theta \tag{2.28}$$

and

$$A_{bv} = A_v - \ddot{x}\sin\theta \tag{2.29}$$

Sliding continues until the relative velocity of the block and base equals zero ($\dot{x} = 0$). At that time, the body momentarily comes to rest relative to the base and Equation (2.14) or (2.19) must be monitored to determine when sliding starts again. Depending on the coefficient of friction and characteristics of the base motion, it is possible to have extended periods of rest during the response.

It is interesting to note that the system is completely characterized by the mass and coefficients of friction. Physical dimensions relating to size and shape need not be specified.

2.2.3 Basic Equations: Block on a Circular Arc Slip Surface

As illustrated in Figure 2.3, a rigid block on a circular arc slip surface is subjected to a horizontal ground acceleration A_h and a vertical ground acceleration A_v. The block has mass M and mass moment of inertia I_c. The mass

center is at C. The block slides along the circle arc about O_c, the center of the circle. The radius of the circle is denoted by R and the distance between the mass center C and O_c is denoted by R_c. Displacements of the block relative to the base are denoted by x(t) along the arc and y(t) perpendicular to the arc. x(t) is positive in the downslope direction and y(t) is positive in the direction towards O_c. Angular rotation about O_c is denoted by $\psi(t)$, positive in the counter-clockwise (i.e., the block slides downslope) direction. Let $\theta(t)$ denote, at time t, the inclined angle of the tangential line through point *b*, which is the point at the bottom of the block on the extended line O_cC. Suppose at $t = 0$, $\theta(0) = \theta_0$.

The inertia forces from the ground excitations and the gravity force are exerted on the block at the mass center, C. They can be expressed as F_t in the tangential direction and F_r in the radial direction (positive as shown in Figure 2.3).

$$F_t = MG\sin\theta + MA_e\cos\theta \tag{2.30}$$

$$F_r = MG\cos\theta - MA_e\sin\theta \tag{2.31}$$

The resultant normal reaction force N from the arc and the frictional resistance force F_f are assumed to be exerted at point *a*, the location of which will be determined later. The angle between O_cC and $O_c a$ is α.

Rest Mode

Equilibrium of force and moment about O_c leads to

$$MG\cos(\theta - \alpha) - MA_e\sin(\theta - \alpha) = N \tag{2.32}$$

$$MG\sin(\theta - \alpha) + MA_e\cos(\theta - \alpha) = F_f \tag{2.33}$$

and

$$F_fR = (MG\sin\theta + MA_e\cos\theta)R_c \tag{2.34}$$

So

$$G\sin(\theta - \alpha) + A_e\cos(\theta - \alpha) = \frac{R_c}{R}(G\sin\theta + A_e\cos\theta) \tag{2.35}$$

Let

$$\sin\delta = \frac{A_e}{\sqrt{G^2 + A_e^2}} \tag{2.36}$$

$$\cos\delta = \frac{G}{\sqrt{G^2 + A_e^2}} \tag{2.37}$$

Then

$$\sin(\theta - \alpha + \delta) = \frac{R_c}{R}\sin(\theta + \delta) \tag{2.38}$$

$$\delta = \arcsin\left(\frac{A_e}{\sqrt{G^2 + A_e^2}}\right) \tag{2.39}$$

Therefore

$$\alpha = (\theta + \delta) - \arcsin\left[\frac{R_c}{R}\sin(\theta + \delta)\right] \tag{2.40}$$

Onset of Sliding

Assuming the body is initially at rest, referring to the forces shown in Figure 2.3, a slide mode is initiated once the following expressions hold:

$$N\cos\alpha - F_f \sin\alpha = F_r \tag{2.41}$$

$$N\sin\alpha + F_f \cos\alpha = F_t \tag{2.42}$$

$$F_t R_c = F_f R \tag{2.43}$$

$$|F_f| \geq N\mu_s \tag{2.44}$$

Therefore

$$N^2 + F_f^2 = F_r^2 + F_t^2 \tag{2.45}$$

$$\left| \frac{R_c}{R} F_t \right| \geq \tan\phi_s \sqrt{F^2 - \left(\frac{R_c}{R} F_t\right)^2} \tag{2.46}$$

or

$$|F_t| \geq \frac{R}{R_c} \sin\phi_s F \tag{2.47}$$

where

$$F = \sqrt{F_r^2 + F_t^2} \tag{2.48}$$

Let

$$f_r = F_r / M = G\cos\theta - A_e \sin\theta \tag{2.49}$$

$$f_t = F_t / M = G\sin\theta + A_e \cos\theta \tag{2.50}$$

$$f = F/M = \sqrt{f_r^2 + f_t^2} \tag{2.51}$$

Then (2.47) becomes

$$|f_t| \geq \frac{R}{R_C} \sin\phi_s f \tag{2.52}$$

or

$$f_t \geq \frac{R}{R_C} f \sin\phi_s \text{ ; for downslope sliding} \tag{2.53}$$

$$f_t \leq -\frac{R}{R_C} f \sin\phi_s \text{ ; for upslope sliding} \tag{2.54}$$

At the instant of onset of sliding,

$$N\cos\alpha - F_f \sin\alpha = F_r \tag{2.55}$$

$$N\sin\alpha + F_f \cos\alpha = F_t \tag{2.56}$$

$$F_t R_C = F_f R \tag{2.57}$$

$$|F_f| = N\mu_s \tag{2.58}$$

So

$$N\sin\alpha + N\tan(\phi_s^*)\cos\alpha = \frac{R}{R_C} N\tan(\phi_s^*) \tag{2.59}$$

i.e.

$$\sin(\alpha + \phi_s^*) = \frac{R}{R_C} \sin(\phi_s^*) \tag{2.60}$$

where

$$\phi_s^* = \phi_s; \quad \text{if (2.53) holds} \tag{2.61}$$

$$\phi_s^* = -\phi_s; \quad \text{if (2.54) holds} \tag{2.62}$$

Thus,

$$\alpha = \arcsin[\frac{R}{R_c}\sin(\phi_s^*)] - \phi_s^* \tag{2.63}$$

Sliding Mode

Once the block is sliding, the dynamic governing equations of motion are

$$F_t R_c - F_f R = I_o \ddot{\psi} \tag{2.64}$$

$$N\cos\alpha - F_f\sin\alpha - F_r = MR_c\dot{\psi}^2 \tag{2.65}$$

$$F_t - N\sin\alpha - F_f\cos\alpha = M\ddot{\psi}\, R_c \tag{2.66}$$

where

$$I_o = I_c + MR_c^2 \tag{2.67}$$

$$F_f = N\tan(\phi_k^*) \tag{2.68}$$

$$\phi_k^* = \phi_k S(\dot{\psi}) \tag{2.69}$$

$$N = M(A_v + g)\cos\theta + MA_h\sin\theta + MR_c\dot{\psi}^2 \tag{2.70}$$

$$\theta = \theta_0 - \psi \tag{2.71}$$

Since

$$\psi = \frac{x(t)}{R_c} \tag{2.72}$$

and letting

$$I_c = MR_i^2 \tag{2.73}$$

therefore,

$$[1 + (\frac{R_i}{R_c})^2]\ddot{x} = f_t - f_n \tan(\phi_k^*) \frac{R}{R_c} \tag{2.74}$$

$$f_n \cos\alpha - f_n \tan(\phi_k^*) \sin\alpha = f_r + \frac{\dot{x}^2}{R_c} \tag{2.75}$$

$$f_t = f_n \sin\alpha + f_n \tan(\phi_k^*) \cos\alpha + \ddot{x} \tag{2.76}$$

where

$$f_n = N/M \tag{2.77}$$

$$\phi_k^* = \phi_k S(\dot{x}) \tag{2.78}$$

From (2.75) and (2.76), we have

$$\cos(\alpha + \phi_k^*) = \frac{f_r^*}{f_n} \tag{2.79}$$

and

$$\sin(\alpha + \phi_k^*) = I^* + \frac{f_t^*}{f_n} \tag{2.80}$$

where

$$f_r^* = \cos(\phi_k^*)(f_r + \frac{\dot{x}^2}{R_c}) \tag{2.81}$$

$$I^* = \sin(\phi_k^*) \frac{R}{R_c} / [1 + (\frac{R_i}{R_c})^2] \tag{2.82}$$

$$f_t^* = f_t \cos(\phi_k^*)\left[1 - \frac{1}{1 + (\frac{R_i}{R_c})^2}\right] \tag{2.83}$$

(2.79) and (2.80) lead to

$$(\frac{f_r^*}{f_n})^2 + (I^* + \frac{f_t^*}{f_n})^2 = 1 \tag{2.84}$$

or

$$(1 - I^{*2}) f_n^2 - 2 I^* f_t^* f_n - (f_r^{*2} + f_t^{*2}) = 0 \tag{2.85}$$

Solving (2.85) yields

$$f_n = \frac{2 I^* f_t^* + \sqrt{4I^{*2} f_t^{*2} + 4(1 - I^{*2})(f_r^{*2} + f_t^{*2})}}{2(1 - I^{*2})} \tag{2.86}$$

Substituting (2.86) into (2.74) and solving yields the equation for $\ddot{x}$. Also

$$\alpha = \arcsin(I^* + \frac{f_t^*}{f_n}) - \phi_k^* \tag{2.87}$$

The absolute accelerations of the block at the mass center C in the *X* and *Y* directions are

$$A_{bh} = A_h + \ddot{x}\cos\theta + \frac{\dot{x}^2}{R_c}\sin\theta \tag{2.88}$$

$$A_{bv} = A_v - \ddot{x}\sin\theta + \frac{\dot{x}^2}{R_c}\cos\theta \tag{2.89}$$

The sliding displacement in the tangential direction, and the absolute accelerations of the block at 0" at the upper corner of the block on the sliding surface in the *X* and *Y* directions are:

$$d_{o''} = \frac{R}{R_c} x \tag{2.90}$$

$$A_{o''h} = A_h + \frac{R}{R_c}\left(\ddot{x}\sin\beta + \frac{\dot{x}^2}{R_c}\cos\beta\right) \tag{2.91}$$

$$A_{o''v} = A_v - \frac{R}{R_c}\left(\ddot{x}\cos\beta - \frac{\dot{x}^2}{R_c}\sin\beta\right) \tag{2.92}$$

where β is the angle of the tangential at o'' to the vertical (Figure 2.3).

Note that the system is not only characterized by the mass and coefficients of friction but also by physical dimensions relating to size and shape of the block and the slip surface, and the initial position of the block.

2.3 Computer Program Development

In the development of the computer programs, the dynamic coefficient of friction is assumed to be equal to the static coefficient and is taken as a simple constant during sliding. If the shape of the coefficient of friction curve as a function of sliding velocity is known experimentally, it can be easily incorporated in the computer programs for an exact solution if desired. Such experiments have not been done for soils yet. The errors caused by the assumption of equal static and dynamic friction coefficients are expected to be less significant than the uncertainties associated with the value of μ and the prediction of future earthquake intensities. However, the value of friction coefficient used in the present model should be carefully determined.

The following outlines the basis for developing the computer program. When the base on which the slip surface is resting is subjected to excitations, A_h

and A_v, no displacement will take place until the thresholds (2.14) or (2.19), (2.53) or (2.54) are satisfied. From that time until the sliding stops, the motion is obtained by solving the dynamic Equations (2.24) or (2.74) to (2.86). Integration of the velocity-time plot yields the sliding displacement of the block.

2.3.1 Methods Used in the Programs

The computer programs have been developed based on the basic equations of the sliding block established in the last section. A total of two computer codes have been written in FORTRAN 77 on VAX/VMS. Computer Code *SLIP-P* is for the case that a block is on an inclined plane. Computer Code *SLIP-C* is for the case that a block is on a circular arc slip surface. Since the dynamic coefficient of friction is assumed to be equal to the static coefficient, no distinction between the static internal friction angle and dynamic internal friction angle of the interface material is made and it is simply denoted as ϕ.

Computer Code SLIP-P

This code is developed to solve the following dynamic equations.

$$\ddot{x} = (\cos\theta + \sin\theta\tan\phi)[A_e - G\tan(\phi - \theta)]; \text{ for downslope sliding} \quad (2.93)$$

$$\ddot{x} = (\cos\theta - \sin\theta\tan\phi)[A_e + G\tan(\phi + \theta)]; \text{ for upslope sliding} \quad (2.94)$$

The threshold of sliding downslope is

$$A_e \geq A_{yd} = G\tan(\phi - \theta) \quad (2.95)$$

And the threshold of sliding upslope is

$$A_e \leq A_{yu} = -G\tan(\phi + \theta) \tag{2.96}$$

Combining (2.93) and (2.94) leads to

$$\ddot{x} = f(\theta, \phi, A_h, G)$$

A fourth-order Runge-Kutta step-by-step time integration scheme (Hildebrand, 1974) was used to solve these equations. In doing so, these equations are written as a set of two first-order, ordinary differential equations (ODE) in the x and $\dot{x}$. The Runge-Kutta step-by-step time integration scheme may be explained as follows.

Considering a general case, let an initial value problem be given as a set of n first-order ODE

$$\dot{x}_i = f_i(t, x_1, x_2, \ldots, x_n) \tag{2.97}$$

$$x_i(t_0) = x_{i0} \tag{2.98}$$

The function x_i at $t_{0+1} = t_0 + h$ (h is the step size) is estimated according to the formula:

$$x_i(t_0 + h) = x_{i0} + \frac{h}{6}(k_{i1} + 2k_{i2} + 2k_{i3} + k_{i4}) \tag{2.99}$$

where

$$k_{i1} = f_i(t_0, x_{10}, x_{20}, \ldots, x_{n0}) \tag{2.100}$$

$$k_{i2} = f_i\left(t_0 + \frac{h}{2}, x_{10} + \frac{h}{2}k_{11}, x_{20} + \frac{h}{2}k_{21}, \ldots, x_{n0} + \frac{h}{2}k_{n1}\right) \tag{2.101}$$

$$k_{i3} = f_i\left(t_0 + \frac{h}{2}, x_{10} + \frac{h}{2}k_{12}, x_{20} + \frac{h}{2}k_{22}, \ldots, x_{n0} + \frac{h}{2}k_{n2}\right) \tag{2.102}$$

$$k_{i4} = f_i\,(t_0 + h,\ x_{10} + hk_{13},\ x_{20} + hk_{23},\ \ldots,\ x_{n0} + hk_{n3}) \tag{2.103}$$

For the sliding problem, n=2, let $x_1 = x$, $x_2 = \dot{x}$, then

$$\dot{x}_1 = x_2 \tag{2.104}$$

$$\dot{x}_2 = f(\theta, \phi, A_h, G) \tag{2.105}$$

Thus,

$$f_1\,(t, x_1, x_2) = x_2 \tag{2.106}$$

$$f_2\,(t, x_1, x_2) = f(\theta, \phi, A_h, G). \tag{2.107}$$

Computer Code SLIP-C

In this case the dynamic equations to be solved are:

$$\ddot{x} = [f_t - f_n \tan(\phi^*)\,\frac{R}{R_c}]/[1 + (\frac{R_i}{R_c})^2] \tag{2.108}$$

$$\theta = \theta_0 - \frac{x}{R_c} \tag{2.109}$$

The threshold of sliding is

$$|f_t| \geq \frac{R}{R_c}\, f \sin\phi \tag{2.110}$$

To develop the computer code, the fourth-order Runge-Kutta step-by-step time integration scheme is used.

2.3.2 Special Considerations

For developing the two computer codes, it is essential to identify if a block is in rest mode or slide mode. Also whether the block is sliding downslope or upslope must be determined. Therefore, the thresholds expressed as (2.95) and (2.96) or (2.110) should be carefully checked. The time step size should be chosen appropriately small in order to reduce the truncation errors.

2.4 Verification of the Computer Programs

In order to verify the developed computer programs, two test examples are presented as follows.

2.4.1 Description of Test Examples

Test Example 1/Code SLIP-P

Consider a problem of a rigid block on an inclined plane subject to horizontal excitation of finite duration T_d, defined by a sinusoidal function

$$A_h(t) = -A_m \sin(\omega t) \tag{2.111}$$

where $\omega = 2\pi f$, f is frequency of the excitation.

Assuming $T_d = 2\pi/\omega. = 20$ sec., $A_m = 0.5g$, $\omega = \pi/10$, $\phi = 40^\circ$, $\theta = 15^\circ$, then $A_{yd} = g\tan(\phi - \theta) = 0.4663g$ and $A_{yu} = -g\tan(\phi + \theta) = -1.4281g$, so the block will only slide downslope.

The problem can be studied analytically as follows.

The block would not slide until time t_1, i.e.,

$$\ddot{x}(t) = 0, \dot{x}(t) = 0, x(t) = 0 ; \qquad 0< t <t_1 \tag{2.112}$$

$$t_1 = \frac{1}{\omega} \arcsin(\frac{A_{yd}}{A_m}) = 3.825 \text{ sec.} \tag{2.113}$$

After it starts to slide, the sliding acceleration, velocity and displacement can be analytically obtained from (for $t_1 < t < t_3$)

$$\ddot{x}(t) = C_d[A_m \sin(\omega t) - A_{yd}] \tag{2.114}$$

$$\dot{x}(t) = -C_d[\frac{A_m}{\omega} \cos(\omega t) + A_{yd} t] + C_1 \tag{2.115}$$

$$x(t) = -C_d[\frac{A_m}{\omega^2} \sin(\omega t) + 0.5 A_{yd} t^2] + C_1 t + C_2 \tag{2.116}$$

where

$$C_d = \cos\theta + \sin\theta \tan\phi = 1.1831 \tag{2.117}$$

$$C_1 = C_d[\frac{A_m}{\omega} \cos(\omega t_1) + A_{yd} t_1] = 27.338 \text{m/sec} \tag{2.118}$$

$$C_2 = C_d A_{yd}(\frac{1}{\omega^2} + 0.5 t_1^2) - C_1 t_1 = -10.236 \text{ m} \tag{2.119}$$

$$t_2 = 0.5 T_d - t_1 \tag{2.120}$$

t_3 is such that

$$-C_d[\frac{A_m}{\omega} \cos(\omega t_3) + A_{yd} t_3] + C_1 = 0 \tag{2.121}$$

and

$$t_3 > t_2 \tag{2.122}$$

Solving (2.121) and (2.122) gives

$$t_3 = 7.365 \text{ sec.} \tag{2.123}$$

After time t_3, the block comes to rest again, thus

$$\ddot{x}(t) = 0, \dot{x}(t) = 0, x(t) = x(t_3) = 1.217 \text{ m} = 121.7 \text{ cm}; \quad t_3 < t < T_d \tag{2.124}$$

Using Computer Code *SLIP-P*, the computation was performed for the same problem as above. The results are shown in Figure 2.4, where the solid line is the analytical solution and the dot line is from the results of *SLIP-P*. It is found that the analytical and computed results are very close.

Test Example 2/Code SLIP-C

In this example, everything is the same as in Test Example 1 except that the block is on a circular arc slip surface with $R = R_c = 10^3$ m and $R_i = 0$, the initial position of the block is defined by the angle, $\theta_o = 15^o$. As in Test Example 1, the block will only slide downslope. It is expected that the block will start sliding at the same time t_1 as in Test Example 1 and the sliding displacement of the block will be smaller than that in Test Example 1. However, they will be quite close because of the large value of R_c. Figure 2.5 shows the results of computation by applying Computer Code *SLIP-C*. These results prove the expectation.

2.4.2 Comments on the Verification

Since the test problem has been attempted successfully in the above examples, the computer programs developed in the present study are considered to have been partially verified. This means the programs can numerically simulate the analytical model established in the previous section. No analytical solutions exist for a circular sliding surface. Whether the model can accurately represent the actual physical and dynamical behavior of a block on a slip surface rationally needs to be tested experimentally, which is the main task in Chapter 3.

2.5 Parametric Studies with Block on an Inclined Plane

The analytical model used in the present study involves three components: rigid block, interface and base excitations. Therefore, it is noted that there are several parameters required to characterize this model: the friction coefficient μ (or the friction angle ϕ) of the interface, the inclined angle of the slip surface θ and the characteristics of the excitation (the amplitude, the frequency content, and the duration; for a sinusoidal excitation, they are A_m, f and T_d). So it is of interest to investigate the effects of all these parameters on the dynamic behavior of the rigid block.

2.5.1 Variation of Block Response with Amplitude of Base Motion

Consider the excitation to be a sinusoidal wave defined by Equation (2.111). The slip surface is an inclined plane with $\theta = 15^o$. Let $\phi = 35^o$, f = 5 Hz, T_d = 0.2 sec, Various values of A_m = 0.4g, 0.5g and 0.6g have been chosen, and computations

have been performed with *SLIP-P*. Figure 2.6 shows the results. It is found that the bigger the amplitude is, the more sliding displacement occurs, as expected.

2.5.2 Variation of Block Response with Frequency of Base Motion

Computations performed are for a block on an inclined plane with $\theta = 15^o$, and $\phi = 40^o$. The excitation is a sinusoidal wave with A_m =0.5g, T_d = 0.2 sec. and different values of f: 5, 10,15 Hz. The results are plotted in Figure 2.7, and it is found that the higher frequency results in less sliding displacement.

2.5.3 Variation of Block response with Duration of Base Motion

Here the influence of duration of base motion on the block response is examined. The parameters used are: $\theta = 15^o$, $\phi = 30^o$, A_m = 0.5g, f = 5 Hz, T_d = 0.2, 0.4, 0.6 sec. Table 2.1 shows the block's sliding displacement versus duration of base motion. For a given steady-state, harmonic excitation, the sliding displacement during each cycle is constant if shearing resistance on the interface does not degrade. Therefore, the total sliding displacement after a given number of cycles *N* is simply the incremental sliding displacement generated during one cycle multiplied by the number of cycles *N*.

2.5.4 Variation of Block Response with Inclined Angle

Now the variable is θ: 12^o, 15^o, 18^o. Other parameters are: $\phi = 30^o$; A_m = 0.5g, f = 5 Hz, T_d = 0.4 sec. The results are shown in Figure 2.8. It is noted that an increase of the inclined angle results in an increase of sliding displacement, again as expected.

2.5.5 Variation of Block Response with Friction Angle

Changing the value of ϕ to be 27^o, 30^o, 33^o and taking $\theta = 15^o$, $A_m = 0.5g$, $f = 5$ Hz and $T_d = 0.2$ sec. yields the results shown in Figure 2.9. With an increase of the internal friction angle, the sliding displacement is reduced. These results correspond to expectation, but it is noted that the displacement is very sensitive to friction angle.

2.5.6 Variation of Block Response with Type of Excitation

In the above computations, the input base excitation is sinusoidal. In order to illustrate the effects of different type of base excitation on the block response, a real earthquake excitation is used in the following computation.

The input acceleration is a section of the accelerogram (time from 0 to 10.22 sec) recorded in the El Centro Earthquake, 1940, which is shown in Figure 2.10(a). θ and ϕ are as chosen 21^o and 30^o. The calculated results are shown in Figure 2.10(b) and (c). Note that the peaks are cut off on the negative side of Figure 2.10(b) during the sliding process.

2.5.7 Effect of Vertical Excitation on Block Response

Three cases are considered to examine the effects of vertical excitation on a block response. The block is on an inclined plane with $\theta = 15^o$, and $\phi = 35^o$.

The horizontal excitation is

$$A_h(t) = +0.5g \sin(2\pi t) \tag{2.125}$$

Case 1: The vertical excitation is out-of-phase with $A_h(t)$, i.e.,

$$A_v(t) = -0.1g \sin(2\pi t) \tag{2.126}$$

Case 2: The vertical excitation is in-phase with $A_h(t)$, i.e.,

$$A_v(t) = +0.1g \sin(2\pi t) \tag{2.127}$$

Case 3: The vertical excitation is not considered, i.e.,

$$A_v(t) = 0 \tag{2.128}$$

In all cases, the duration T_d is 2 sec.

The results are shown in Figures 2.11. It indicates that, compared to the case without vertical excitation, out-of-phase vertical excitation reduces the sliding displacement; however, in-phase vertical excitation increases the sliding displacement.

2.6 Parametric studies with Block on a Circular Arc

When a block is on a circular arc, as compared to the block on an inclined plane, new parameters involved are R, R_c and R_i. This section investigates their influence on the response of the block.

The problem concerned is shown in Figure 2.12. In this problem., the sliding block is a circle segment o" bo'eo". The independent geometric parameters are R and h/R. Once $\frac{h}{R}$ is known, $\frac{R}{R_c}$ and $\frac{R_i}{R_c}$ can be obtained from

$$\frac{R}{R_c} = \frac{C_a}{C_s} \tag{2.129}$$

$$\left(\frac{R_i}{R_c}\right)^2 = \frac{C_i}{C_a}\left(\frac{R}{R_c}\right)^2 - 1 \tag{2.130}$$

where

$$C_a = \frac{\pi}{2} - (\frac{a}{R})\sqrt{1 - (\frac{a}{R})^2} - \arcsin(\frac{a}{R}) \tag{2.131}$$

$$C_s = \frac{2}{3}[1 - (\frac{a}{R})^2]^{1.5} \tag{2.132}$$

$$C_i = \frac{\pi}{4} - (\frac{a}{R})\sqrt{1 - (\frac{a}{R})^2}\,[\frac{1}{6} + \frac{1}{3}(\frac{a}{R})^2] - \frac{1}{2}\arcsin(\frac{a}{R}) \tag{2.133}$$

$$\frac{a}{R} = 1 - \frac{h}{R} \tag{2.134}$$

In this problem, the input motion is horizontal excitation only, as defined as (2.111), amplitude A_m = 0.5g, frequency f =2 Hz and duration T_d = 0.5 sec.

First, R is set to 120 m to study the effect of $\frac{h}{R}$, which is chosen as: 0.05, 0.1 and 0.2. Using the program *SLIP-C*, the response of the block is computed and the results are shown in Figure 2.13. It is found that they are sensitive to $\frac{h}{R}$, especially the angle α (or Alpha in Figure 2.13 (a)), sliding velocity and sliding displacement.

Next, $\frac{h}{R}$ is set to 0.1 to study the effect of R, which is chosen as: 80 m, 120 m and 160 m. The computed results are shown in Figure 2.14. The differences for the results of the three cases are so small that they are hardly distinguishable in the figures.

2.7 Salient Features of Sliding

2.7.1 Sensitivity of Sliding to Parameters

From the results of numerical computations with the developed computer codes, it is observed that the sliding is very sensitive to the characteristics of base

excitation, friction angle, inclined angle and h/R. For example, a 1^{o} change in friction angle results in a 10% ~ 15% change in sliding displacement (Figure 2.9).

2.7.2 Characteristics of Motion

The results indicate that when the excitation is not strong enough, the block is in the rest phase, in which no sliding occurs and the absolute acceleration of the block is the same as that of the base. When the exciting force is big enough to overcome the friction force, the block enters the sliding phase. That is, sliding takes place and the absolute acceleration of the block is different from that of the base. On the recorded accelerogram of the block, asymmetry is found, i.e., in terms of amplitude, the absolute acceleration in the upstream direction is smaller than that in the downstream direction. Absolute accelerations in the upstream direction get cut off when downslope sliding commences. It is also evident from the figures that some narrowing of the absolute acceleration peaks in the downstream direction can occur, although this is not evident for the earthquake response in Figure 2.10.

T_d (sec)	0.2	0.4	0.6
D_s (cm)	0.5977	1.1954	1.7930

Table 2.1 Sliding displacement versus duration of base motion.

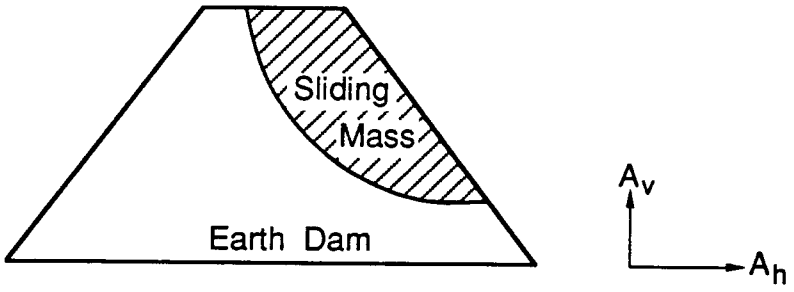

(a) An earth dam

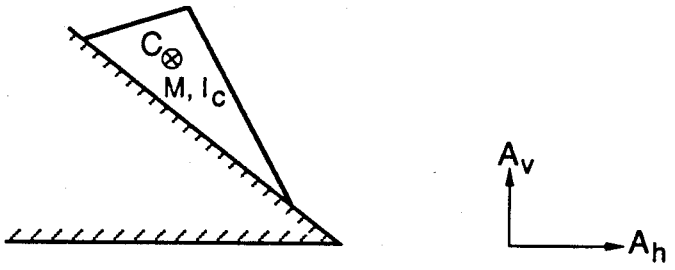

(b) Sliding block on an inclined plane slip surface

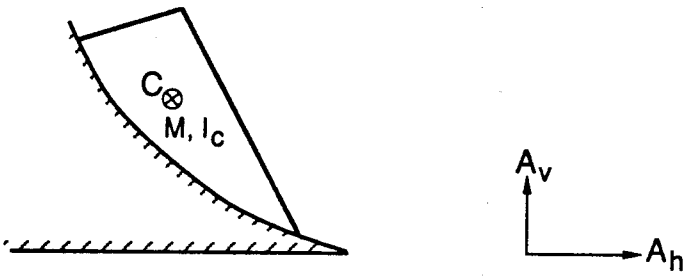

(c) Sliding block on a circular arc slip surface

Figure 2.1 Idealization of problem:
earth dam and sliding block model.

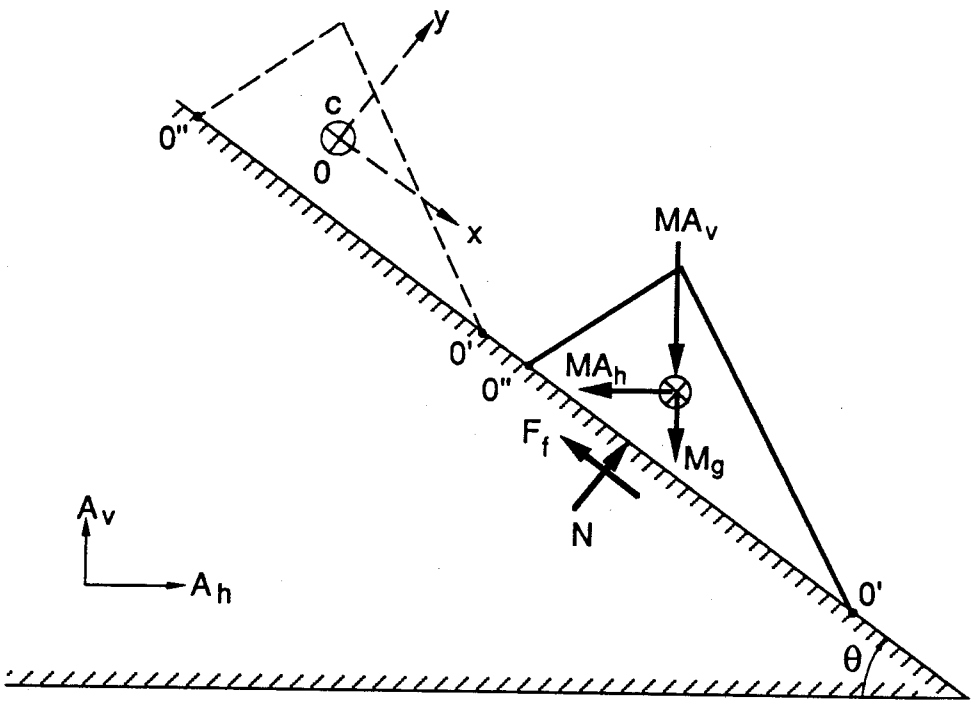

Figure 2.2 Block on an inclined plane.

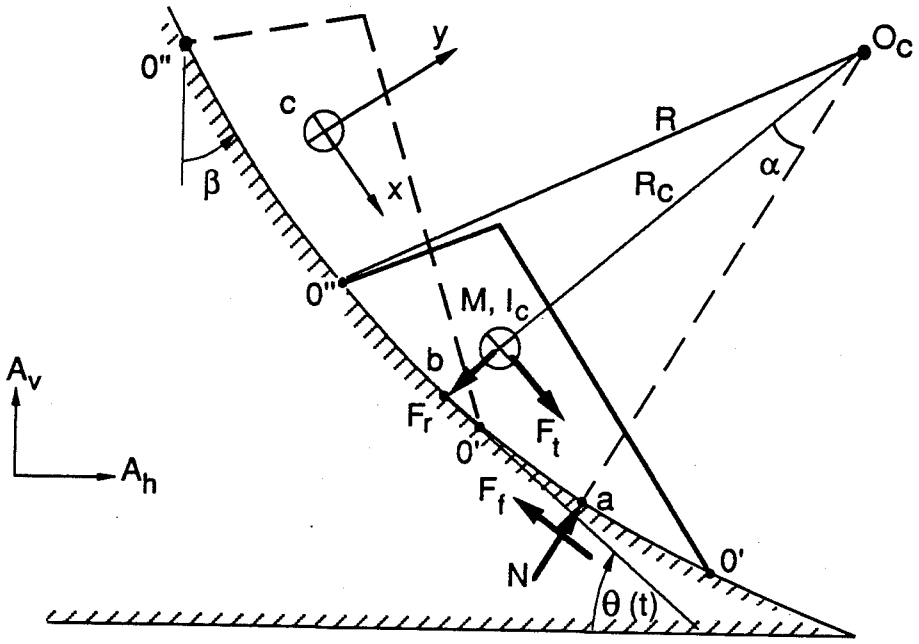

Figure 2.3 Block on a circular arc.

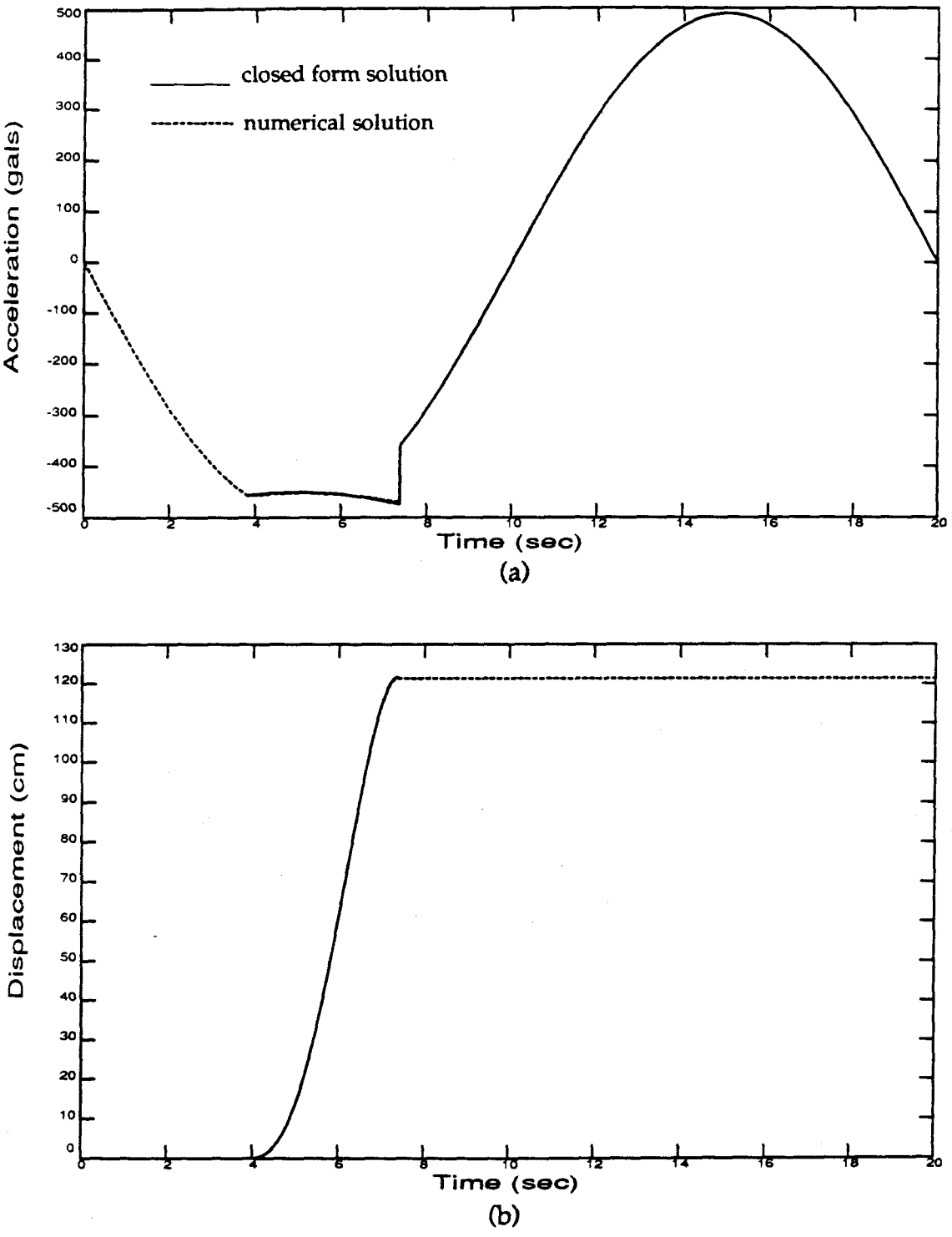

Figure 2.4 Results of Test Example 1/ Code *SLIP-P*.

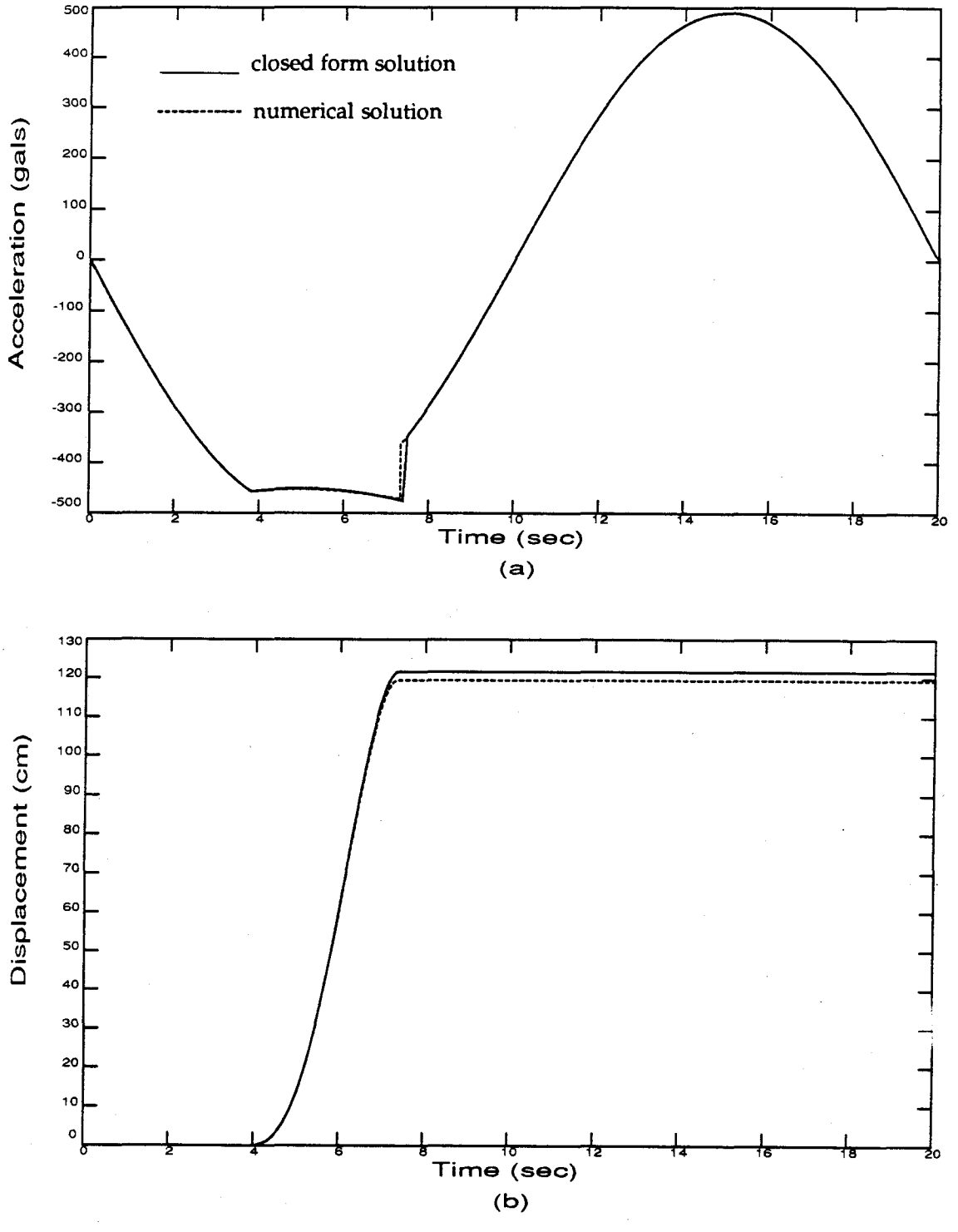

Figure 2.5 Results of Test Example 2/ Code *SLIP-C*.

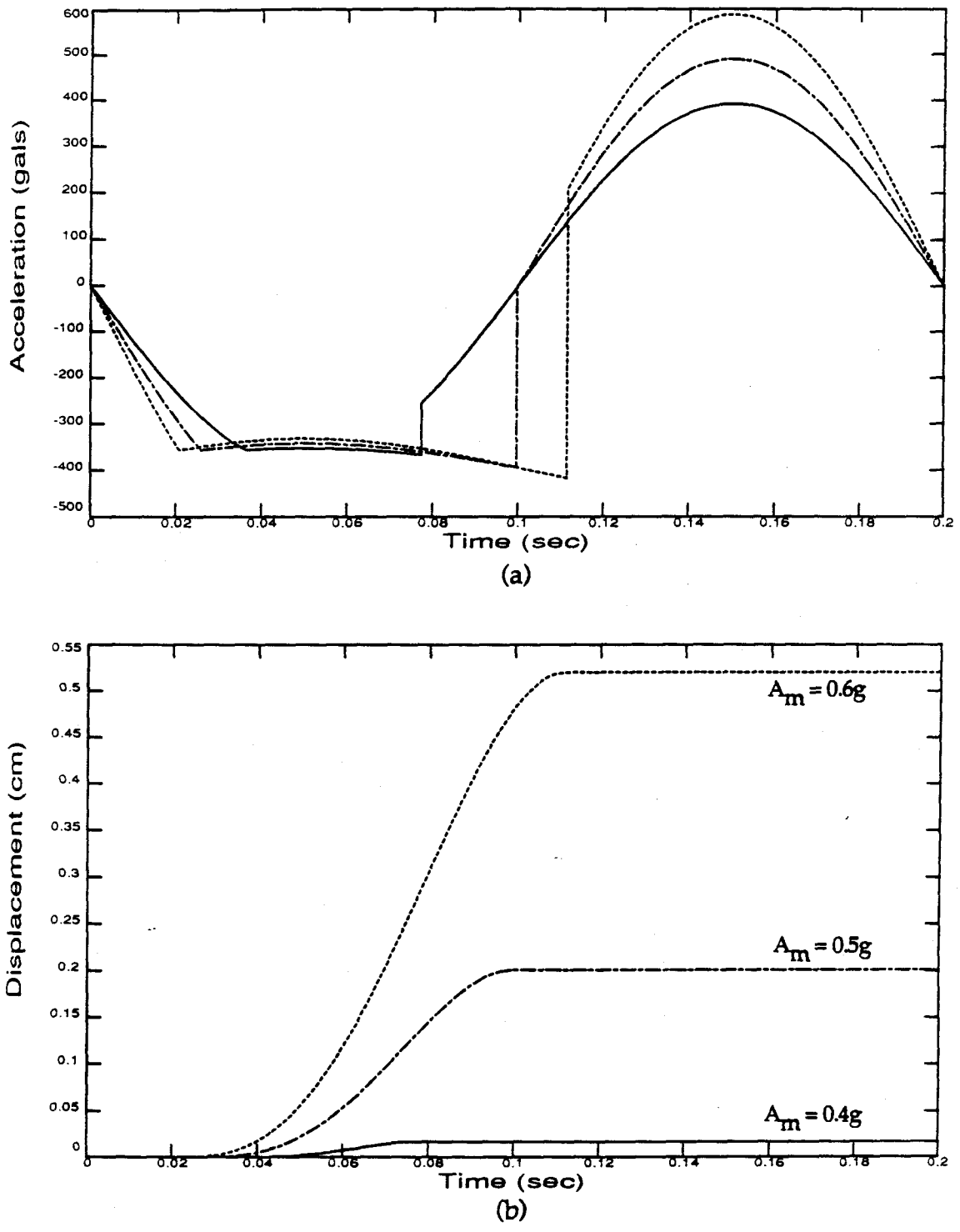

Figure 2.6 Variation of block response with amplitude of base motion.

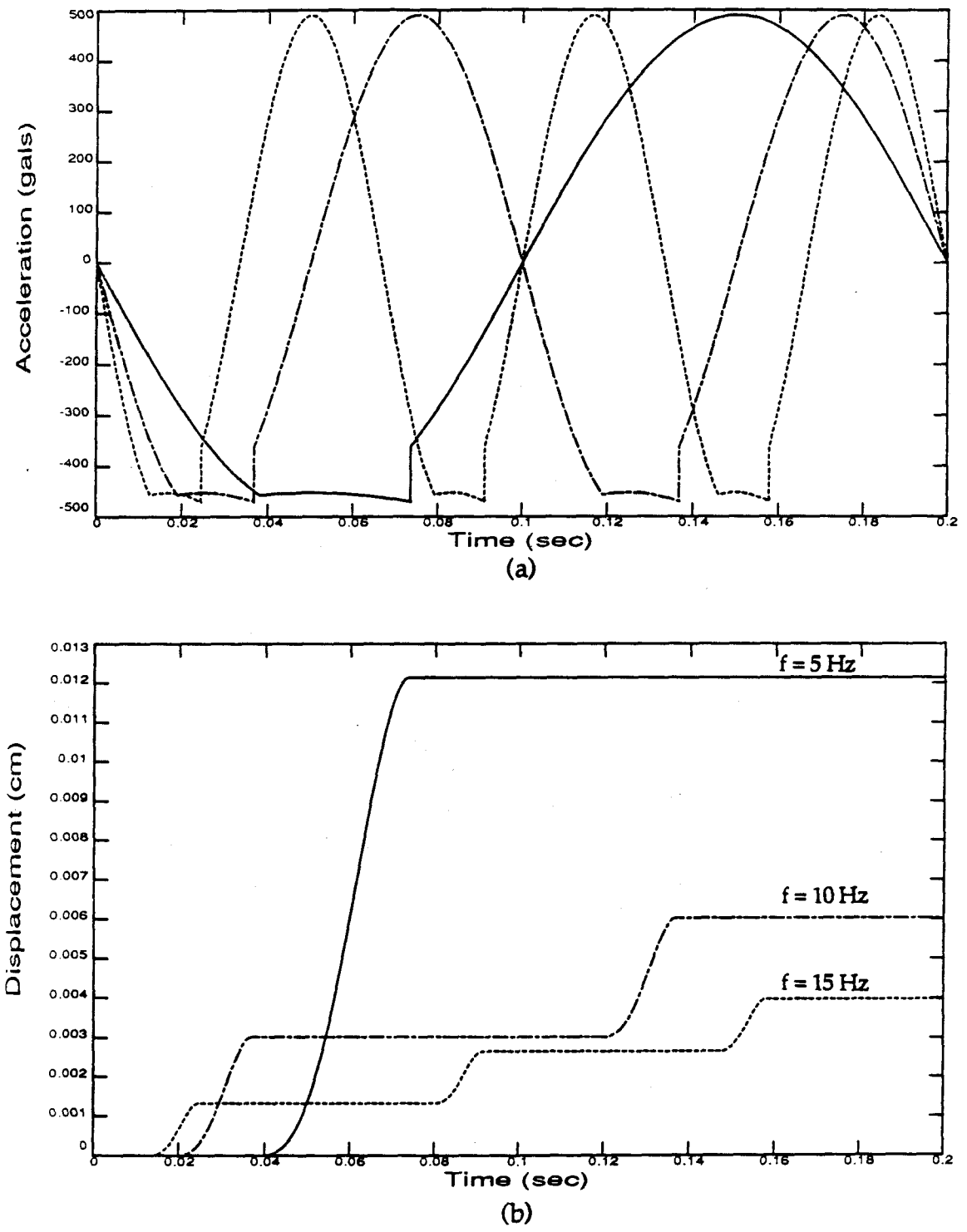

Figure 2.7 Variation of block response with frequency of base motion.

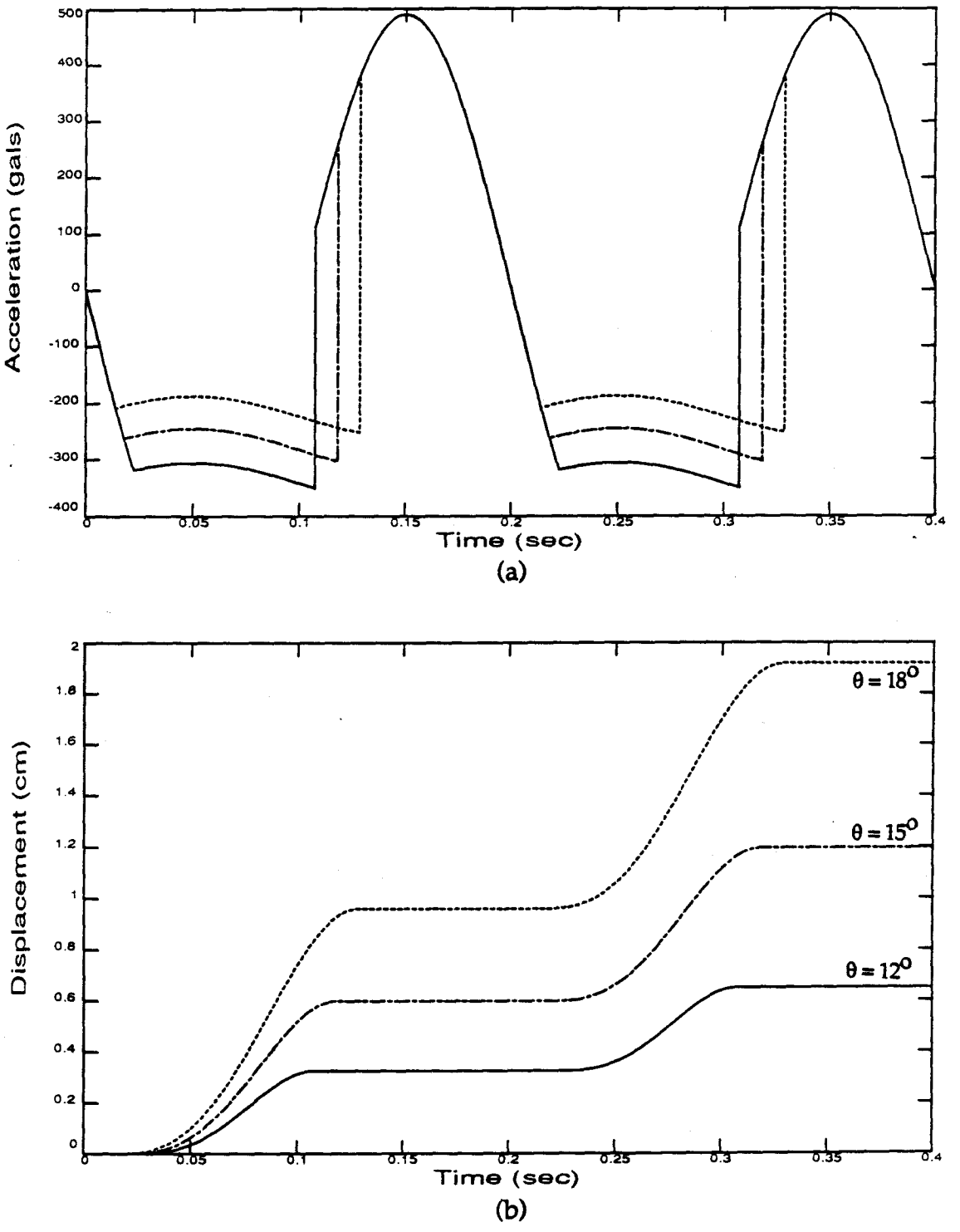

Figure 2.8 Variation of block response with inclined angle.

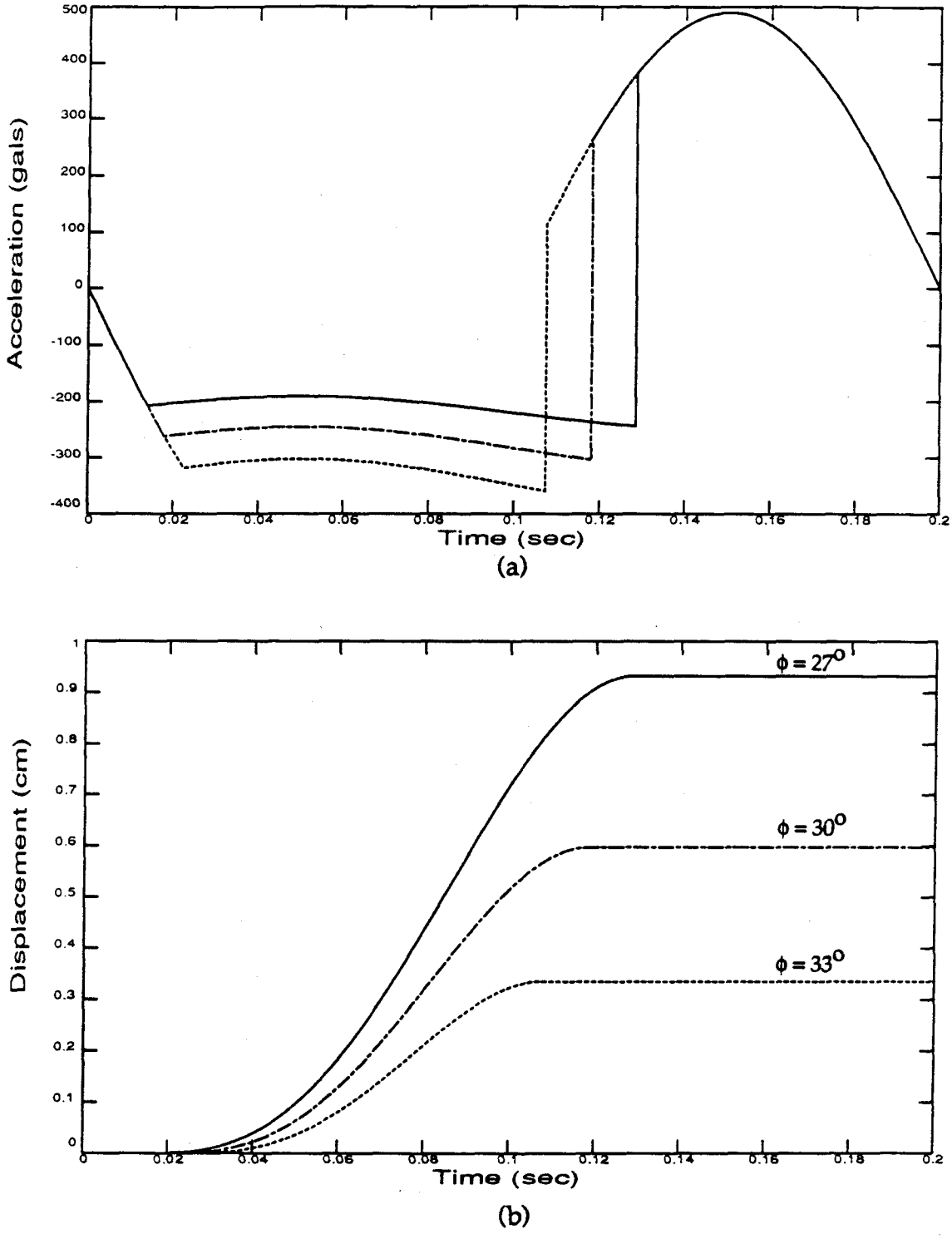

Figure 2.9 Variation of block response with friction angle.

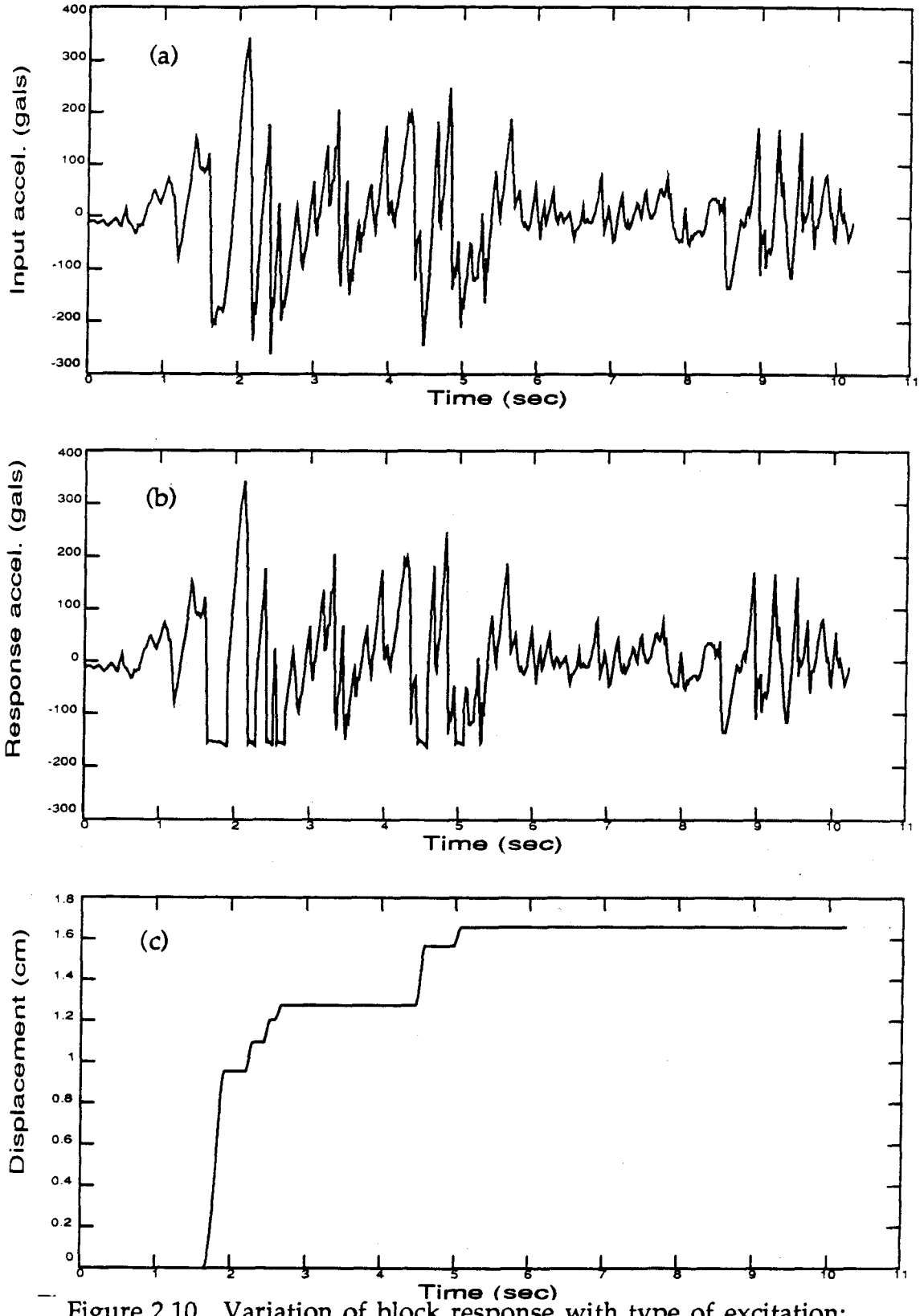

Figure 2.10 Variation of block response with type of excitation: results with accelerogram recorded in the El Centro Earthquake.

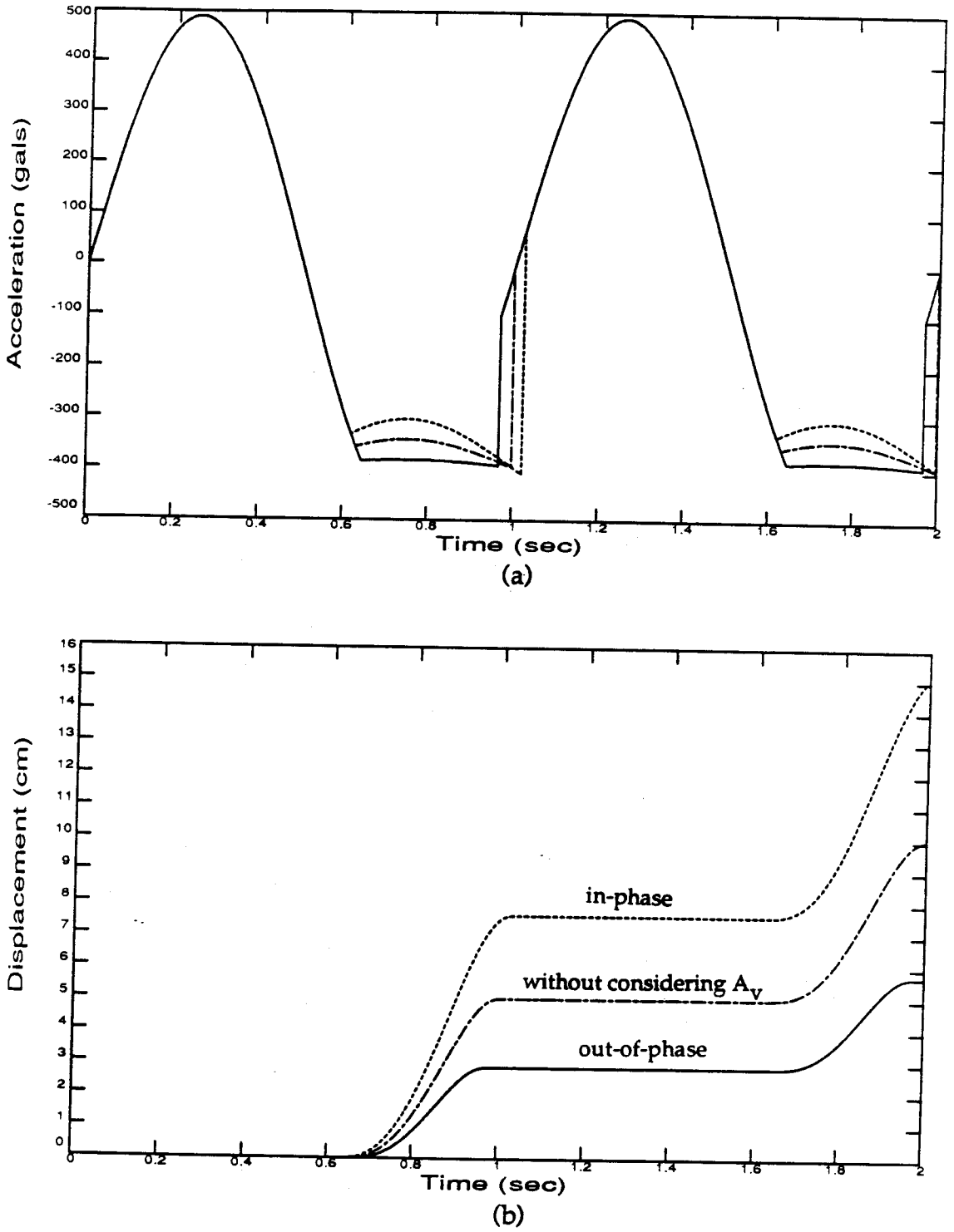

Figure 2.11 Effect of vertical excitation on block response.

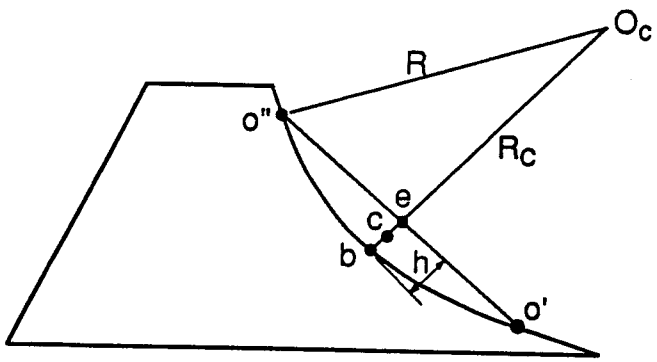

(a) Geometrical configuration

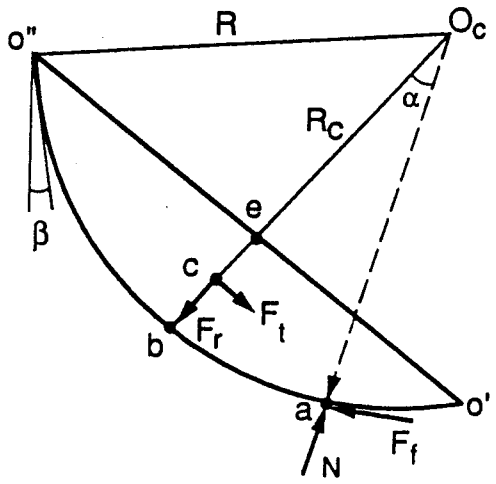

(b) Force diagram

Figure 2.12 Problem concerned in parametric studies for the block on a circular arc.

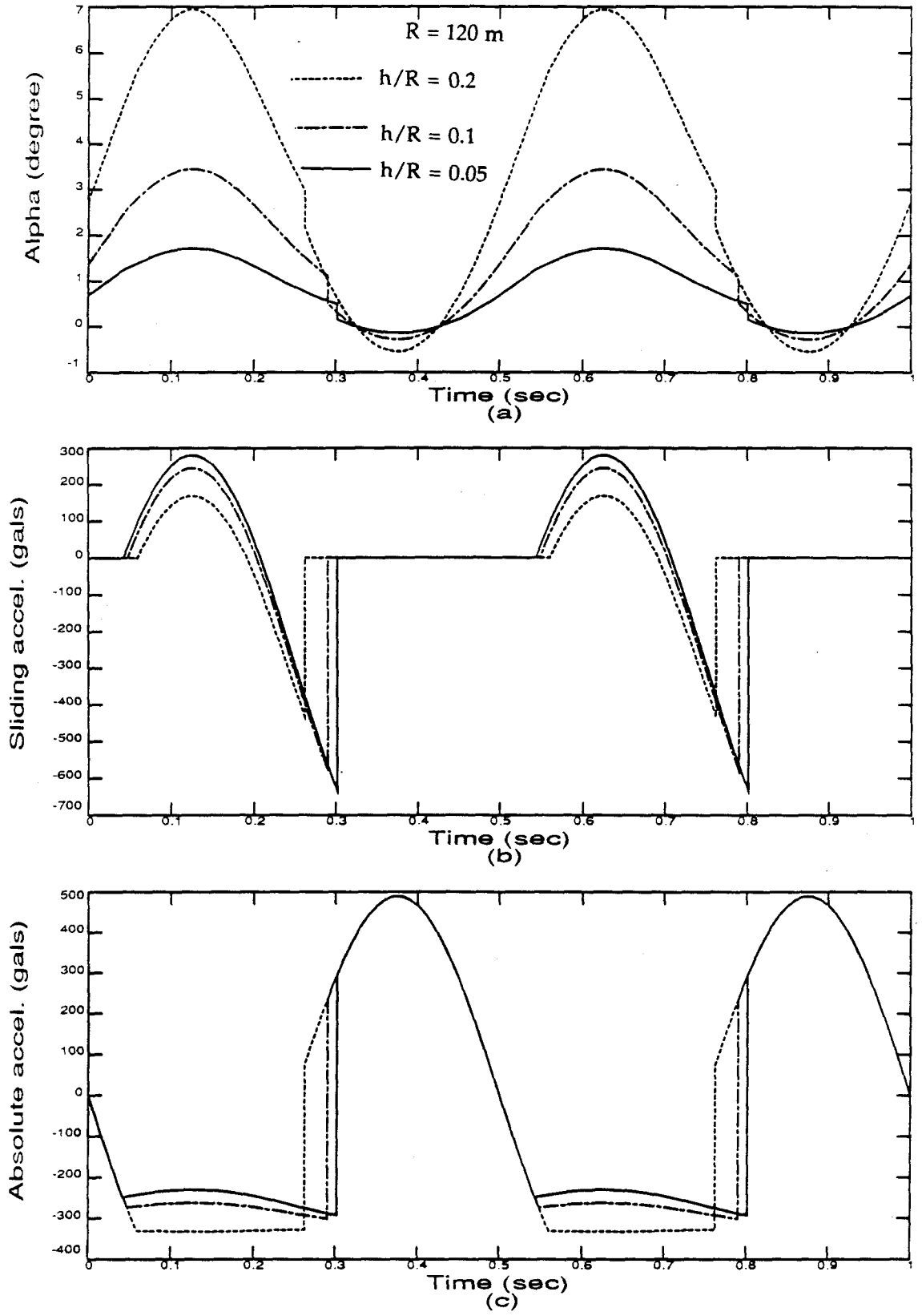

Figure 2.13 Block on a circular arc: effect of h/R.

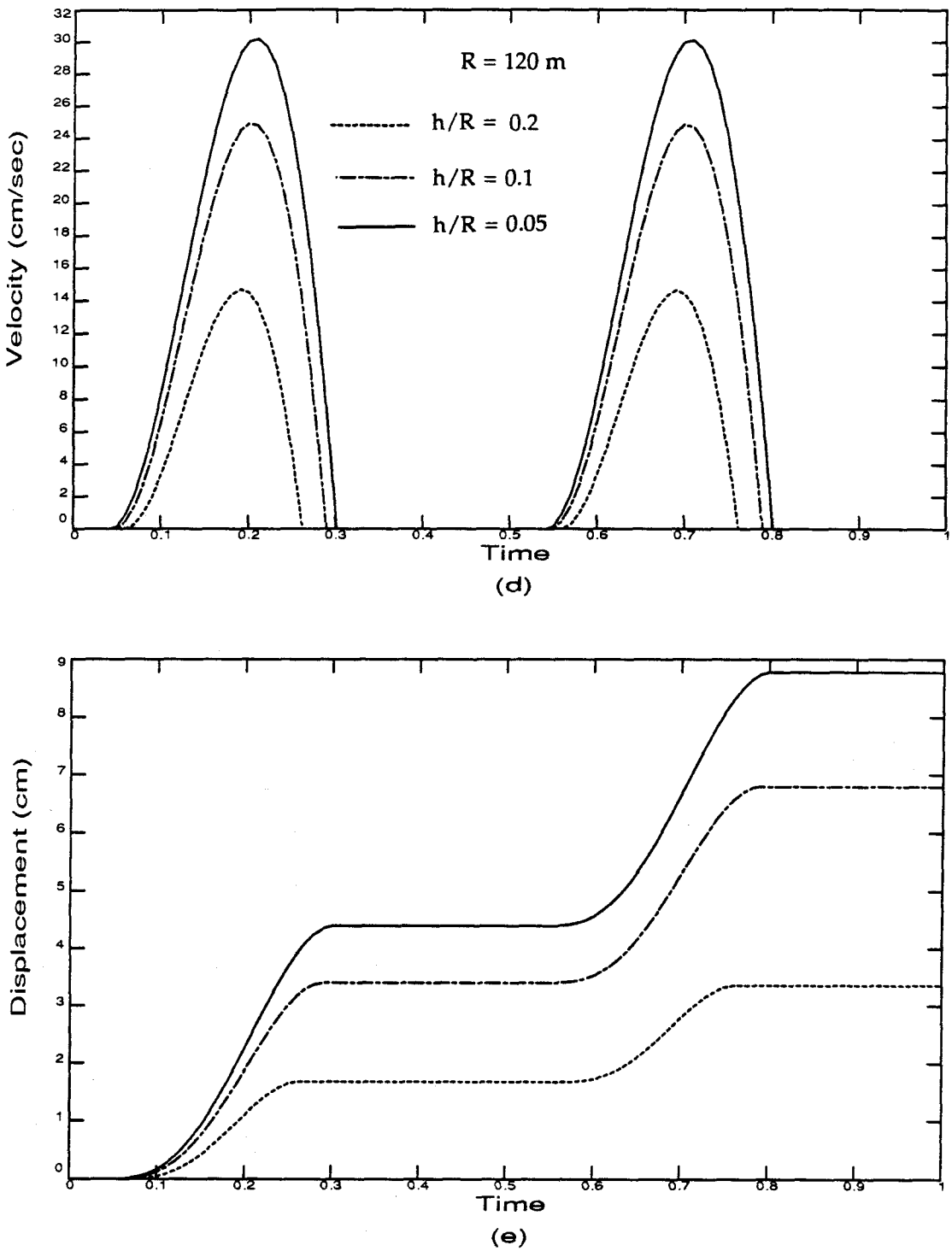

Figure 2.13 Block on a circular arc: effect of h/R (continued).

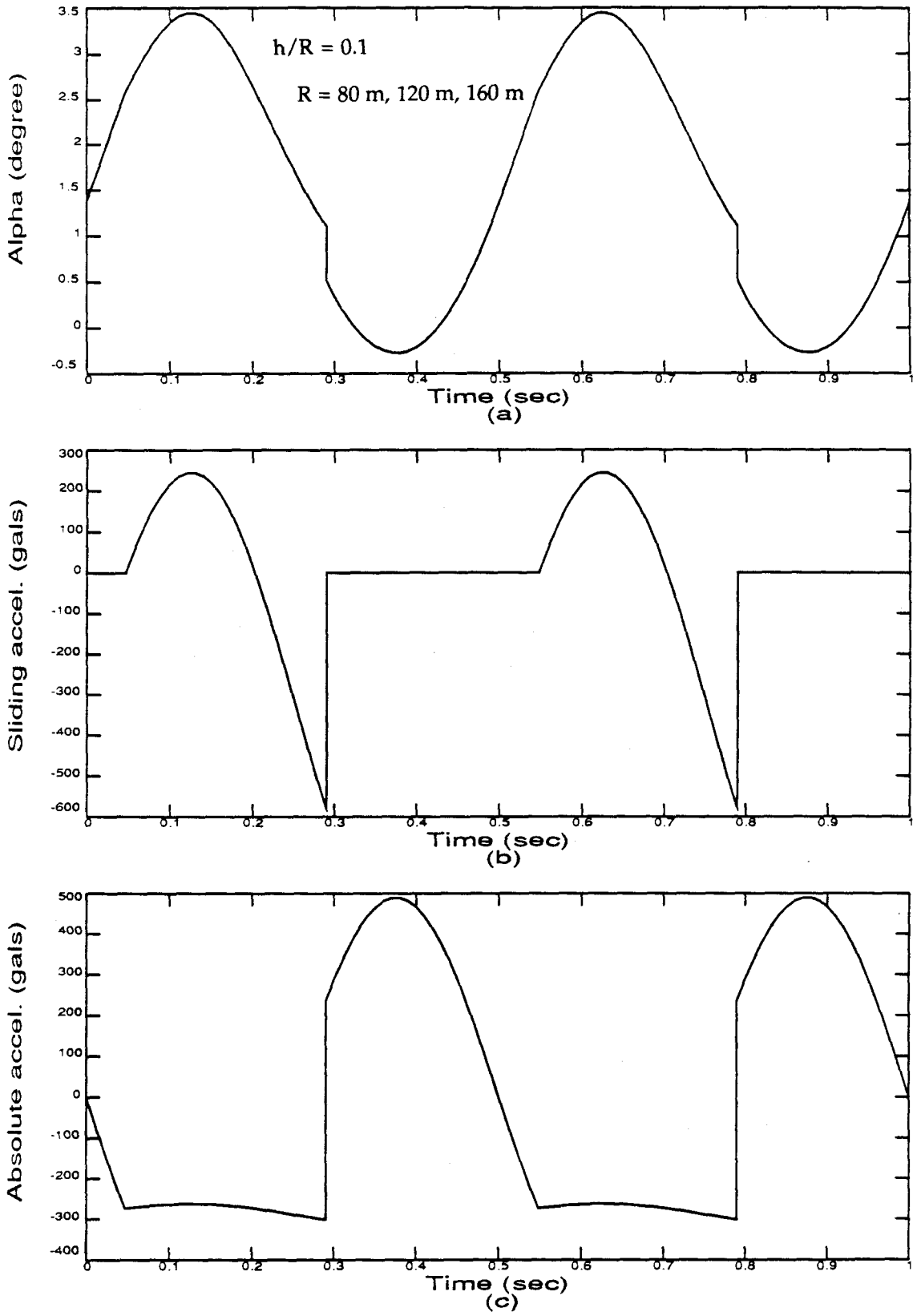

Figure 2.14 Block on a circular arc: effect of R.

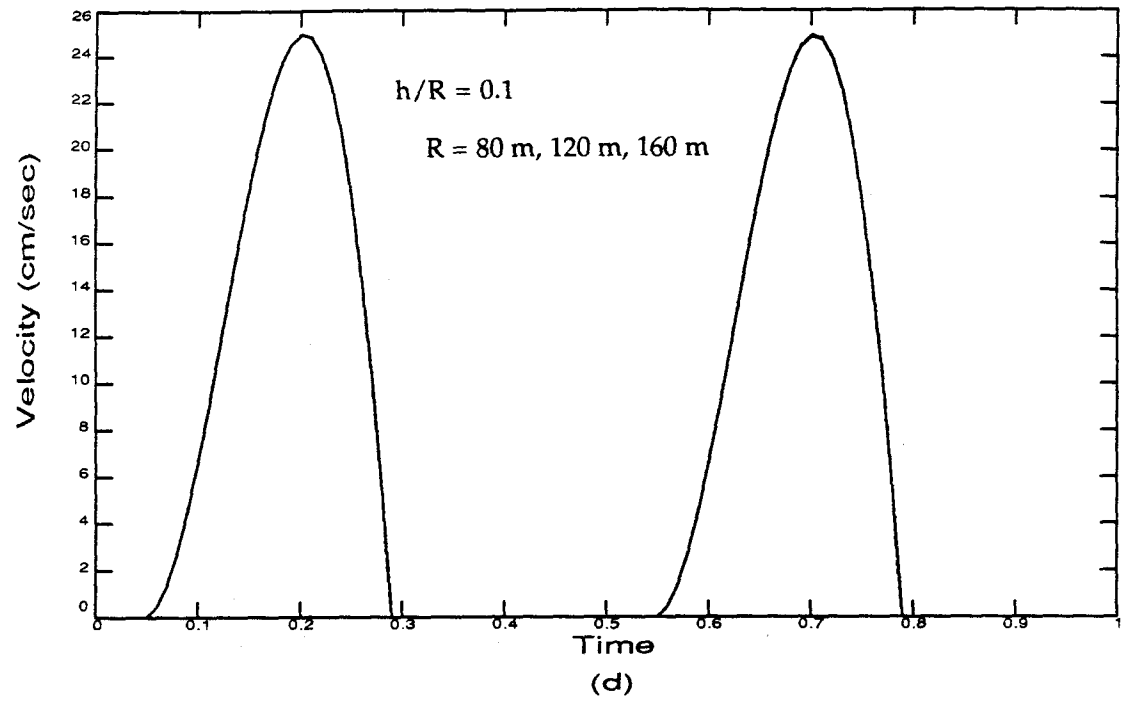

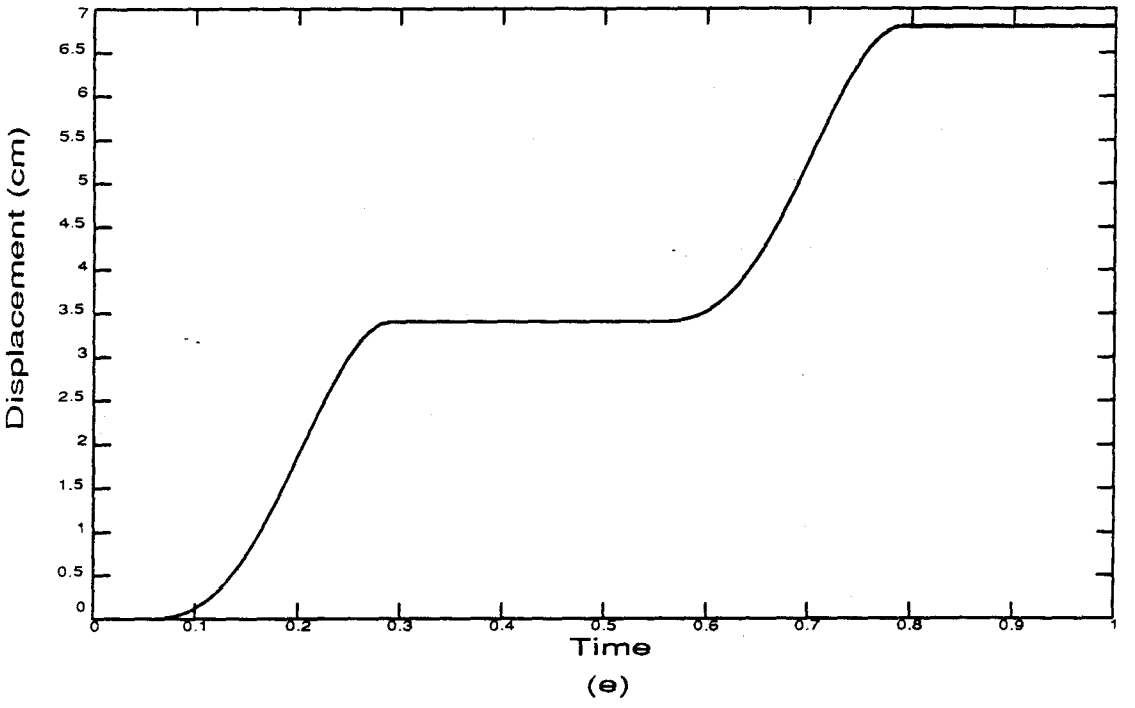

Figure 2.14 Block on a circular arc: effect of R (continued).

Chapter 3

VALIDATION OF MODEL: SHAKING TABLE TESTS AND NUMERICAL SIMULATIONS

3.1 Introduction

In the simplified method described in the previous chapter, a rigid block is supported through non-symmetric sliding resistance on an inclined plane or a circular arc surface. The rigid block represents the potential sliding mass during a seismic event, and the inclined plane or the circular arc surface is regarded as the rupture or slip surface which is subjected to the base excitation horizontally, vertically or both. In order to validate this analytical model and observe the behavior of a rigid block, an experimental investigation with shaking table tests has been performed in the present study. Only the inclined plane slip surface is employed. Also for verification of the computer programs developed, comprehensive numerical simulations and comparison with the experimental results have been carried out.

A shaking table has been widely adopted for dynamic experiments on structures or structural models. Usually, shaking table tests can be utilized for the following purposes (Shibata, 1984): 1) the investigation of dynamic characteristics of structures, 2) the validation of a computer code for dynamic

response analysis of a structure and 3) the qualification of newly designed components. Applying a shaking table test to the investigation of the sliding block model is of great significance.

As noted previously, there are several parameters involved in the rigid block model on an inclined plane: the friction coefficient, the inclined angle, and the excitation characteristics (amplitude, frequency content, and duration). Therefore, the effects of all these parameters on the dynamic behavior of the rigid block have been considered in the shaking table tests. In order to have a complete understanding of the sliding model, the study described in this chapter not only deals with harmonic (sinusoidal) motions but also with earthquake-type excitations. By means of shaking table tests and comprehensive numerical simulations, the investigation presented here focuses on studying the dynamic characteristics of the sliding block response under various base excitations, and its significance to the understanding of the dynamic behavior of real earth structures.

3.2 Experimental Setup Preparation

The experimental setup of the model, as sketched in Figure 3.1, consists of two base plates, two vertical supporting plates, two bearings and one inclined plate. The setup parts, all made of aluminum, are connected together by bolts. The arrangement is fixed on the testing platform by bolting the base plates to the platform. The inclined plate is rotatable around the bearings so that various inclined angles can be obtained. The sliding block is made of steel with dimensions 5" x 3.25" x 2.5" and a weight of 11.29 pounds. Various friction angles

were achieved by glueing different types of sandpaper to the surfaces of the inclined plate and the bottom of the block.

During the initial testing, it was found that the block would slide off the sliding path if it was directly placed on the flat surface of the inclined plate. In order to keep the sliding block straight for measurement purpose, a special arrangement was made. In this arrangement (see Figure 3.1(b)), two plates are set apart to form a slot and three bearings are mounted on the bottom of the block. The bearings fit into the slot and constrain the block to travel in a straight line while not affecting the friction coefficient.

3.3 Apparatus and Instrumentation

The shaking table tests were carried out on an earthquake simulation testing system at Caltech manufactured by MTS System Corporation, which is labeled MTS 840 Vibration Test System. The system has an unidirectional servohydraulic vibration table which delivers one horizontal component of ground motion (i.e., one horizontal degree of freedom). The table consists of a 36" x 44" steel testing platform supported by two granite blocks, each of which is enclosed in a steel case. A thin layer of hydraulic fluid between the granite and steel provides a surface of minimum friction to facilitate table motion. The table is driven by a 3" diameter piston mounted directly beneath it. The piston is capable of producing 3300 pounds of dynamic force over a frequency range of 0-150 Hz with a 3" peak displacement amplitude. Movement of the piston results from the porting of hydraulic fluid pressurized to 3000 p.s.i. Porting (and, consequently, table motion) is controlled by circuitry in the dynamic response controller, which can be operated in acceleration or displacement control modes. Under acceleration

control, excitation waveforms are maintained by comparison of the rms value of the input signal to the rms value of the table motion, which is monitored by system accelerometers. The error signal generated by this comparison is applied to a servovalve, which attempts to compensate for discrepancies by modifying the flow of hydraulic fluid to the piston. The system has good repeatability and linearity of an input waveform (Yan, 1989). Figure 3.2(a) is a photo of the testing model on the table. Two sources provided the signals used to drive the table, depending on the type of test being carried out. A Hewlett-Packard function generator produced sinusoidal signals or frequency sweeps, while a computer-controlled digital-to-analog converter (DAC) was used for the earthquake excitations. This DAC, designed and built at Caltech, can convert digitized signals to their analog form at a maximum rate of 200,000 samples per second. The function generators were controlled manually, while a Zenith 120 personal computer initiated the earthquake tests through interactive software and output signals to the DAC. Figure 3.2(b) shows a photo of the console of the vibration system, the computer and the DAC.

Acceleration and displacement transducers were used to record the model's dynamic response. Entran accelerometers (Model No.: EGA-125F) were selected. They possess a flat frequency response to 250 Hz, have dimensions 0.27" x 0.14" x 0.14", and weigh 0.5 grams. The particular accelerometers employed have full scale ranges varying from 10 to 500g and outputs varying from 0.5 to 12 millivolts per g. The displacement transducer was made by the author, and consists of a potentiometer, a pulley and a string. As sketched in Figure 3.4(b), there is a steel bar connecting the block and the string. When the block slides, the string will rotate the pulley so that the electrical potential of the potentiometer

will change. By calibrating the potentiometer, the sliding displacement can be measured.

3.4 Data Acquisition System and Signal Conditioning

The accelerometer signals initially passed through an 8 channel amplifier with selectable gains ranging from 1 to 1500. They were then transferred to a high-pass filter to eliminate any DC voltage component. The conditioned signals are sent through a second amplification stage and another high-pass filter before entering an analog-to-digital converter (ADC). The ADC is a 16 channel, 12 bit integrated circuit design with a maximum sampling rate of 28,570 samples per second. Full scale output of the ADC is selectable and corresponds either to +/- 2.5 volts or +/- 5.0 volts. The output of the ADC is stored in computer memory and written to a 5.25" floppy disk. The data sampling and storage are accomplished simultaneously with the output of the excitation on the same Zenith 120. The ADC is in the same box as the DAC.

3.5 Testing Procedures

3.5.1 First Stage: Frequency Sweep

The first stage in the dynamic testing of the model was to determine the natural frequencies and the damping ratios of the inclined plate and the vertical supporting plate by means of frequency sweeps. These sweeps were conducted with the table under acceleration control, in which a selected table acceleration amplitude was maintained by the controller on the console while the frequency was varied over the range of interest. A sinusoidal wave was fit to the model's

digitized response data by a least-squares algorithm developed at Caltech (Duron, 1987). The algorithm outputs the exact frequency of excitation, acceleration and displacement response amplitudes, and phase differences between responses and the excitation. This information can yield frequency response curves and mode shapes.

In the frequency sweep test, accelerometer A_1 was placed on the front vertical surface of the platform of the table. The time history recorded by this accelerometer was considered to be the base motion of the model. Accelerometer A_2 was placed on the center of the inclined plate to measure the acceleration in the outward-normal direction of the inclined plate. Accelerometer A_3 was placed on the front vertical surface of the vertical plate to measure the acceleration in the horizontal direction. The locations of the accelerometers are shown in Figure 3.3. In the test for determination of the natural frequencies and the damping ratio of the inclined plate, the excitation amplitude was 0.25g and the frequency range was 10-80 Hz, whereas in the test for determination of the natural frequencies and the damping ratio of the vertical supporting plate, the excitation amplitude was the same, 0.25g, and the frequency range was 10-130 Hz.

3.5.2 Second Stage: Vibration Tests

The second stage of testing subjected the model to two types of vibration. Type 1 consisted of sinusoidal excitations with various frequencies and amplitudes. Type 2 was an earthquake-like time history. The digitized acceleration time history of the earthquake contained 2688 acceleration points at a time interval of 0.02 seconds, resulting in a duration of 53.74 seconds. The time scale was compressed so that the excitation duration became 47.65 sec, or 24.33

sec or 4.87 sec before application to the model. Linear interpolation between existing data points resulted in 8192 acceleration values used in the digital to analog conversion process. The ADC sampled 65,520 total points, with a D to A conversion (excitation output) occurring every eight samples. A total of 4 channels (3 accelerometers and 1 displacement transducer) was sampled during the tests on the model, resulting in 16,380 points per channel and a Nyquist frequency of 1,638 Hz. Although the controlling software used in the tests of Type 1 was the same as in those of Type 2, the signals of D to A (excitation output) were not connected to the shaking table, instead the excitations generated by the function generator were input to the table directly.

For each test, the accelerations of the inclined plate and the sliding block and the sliding displacement of the block were measured through the computer-controlled data acquisition system. The accelerations were obtained from three accelerometers (A_1, A_2 and A_3) attached to the plate surfaces and the sliding block. A_1 and A_2 measured the acceleration of the inclined plate in the inclined and outward-normal directions, respectively, and A_3 measured the acceleration of the block in the inclined direction. The sliding displacements were obtained from one displacement transducer mounted on the inclined plate. The locations of all the transducers are shown in Figure 3.4.

3.5.3 Measurement of Friction Angle

The friction angle (ϕ) between the block and the sliding surface was measured in two ways. One way was to lift the inclined plate around its bearing while the block sits on the plate. When the plate is lifted to such an angle that the block starts to slide down, this inclined angle is the value of the friction angle, ϕ_1. The

other way was to pull the block with the inclined plate in a horizontal position. Measuring the pulling force with a force balance at the time that the block moves at constant velocity determines a value of friction angle, ϕ_2. ϕ_1 is close to the static fiction angle and ϕ_2 is close to the dynamic fiction angle.

3.6 Data Processing

The data recorded from the shaking table tests were processed on a MicroVax using a computer program called SIG, which was developed by graduate student Robert Beck and made available for use in the Caltech Engineering Division.

3.7 Test Results

This section presents the results of the shaking table tests. The results included are from the frequency sweeps and vibration tests (both sinusoidal and modified earthquake record excitations); the latter typically include time histories of the inclined plate's accelerations and the rigid block's acceleration and sliding displacement. All the test results are illustrated in figures at the end of this chapter.

3.7.1 Frequency Sweep

Frequency response curves from the frequency sweep tests for the plates are plotted in Figure 3.5. They indicate that the fundamental frequency of the inclined plate is 54 Hz, and that the fundamental frequency of the vertical supporting plate is greater than 120 Hz which is beyond the frequency range of

interest for the sliding block. The damping ratio for the inclined plate was determined by the half-power method (Clough and Penzien, 1975) as 3.8%.

3.7.2 Vibration Tests

The test investigations focus on the dynamic behavior of the block on the inclined plate subjected to base excitations. Two types of vibration were taken as the test input excitation.

Tests with Type 1 Vibration: Sinusoidal Excitations

Five tests are discussed here. They are numbered G1-S1 to G1-S5. The corresponding testing parameters are listed in Table 3.1. Figures 3.6 and 3.7 are the test results of G1-S1, showing an example of test records with sinusoidal excitations.

Tests with Type 2 Vibration: Earthquake-type Excitations

Table 3.2 gives the testing parameters of three tests, which are numbered G1-E1 to G1-E3. Typical test results are shown in Figures 3.8 and 3.9, which are from G1-E1.

The results of the other tests will be presented with the simulated results later.

From the tests, it is observed that the sliding block undergoes stick-slip type displacements (e.g., Figures 3..7(b) and 3.9(b)). When the excitation is not strong enough, the block is in the rest phase, in which no sliding occurs and the absolute acceleration of the block is the same as that of the inclined plate. When the

exciting force is big enough to overcome the friction force, the block enters the sliding phase. That is, sliding takes place and the absolute acceleration is different from that of the plate. On the recorded accelerogram of the block (e.g., Figures 3..7(a) and 3.9(a)), there appears a cut-off, i.e., asymmetry is found, in terms of amplitude. The acceleration in the upslope direction is smaller than that in the downslope direction. The upslope accelerations get cut off when sliding begins.

3.8 Numerical Simulations

Numerical simulations were carried out by using the computer program *SLIP-P* described in the previous chapter. Computations were performed for all the cases encountered in the shaking table tests, which had various values of the parameters involved in the model. Although two values of friction angle (ϕ_1 and ϕ_2) were measured in the testing, and also it is noted that ϕ_1 is larger than ϕ_2 by 3^o to 6.1^o in Tables 3.1 and 3.2, the same ϕ value was used for the static and dynamic friction angles. The values of ϕ used in the simulations are listed in Table 3.3. Those values were chosen to give the best agreement between the final values of the simulated sliding displacements and the measured sliding displacements. It is noted that the resulting values of ϕ are usually between the measured values of ϕ_1 and ϕ_2. The input accelerations used in the computations were those measured in the shaking table tests.

If the sliding acceleration of the block is $\ddot{x}$, then the acceleration (in the inclined direction) measured by the accelerometer mounted on the back of the block will be

$$A_{bi} = A_h \cos\theta + \ddot{x} \qquad (3.1)$$

This is the component of acceleration used in the comparisons.

Numerical simulations have been performed for both Type 1 vibration (sinusoidal excitations) and Type 2 vibration (the earthquake records).

All the results of the numerical simulations are illustrated in Figures 3.10 to 3.25 along with the testing results.

3.9 Comparison and Discussion of Results

The results of the numerical simulations have been compared with those of the shaking table tests. It is found that 1) in general the agreement is good, 2) some discrepancies exist, which might result from: a) noise level of output signals, b) the assumption in the numerical simulation that the static friction angle is equal to the dynamic friction angle, so that a single parameter is used to represent frictional resistance; and c) measurement of friction angle.

Of course, the good agreement obtained between the simulated displacements and those from the tests resulted from a fitting process involving ϕ. In addition, recall from the previous Chapter that the response is very sensitive to the values of ϕ.

The findings in this investigation increase understanding of the failure mechanism and response characteristics of earth structures which experience stick-slip type deformations. The accelerogram records obtained from such structures may show asymmetry in amplitude for which the model tests offer an

explanation. Furthermore, the yield acceleration can be ascertained using the results of the investigation. The developed computer programs can be used to evaluate seismically-induced permanent displacements in dams or other earth structures, although great care must be taken because of the sensitivity of the results with the friction angle.

Test No.	A_m (g)	f (Hz)	T_d (sec)	θ (degree)	ϕ_1 (degree)	ϕ_2 (degree)
G1-S1	0.5	5	47.65	10	—	—
G1-S2	0.5	30	24.33	10	18.9	25.0
G1-S3	0.5	20	24.33	10	26.8	30.0
G1-S4	0.5	10	24.33	10	23.6	28.6
G1-S5	0.35	10	24.33	10	23.5	28.5

Table 3.1 Parameters in tests with sinusoidal excitations.

Test No.	A_{dl}^* (g)	T_d (sec)	θ (degree)	ϕ_1 (degree)	ϕ_2 (degree)
G1-E1	0.9	4.87	10	23.5	29.0
G1-E2	0.5	24.33	10	26.0	29.0
G1-E3	0.4	47.65	10	—	—

A_{dl}^* is the dynamic level set on the controller to determine the peak value of acceleration shaking table.

Table 3.2 Parameters in tests with earthquake-type excitations.

Test No.	ϕ(degree)
G1-S1	19.1
G1-S2	19.5
G1-S3	27.9
G1-S4	23.7
G1-S5	23.3
G1-E1	24.0
G1-E2	26.5
G1-E3	21.6

Table 3.3 Value of ϕ used in simulations.

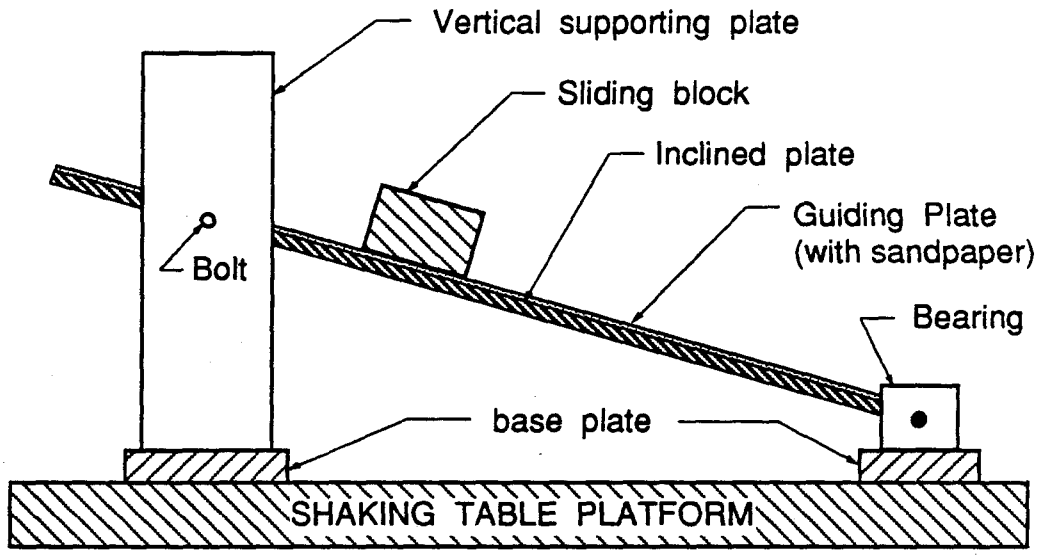

(a) Side view

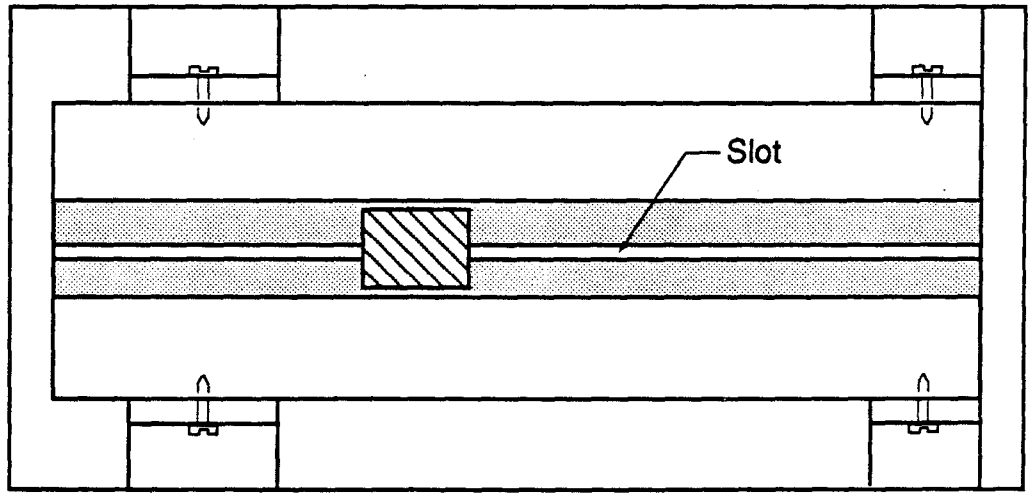

(b) Top view

Figure 3.1 Experimental setup of the model: (a) side view; and (b) top view.

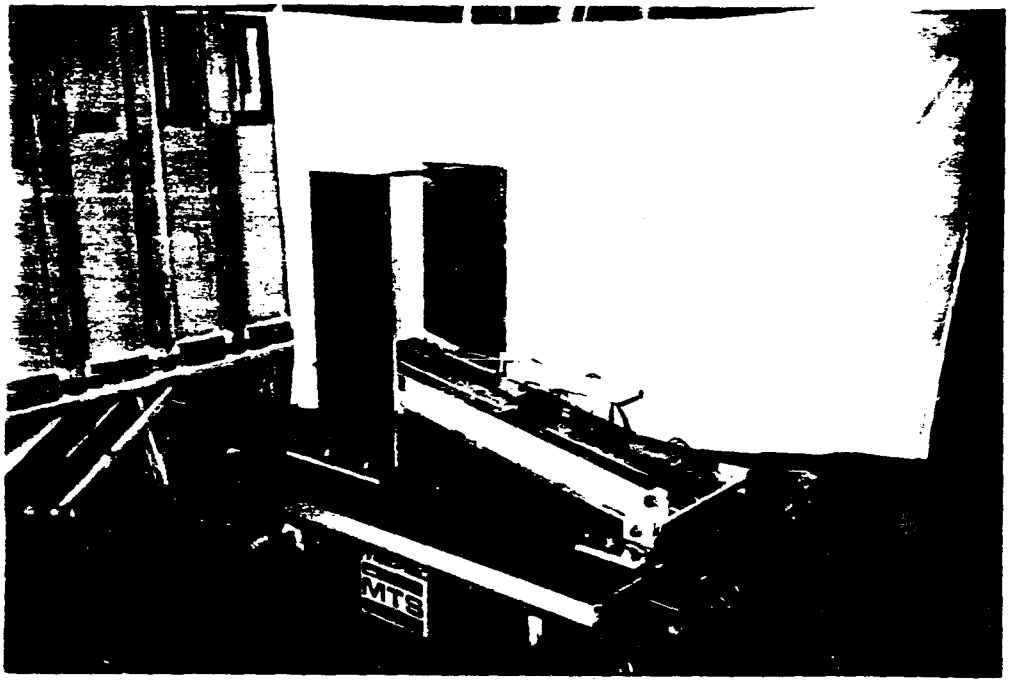

(a)

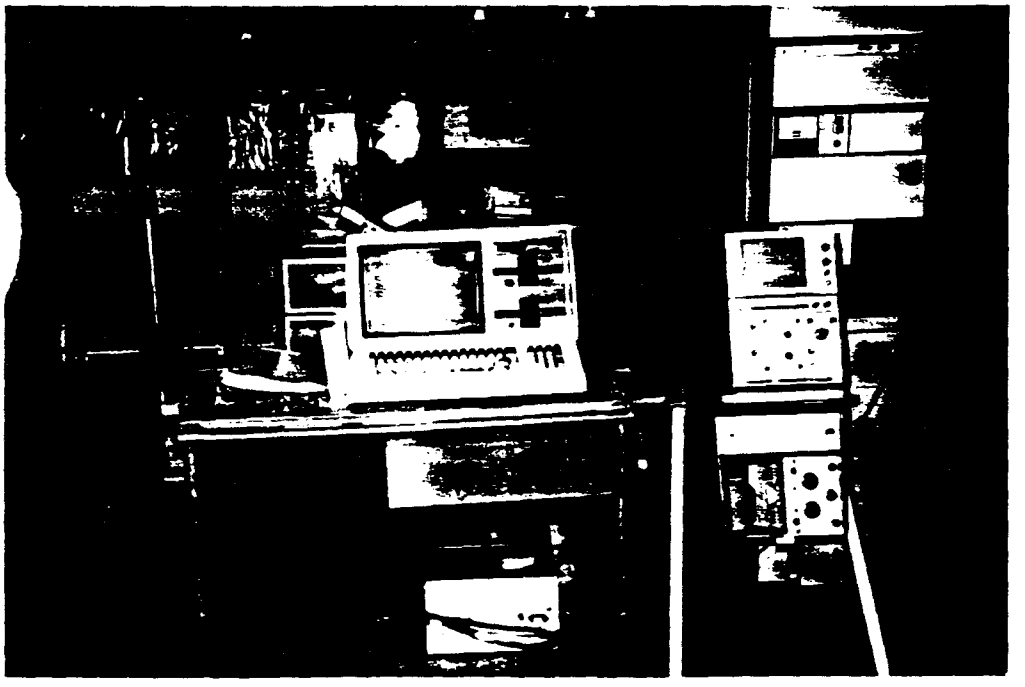

(b)

Figure 3.2 Photos: (a) the testing model on the table; and (b) the console of the vibration system, the computer and the DAC.

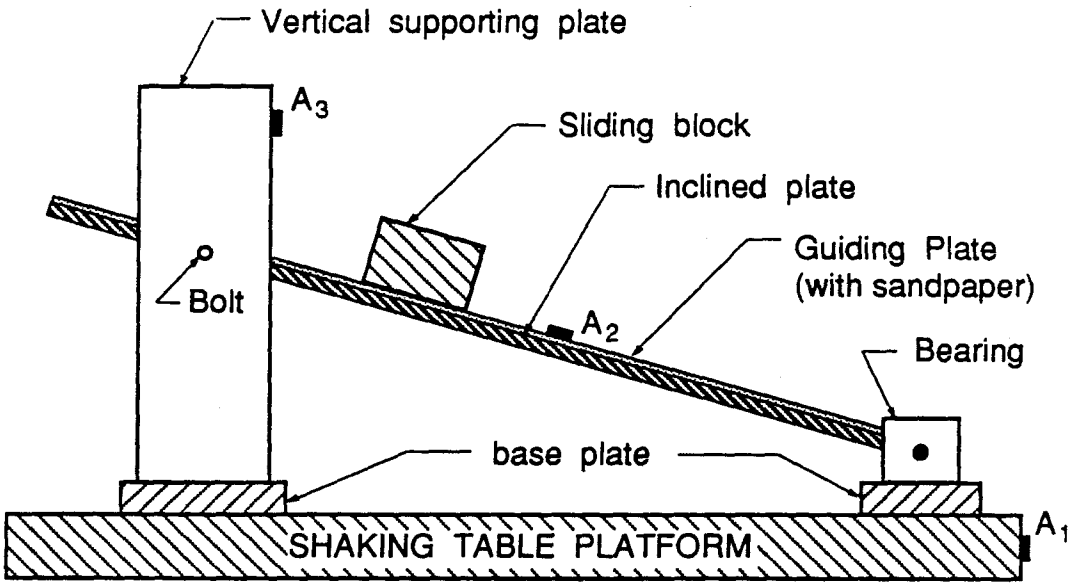

(a) Side view

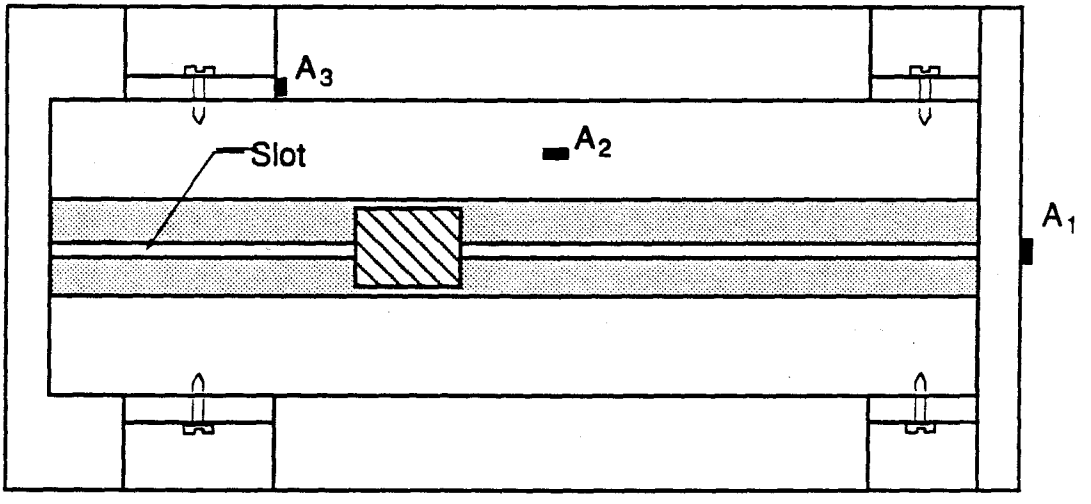

(b) Top view

A_1, A_2, A_3 : accelerometer

Figure 3.3 Location of accelerometers for frequency sweep.

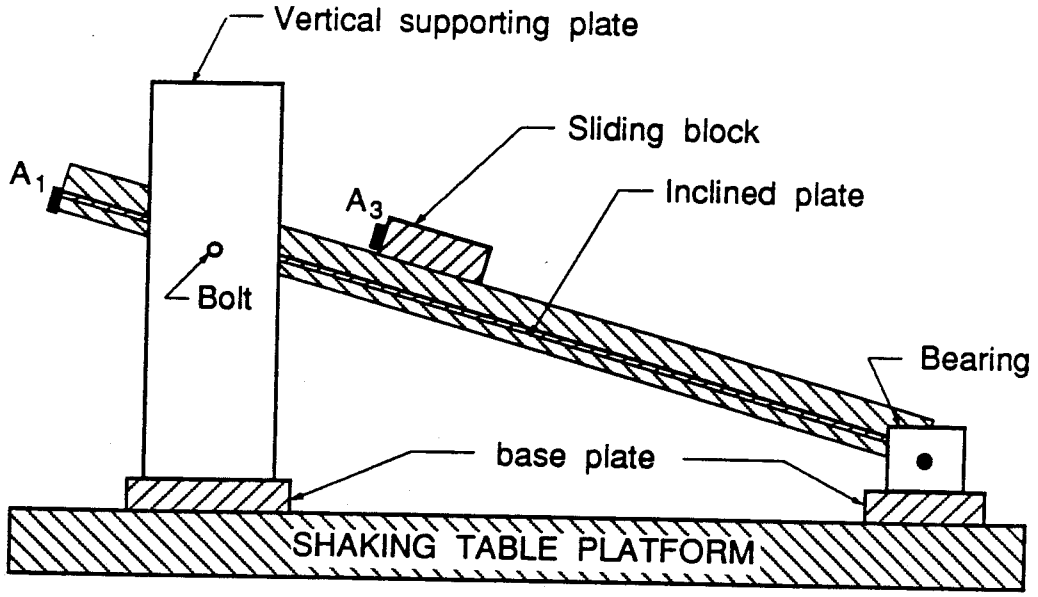

(a) Side view

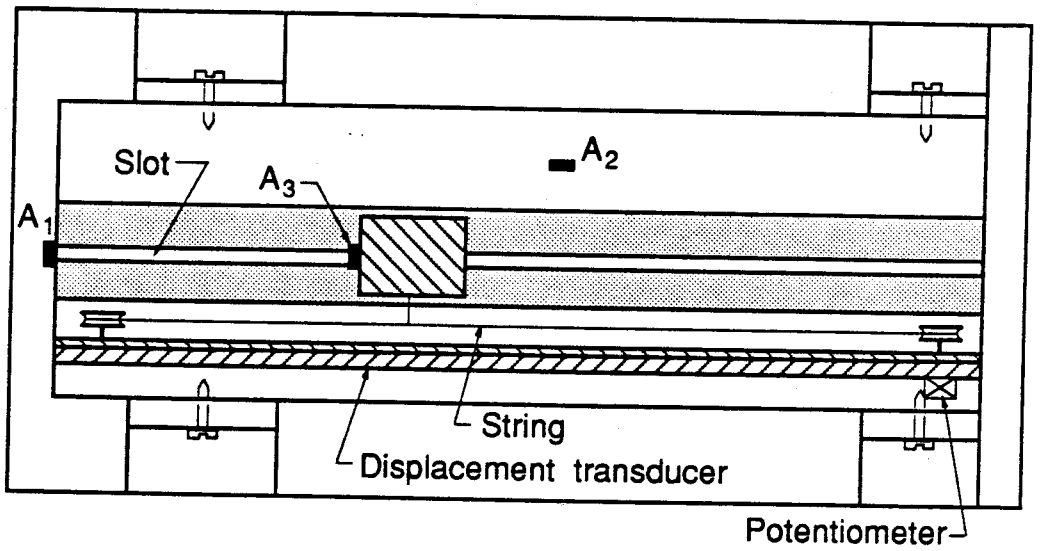

(b) Top view

A_1, A_2, A_3 : accelerometer

Figure 3.4. Location of transducers for vibration tests.

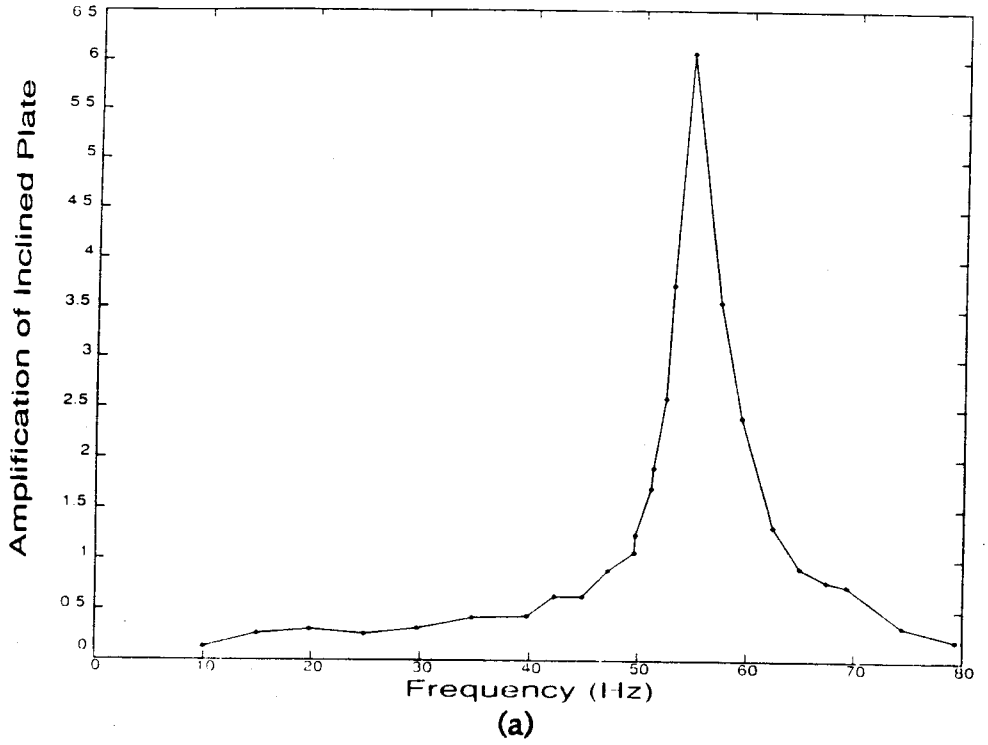

Figure 3.5 Frequency response curves from the frequency sweep tests for the model of (a) the inclined plate; and (b) the vertical supporting plate.

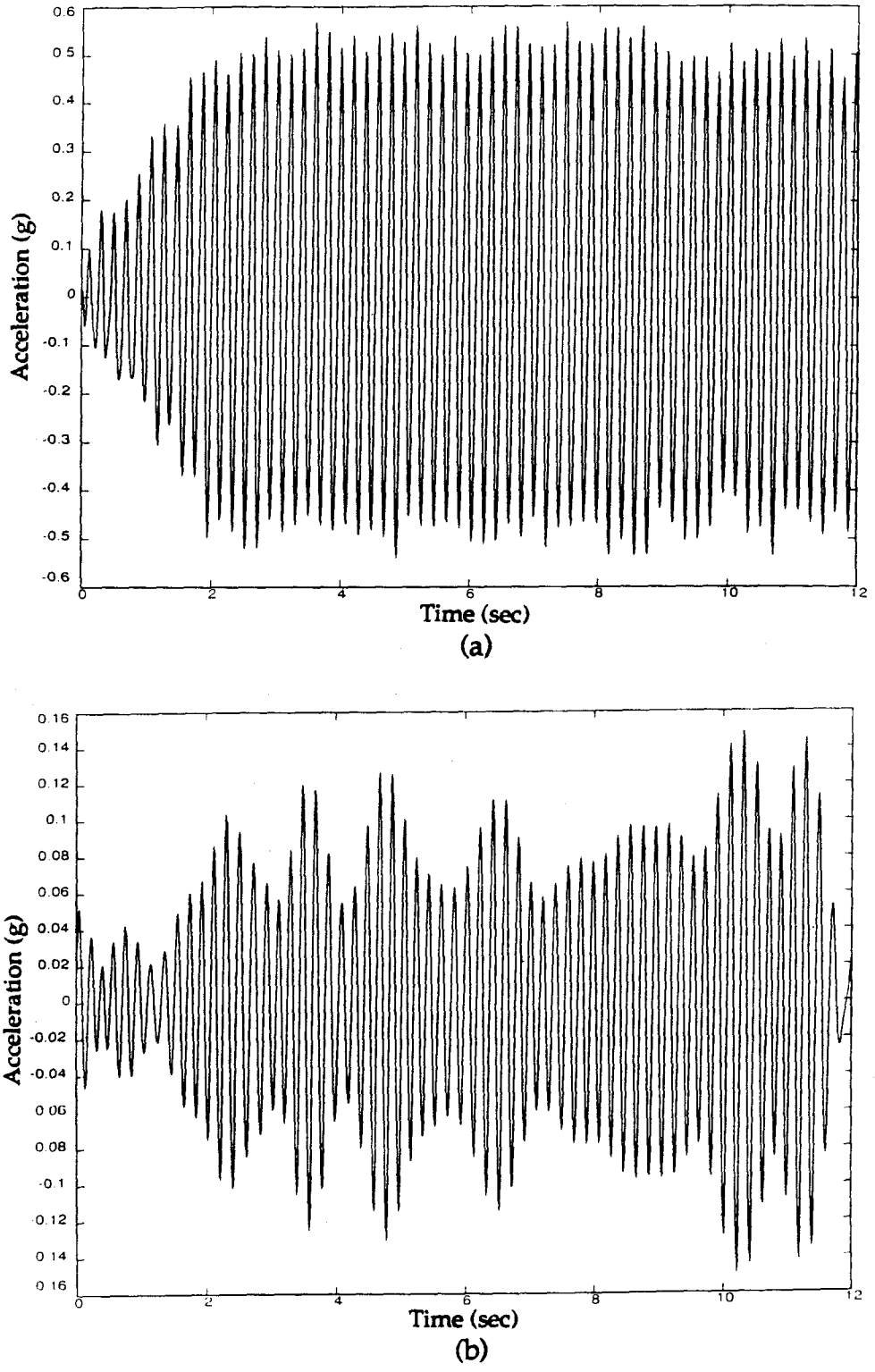

Figure 3.6 An example of test records of sinusoidal excitations: (a) record of A_1; and (b) record of A_2.

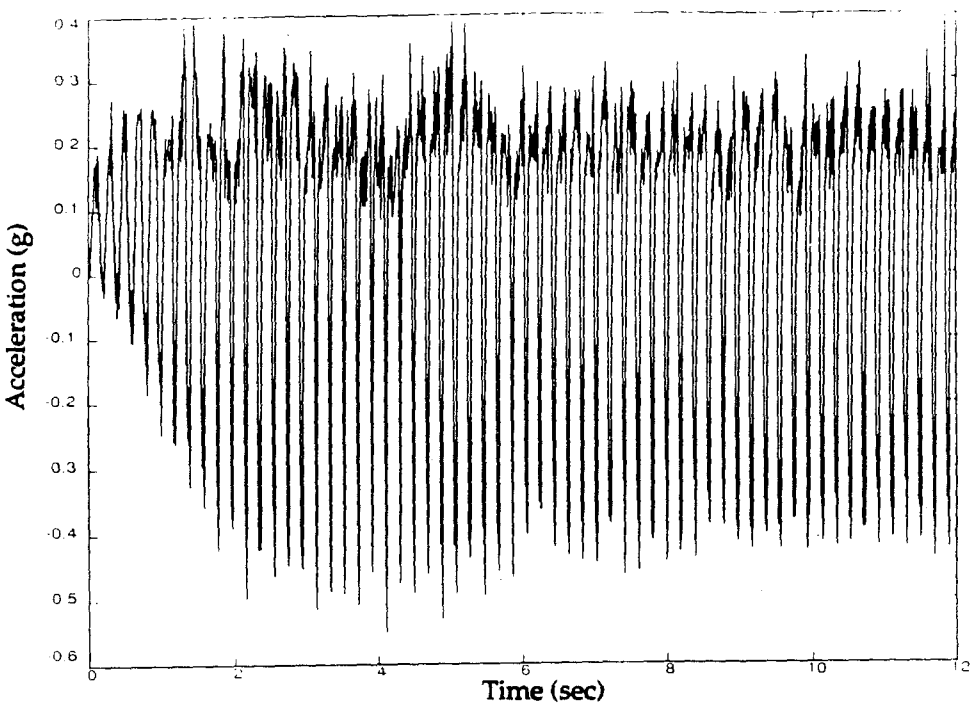

(a)

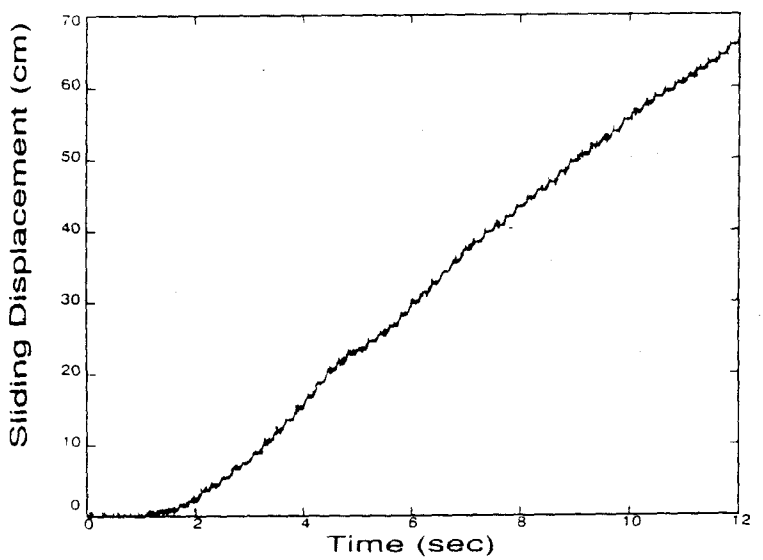

(b)

Figure 3.7 An example of test records of sinusoidal excitations: (a) record of A_3; and (b) record of displacement transducer.

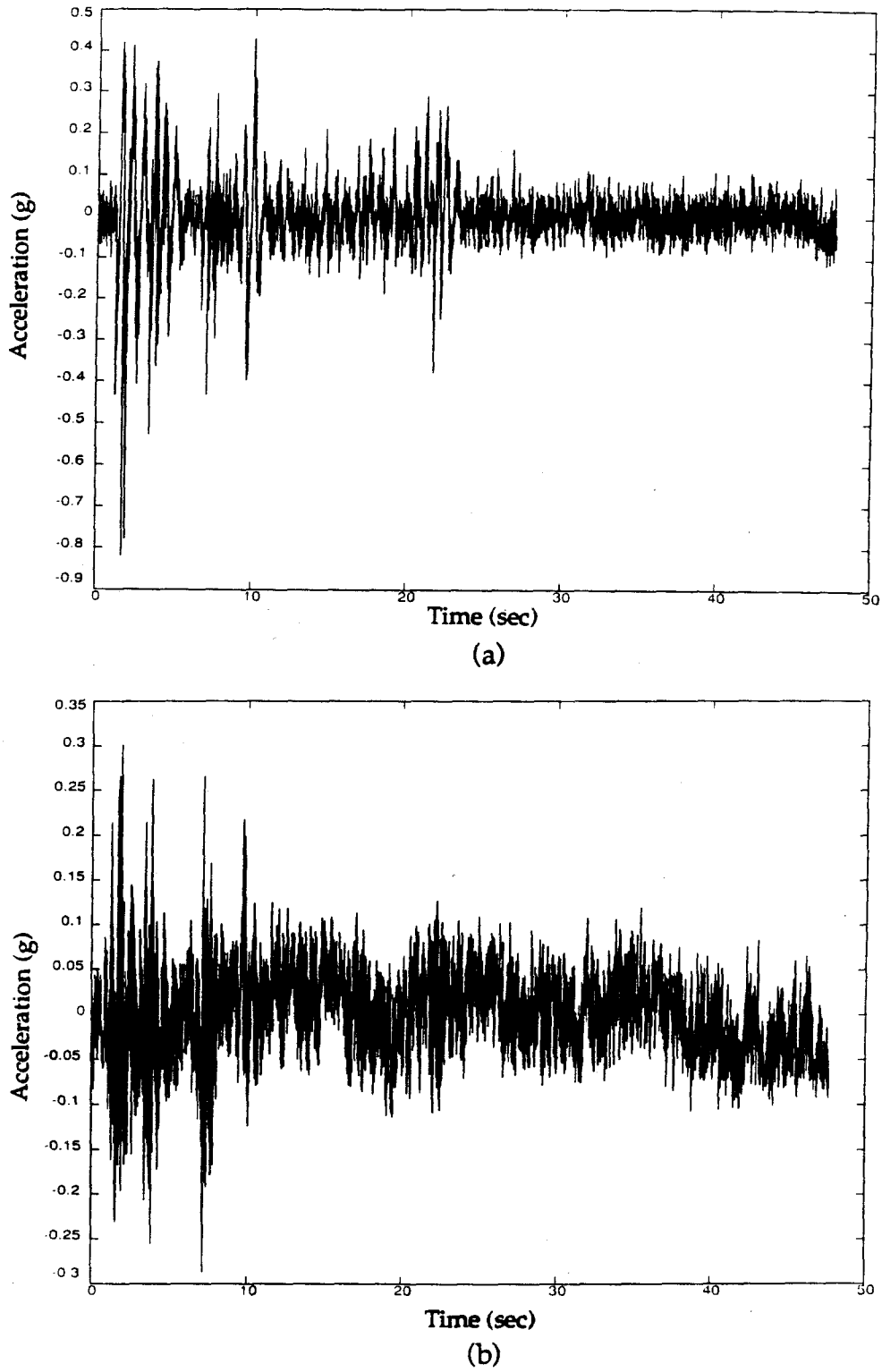

Figure 3.8 Typical test results with earthquake-type excitations: (a) record of A_1; and (b) record of A_2.

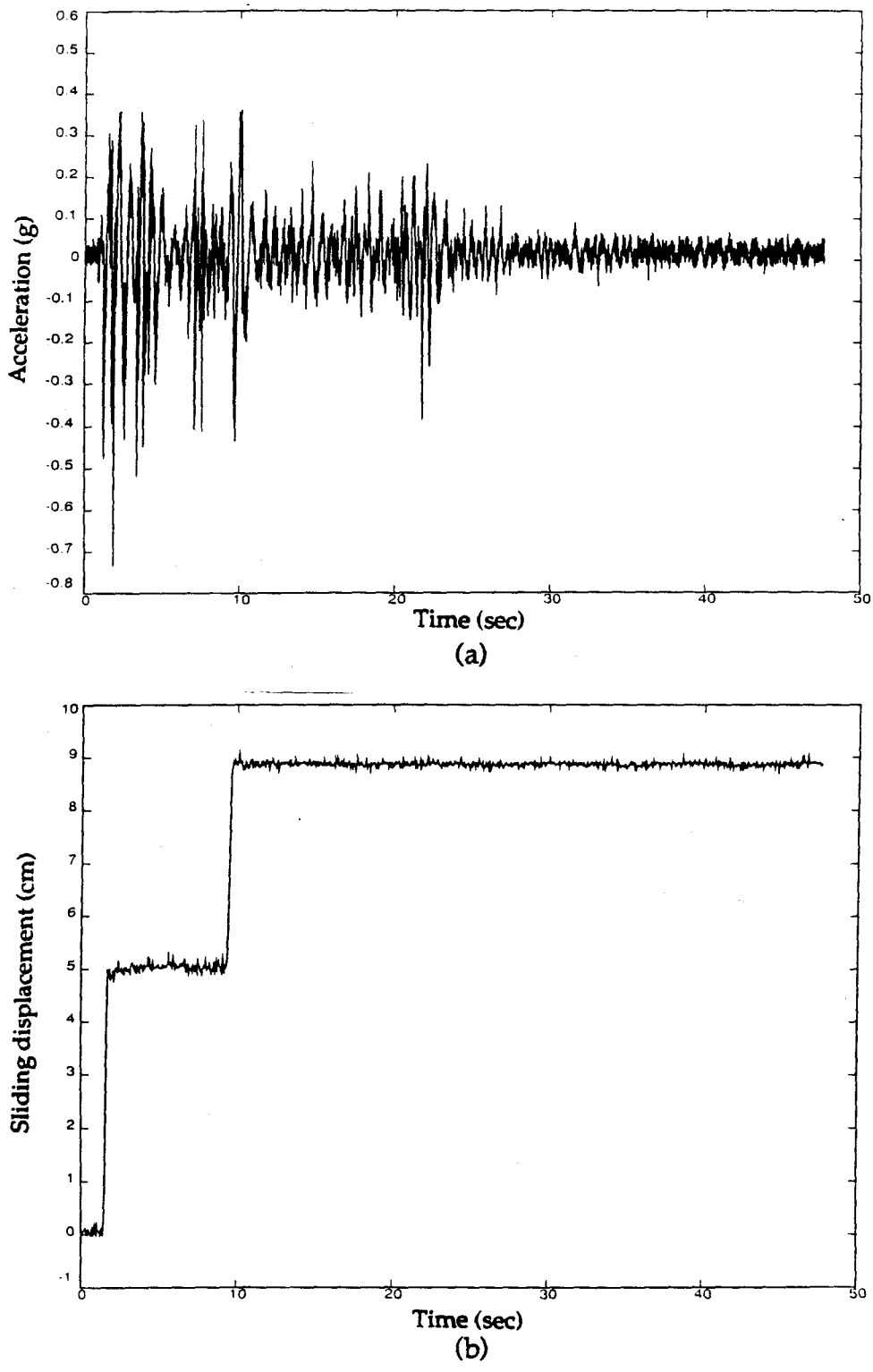

Figure 3.9 Typical test results with earthquake-type excitations: (a) record of A_3; and (b) record of displacement transducer.

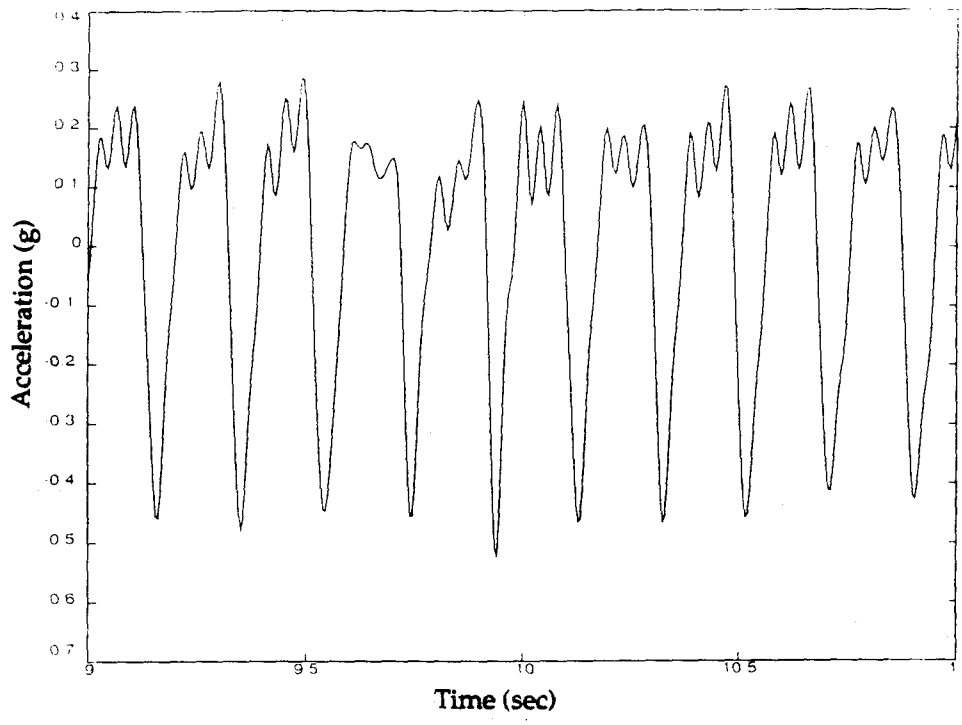

Figure 3.10 Test G1-S1: (a) record of A_3; and (b) simulated block acceleration.

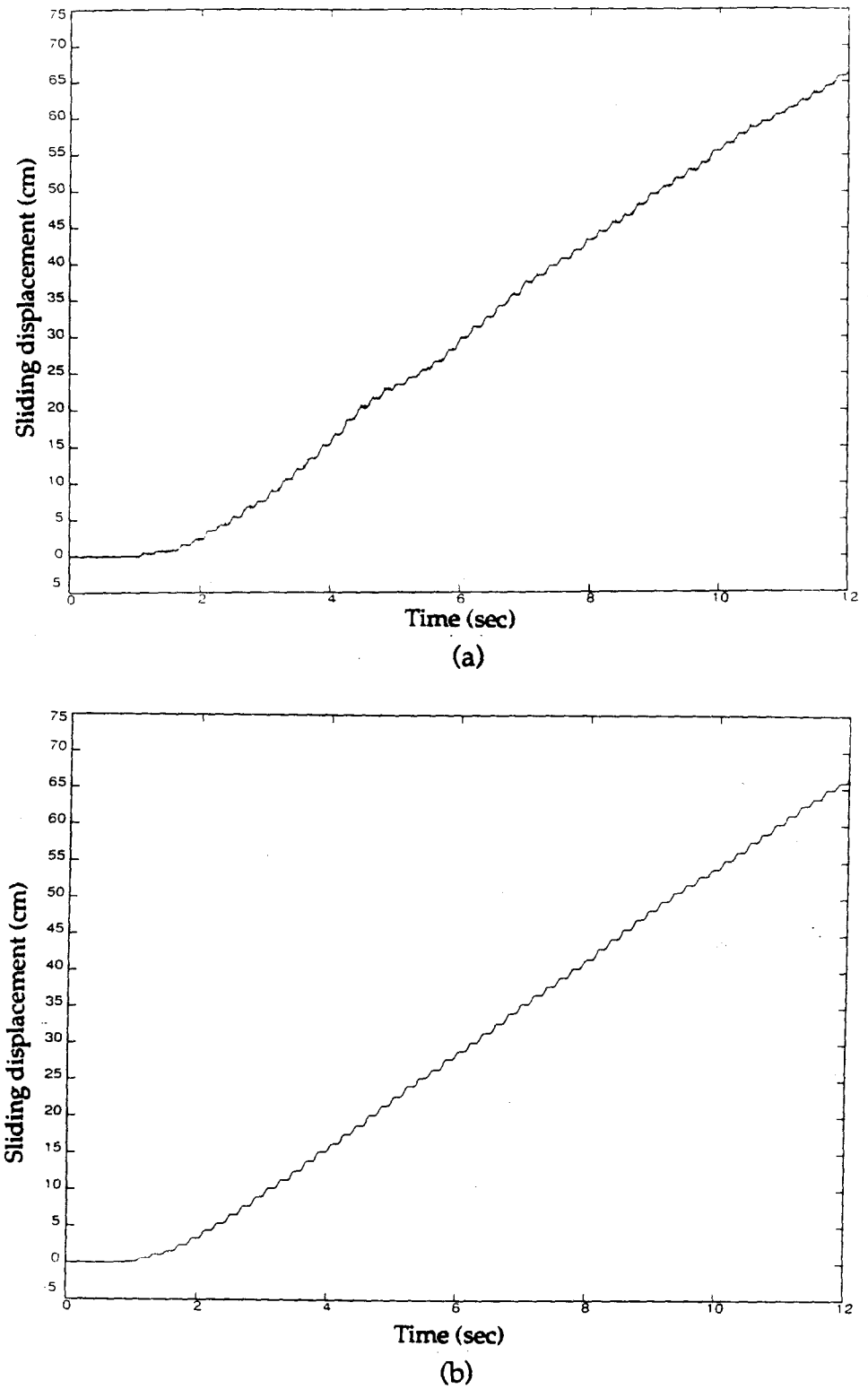

Figure 3.11 Test G1-S1: (a) record of displacement transducer; and (b) simulated sliding displacement.

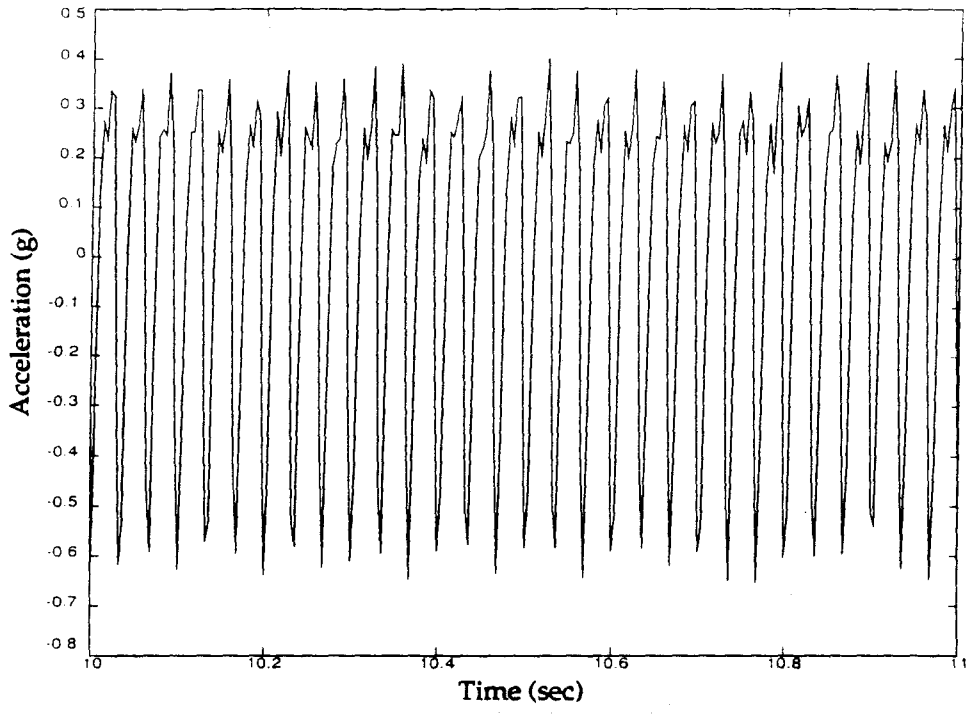

(a)

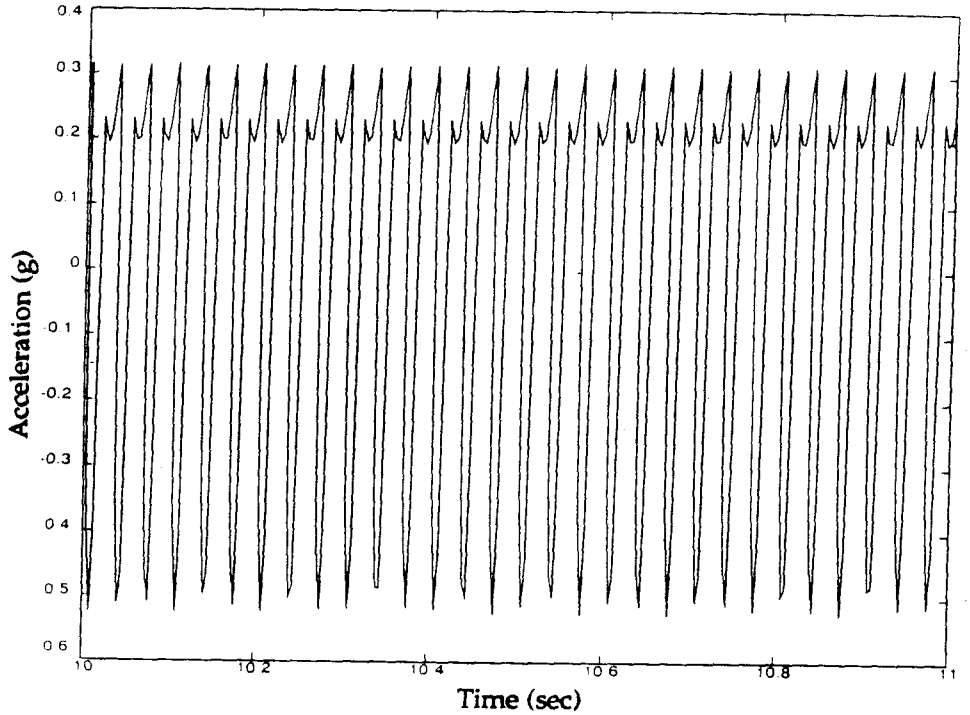

(b)

Figure 3.12 Test G1-S2: (a) record of A_3; and (b) simulated block acceleration.

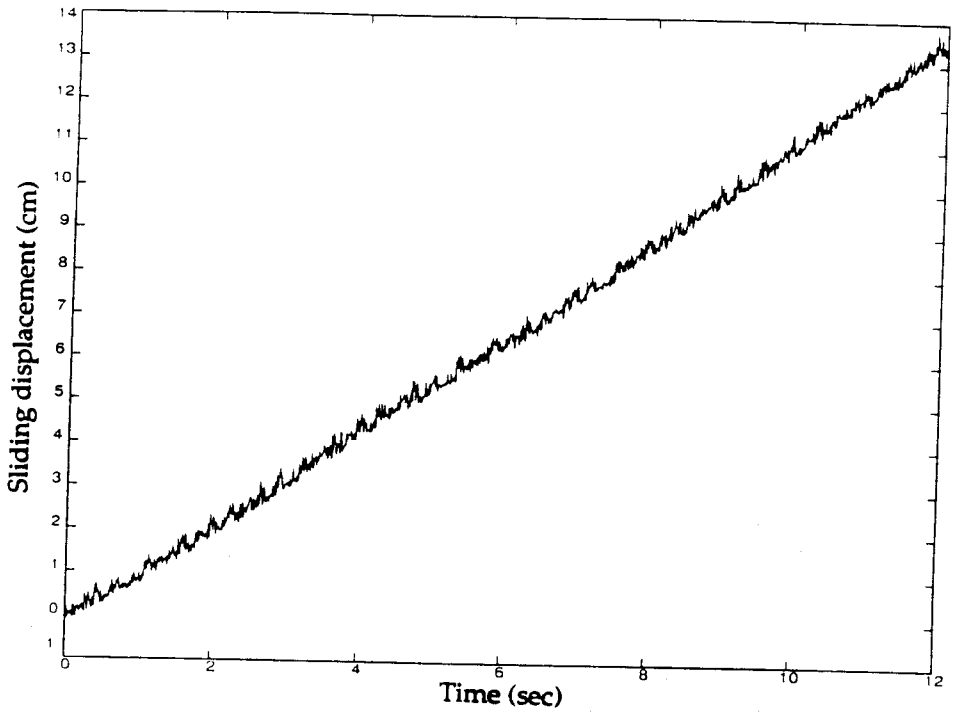

(a)

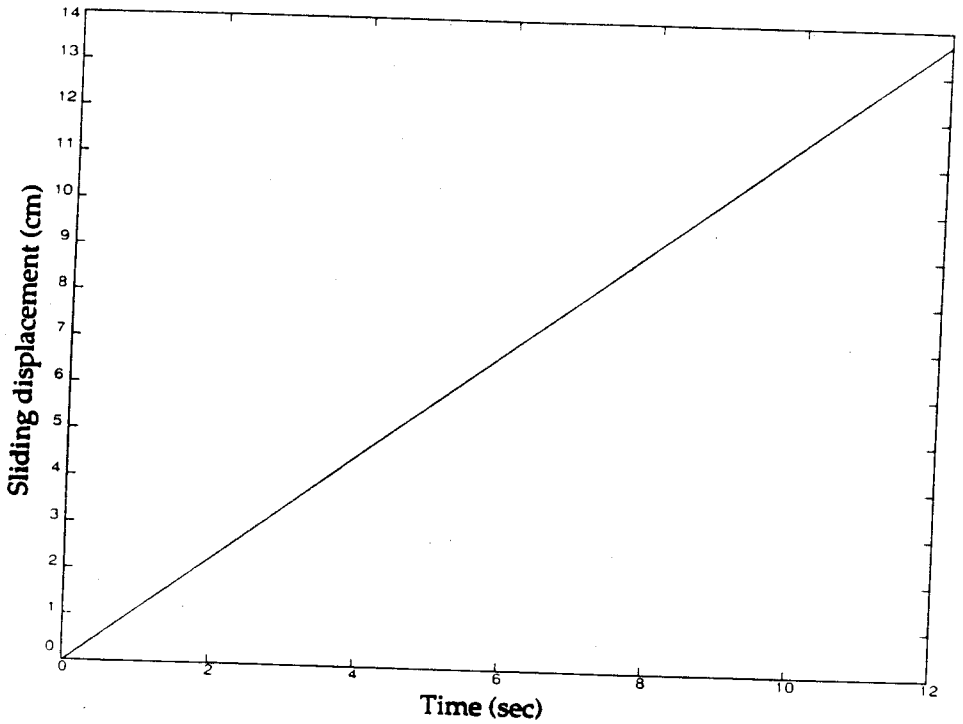

(b)

Figure 3.13 Test G1-S2: (a) record of displacement transducer; and (b) simulated sliding displacement.

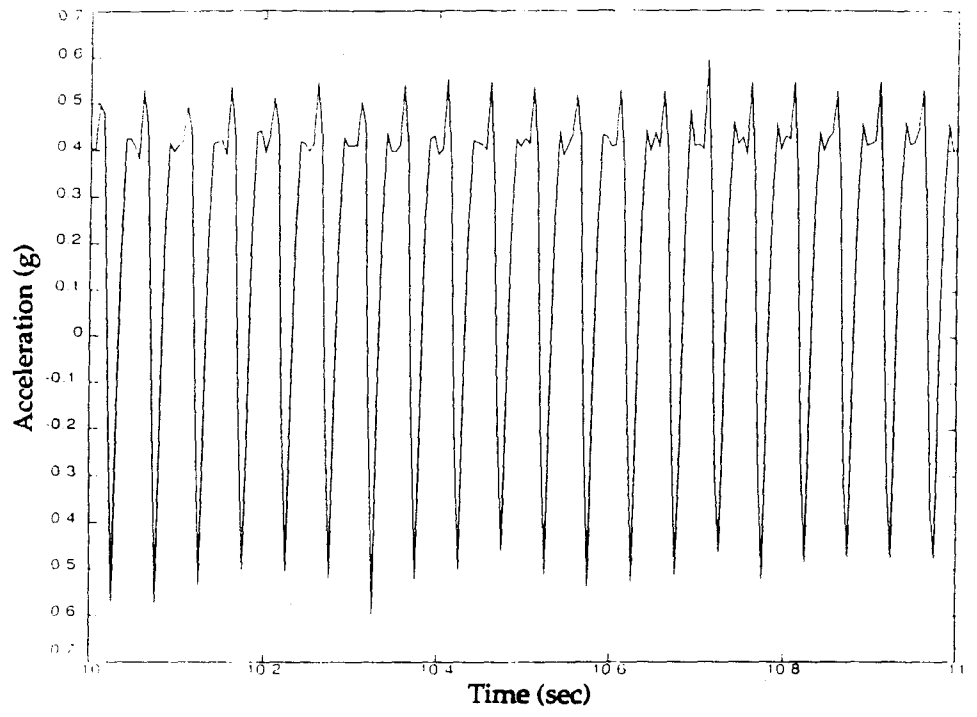

(a)

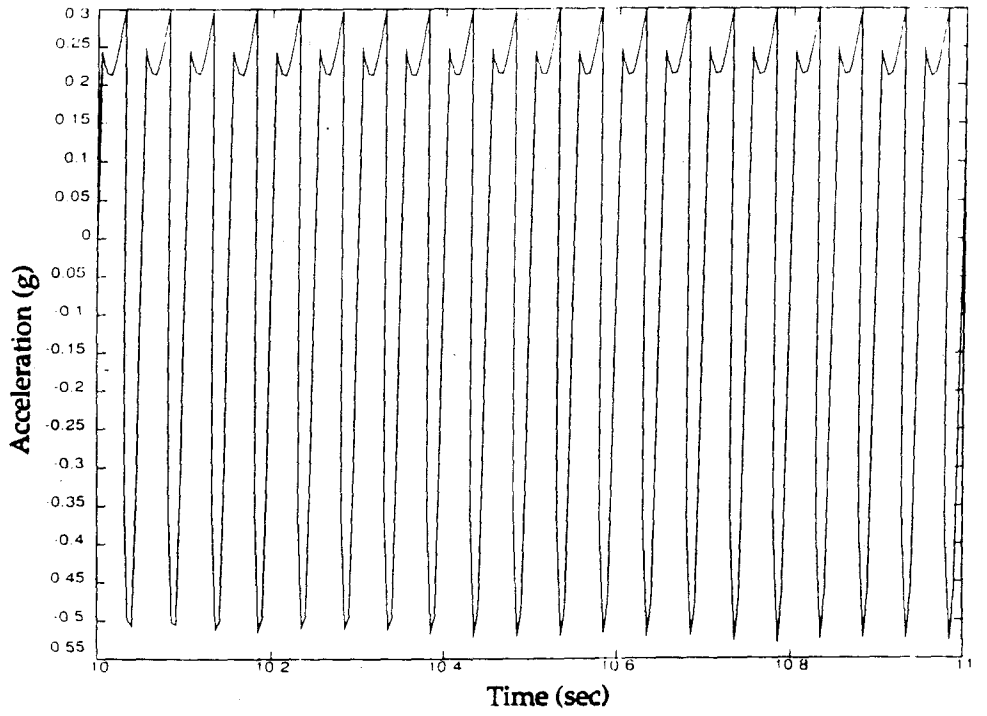

(b)

Figure 3.14 Test G1-S3: (a) record of A_3; and (b) simulated block acceleration.

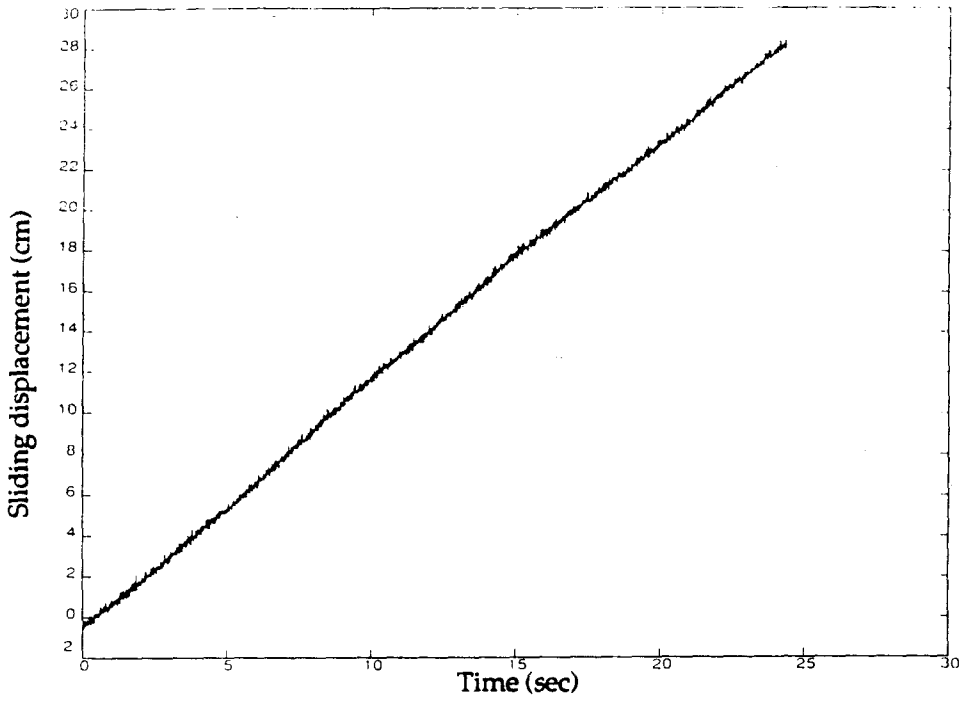

(a)

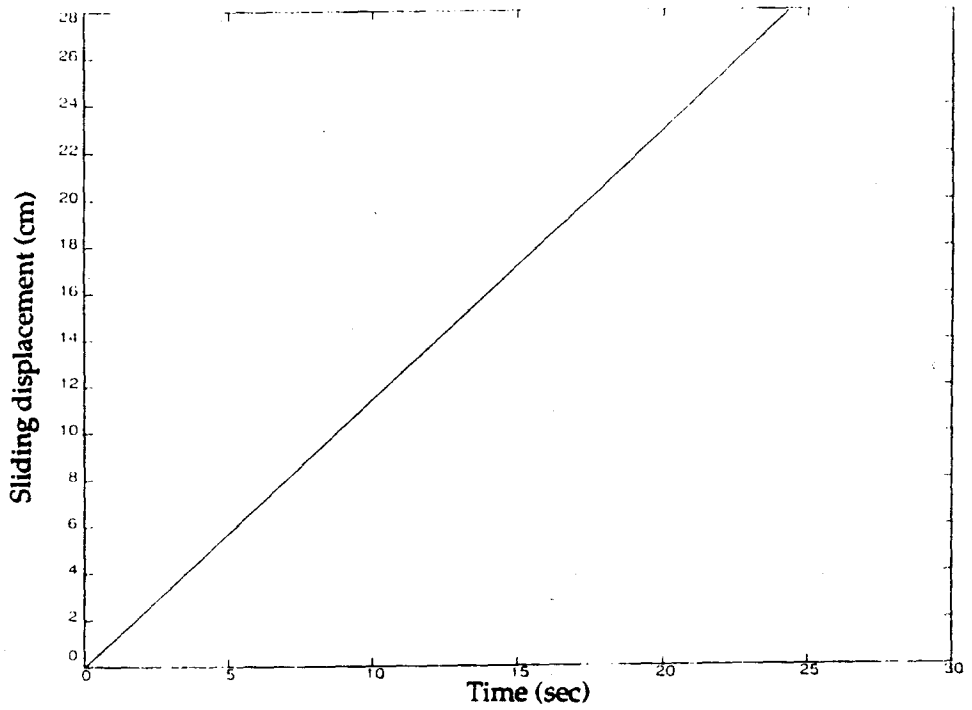

(b)

Figure 3.15 Test G1-S3: (a) record of displacement transducer; and (b) simulated sliding displacement.

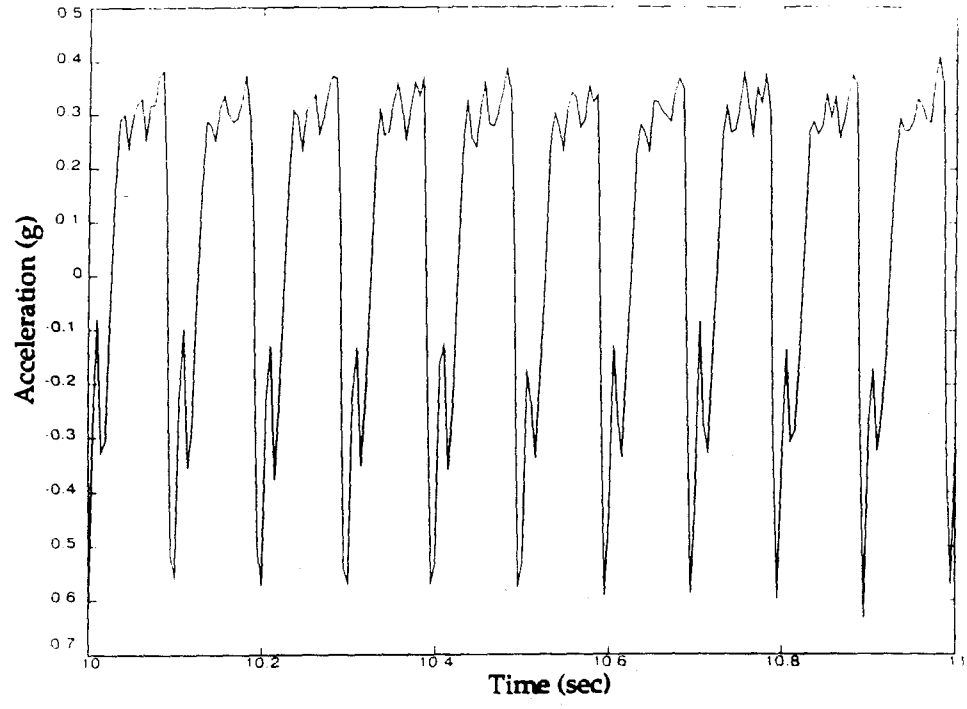

(a)

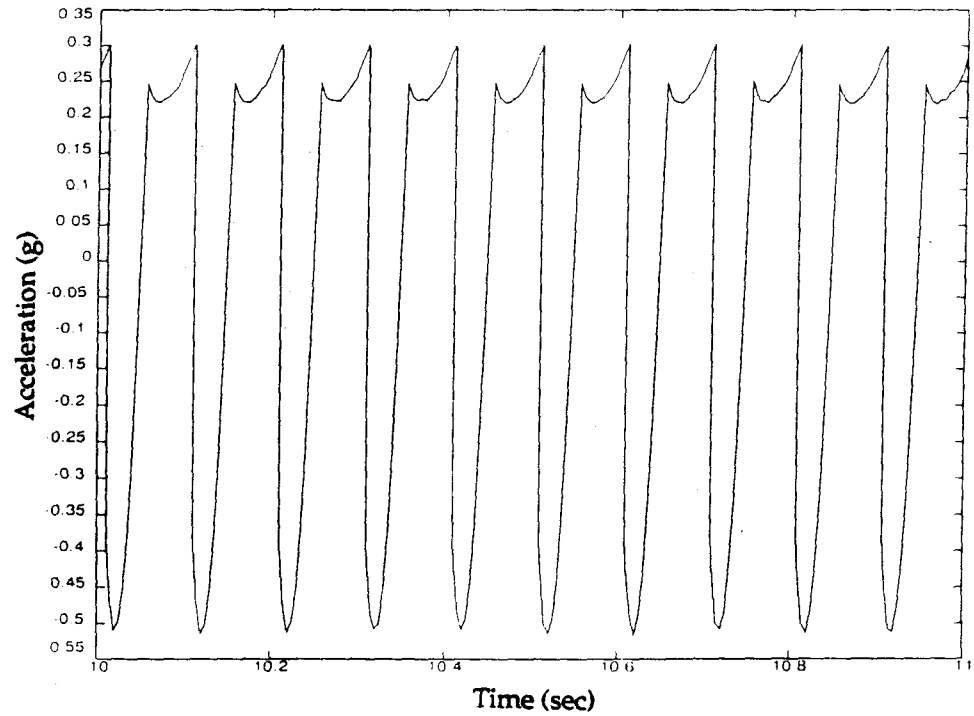

(b)

Figure 3.16 Test G1-S4: (a) record of A_3; and (b) simulated block acceleration.

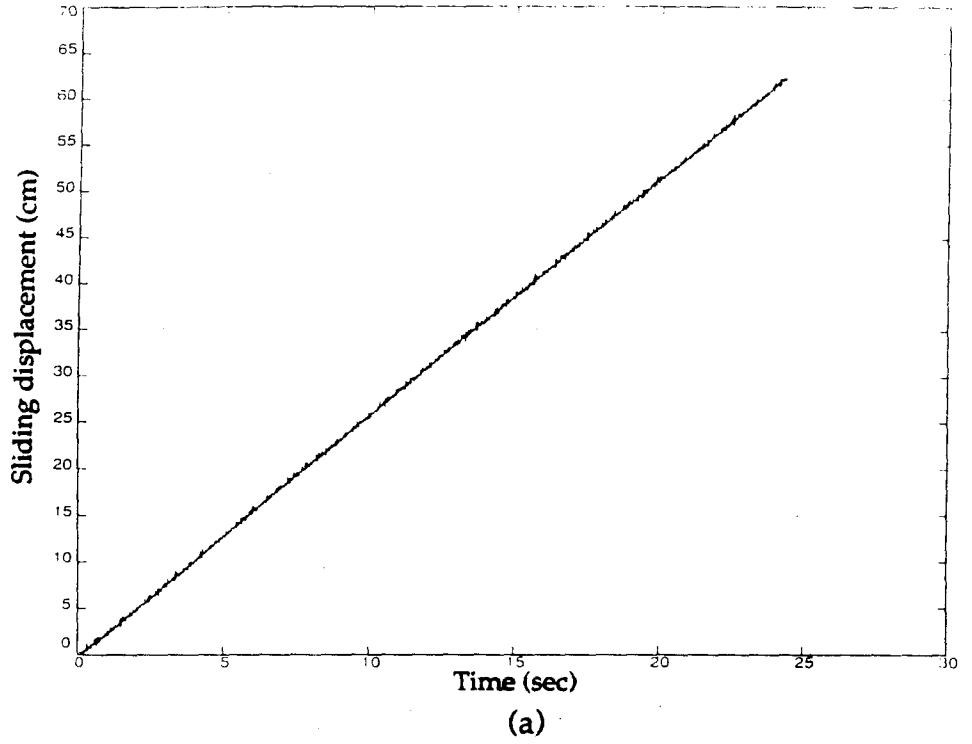

(a)

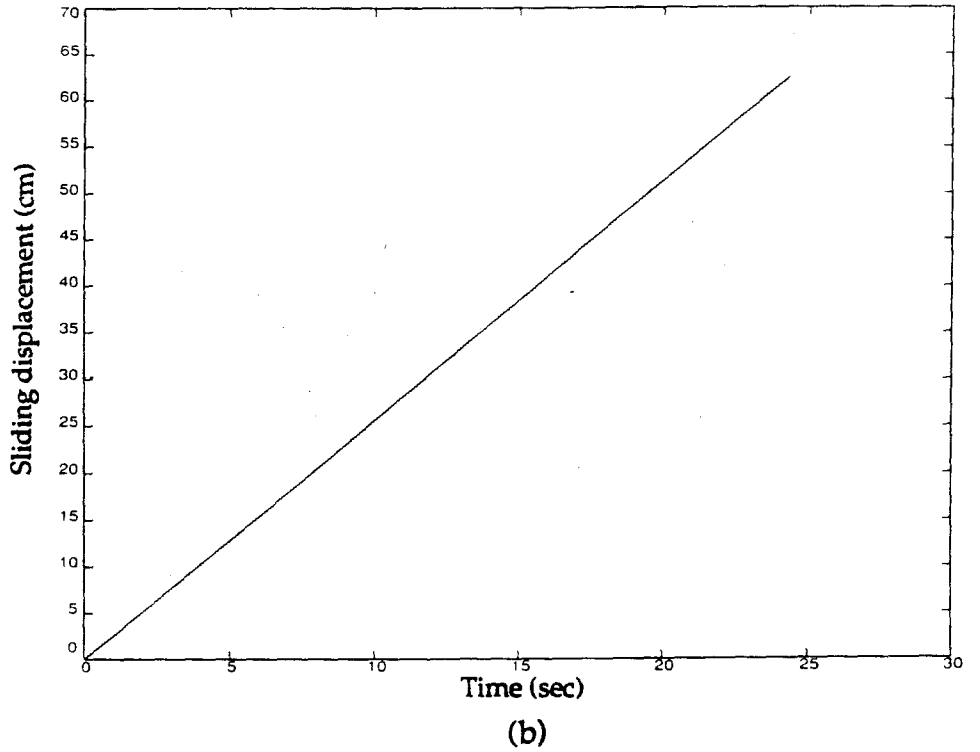

(b)

Figure 3.17 Test G1-S4: (a) record of displacement transducer; and (b) simulated sliding displacement.

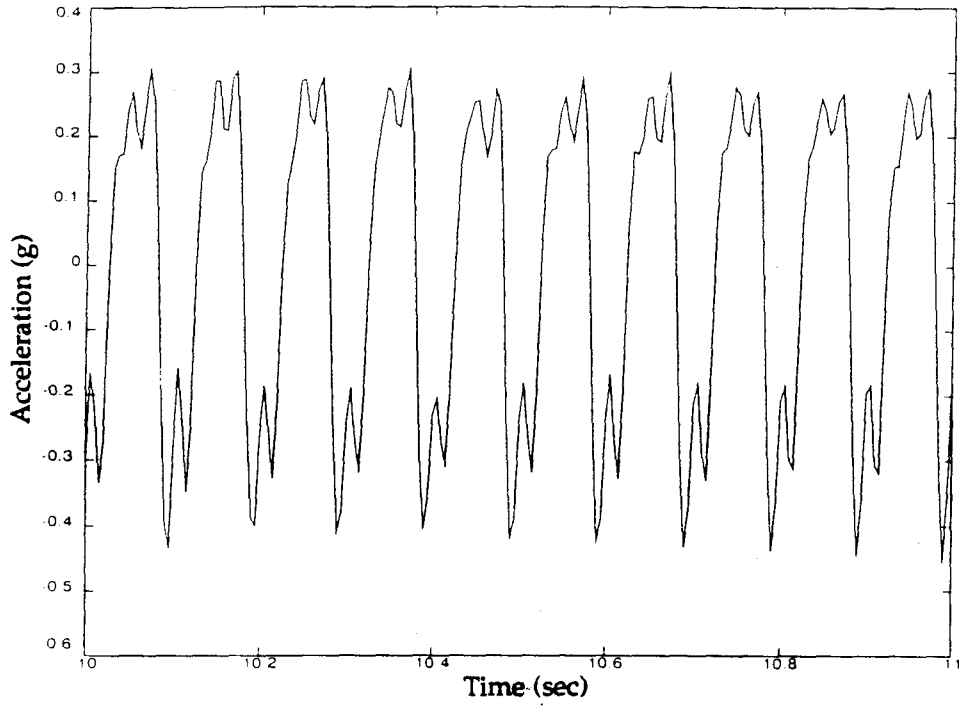

(a)

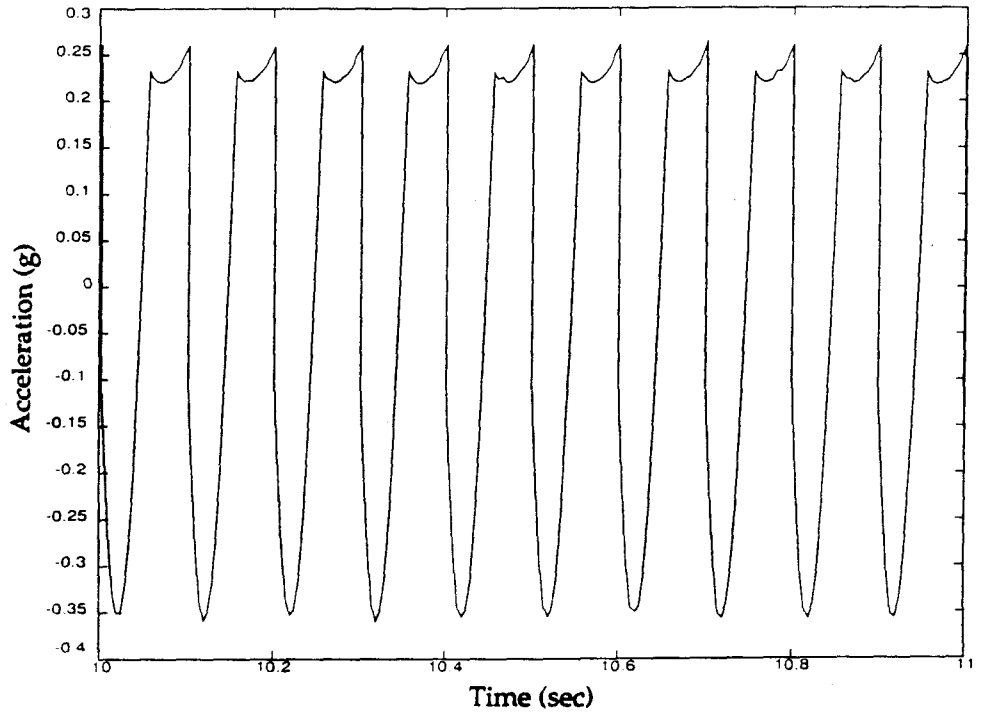

(b)

Figure 3.18 Test G1-S5: (a) record of A_3; and (b) simulated block acceleration.

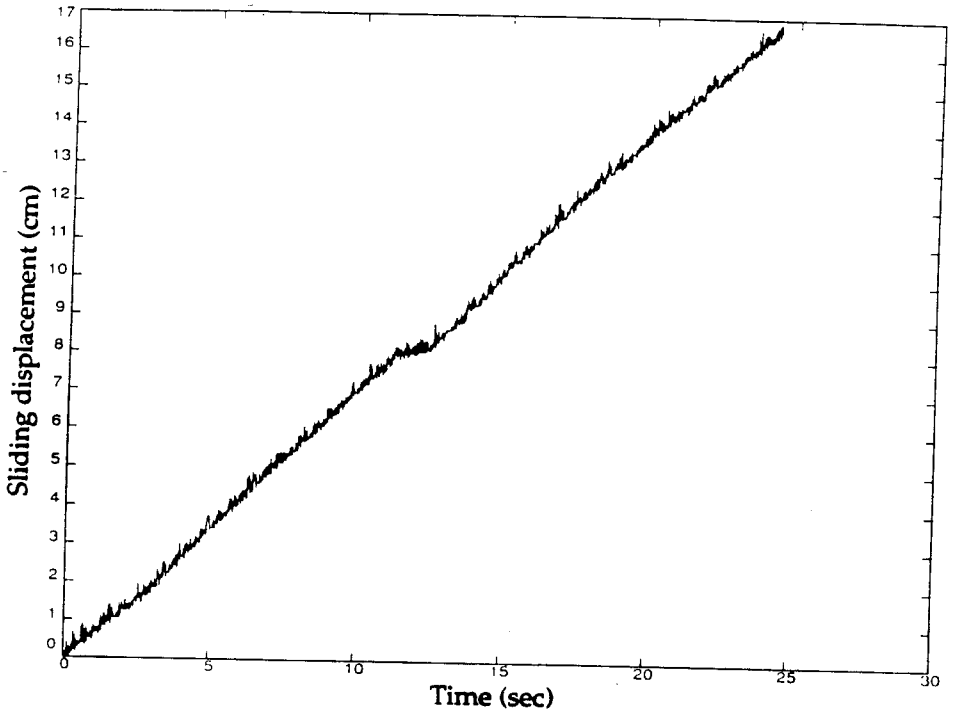

(a)

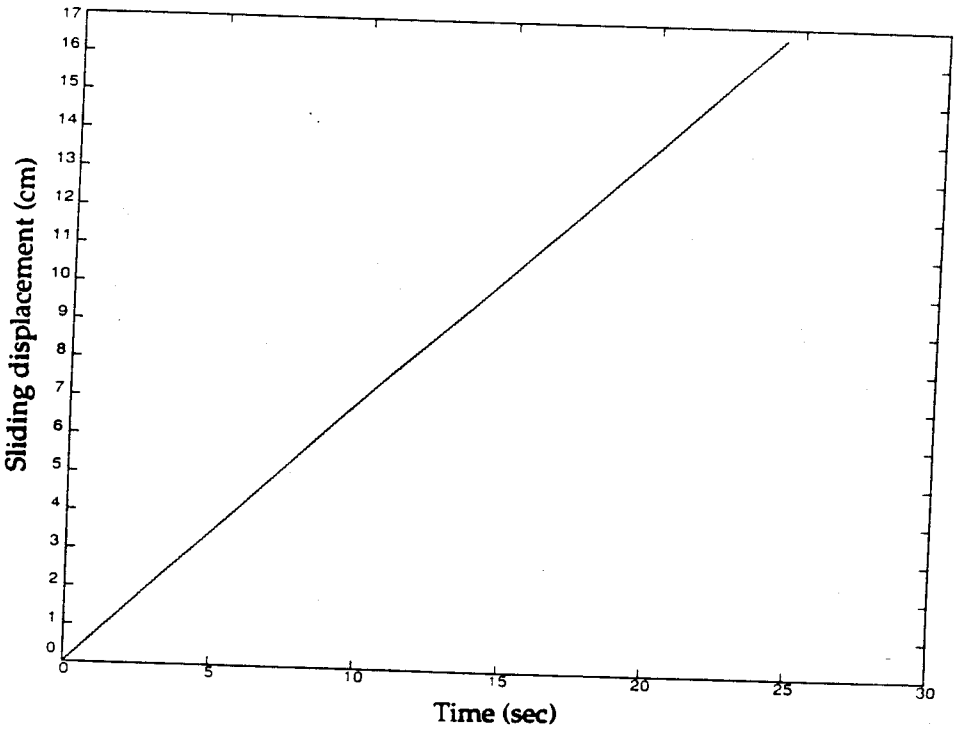

(b)

Figure 3.19 Test G1-S5: (a) record of displacement transducer; and (b) simulated sliding displacement.

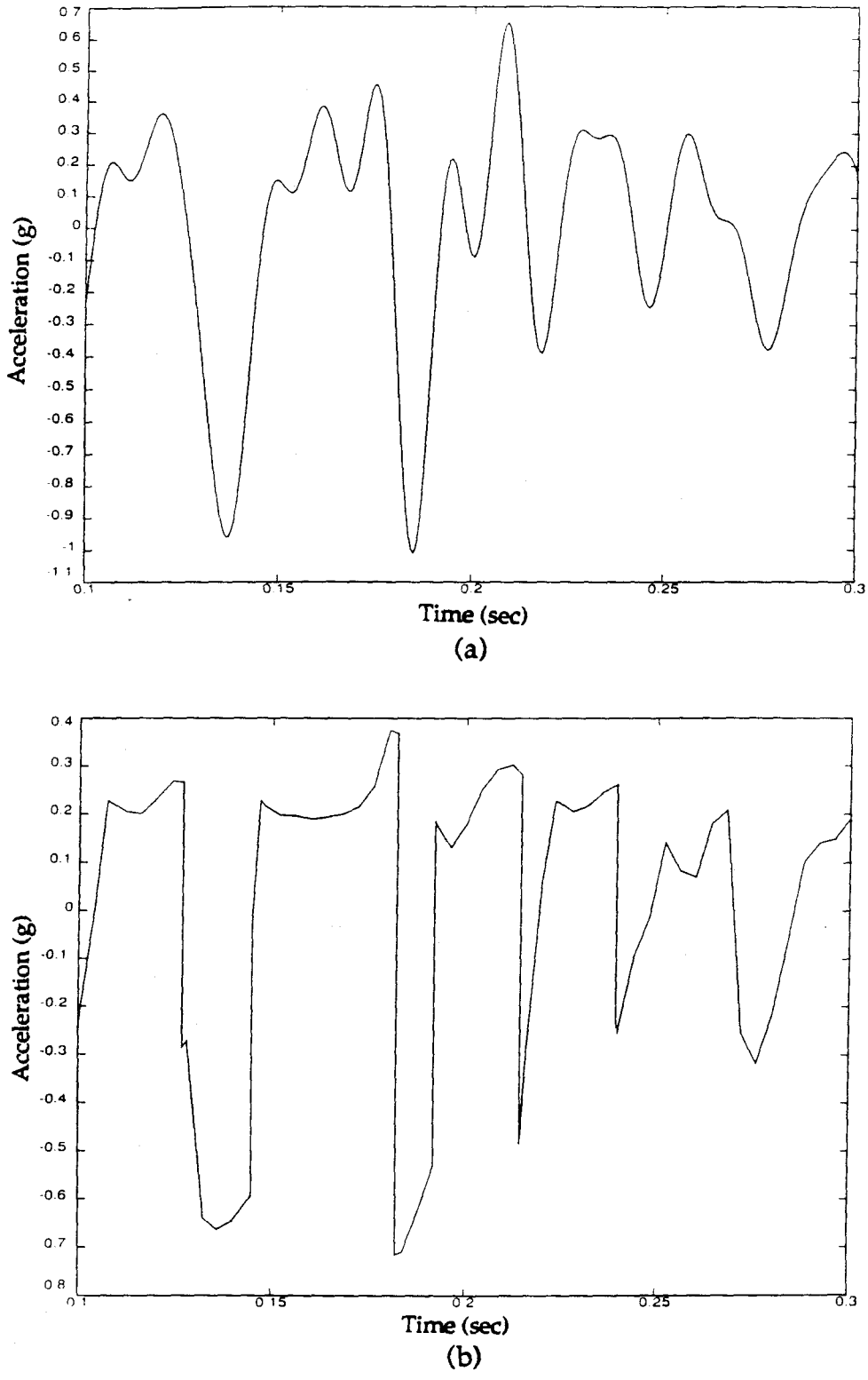

Figure 3.20 Test G1-E1: (a) record of A_3; and (b) simulated block acceleration.

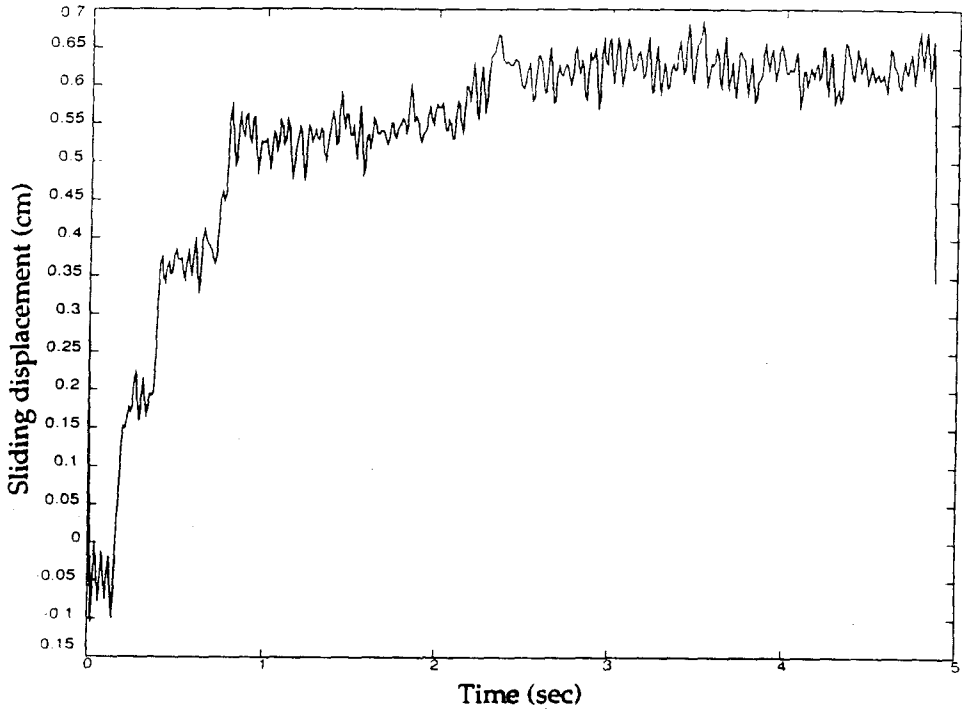

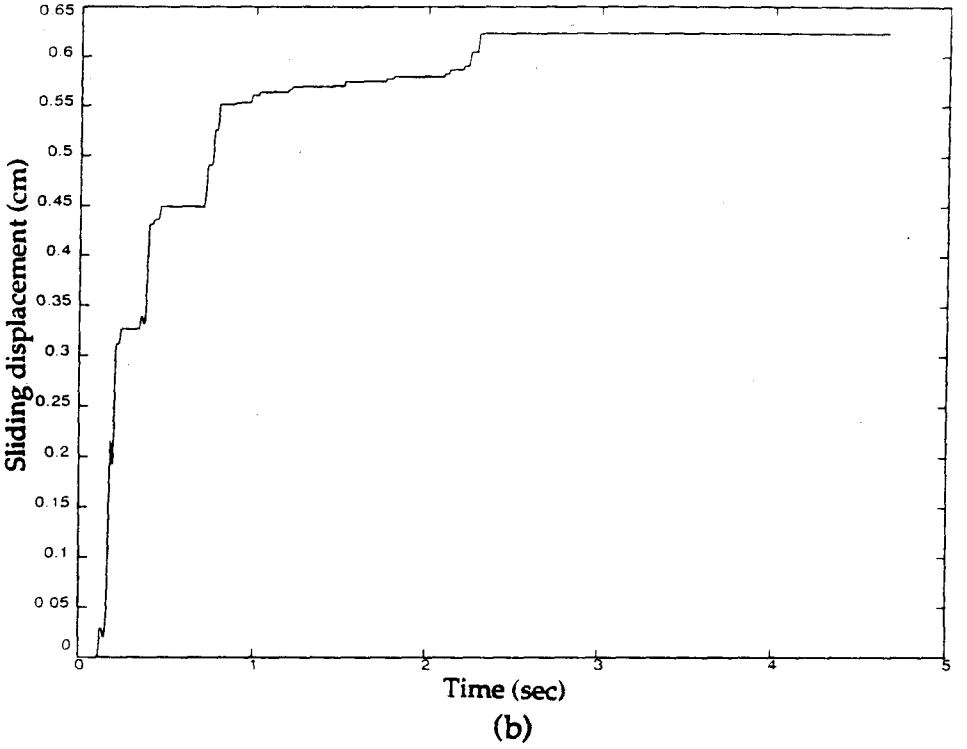

Figure 3.21 Test G1-E1: (a) record of displacement transducer; and (b) simulated sliding displacement.

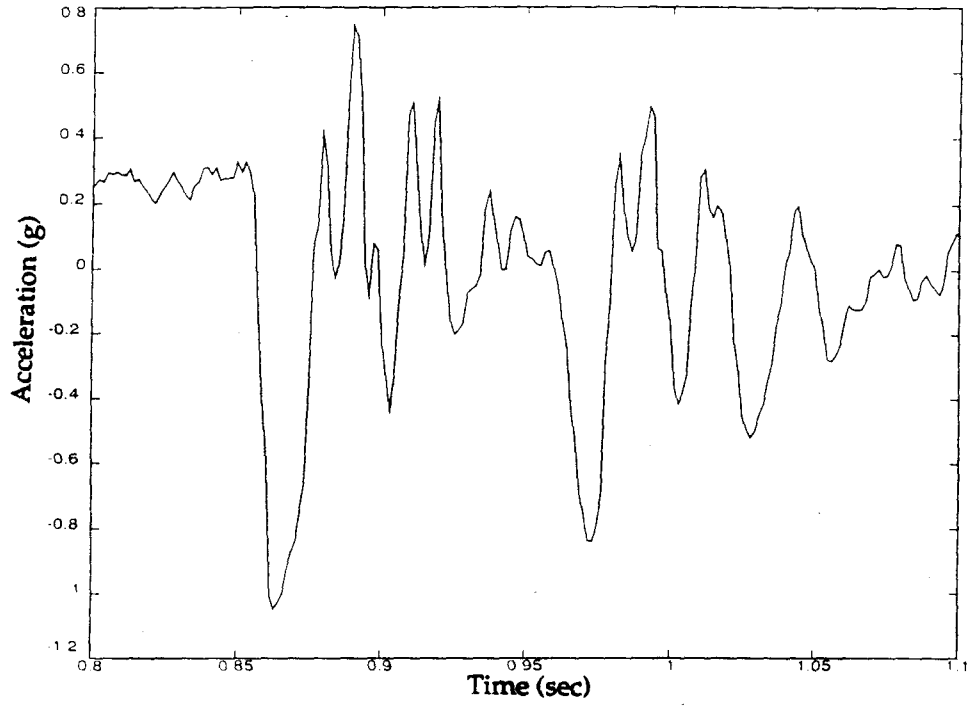

(a)

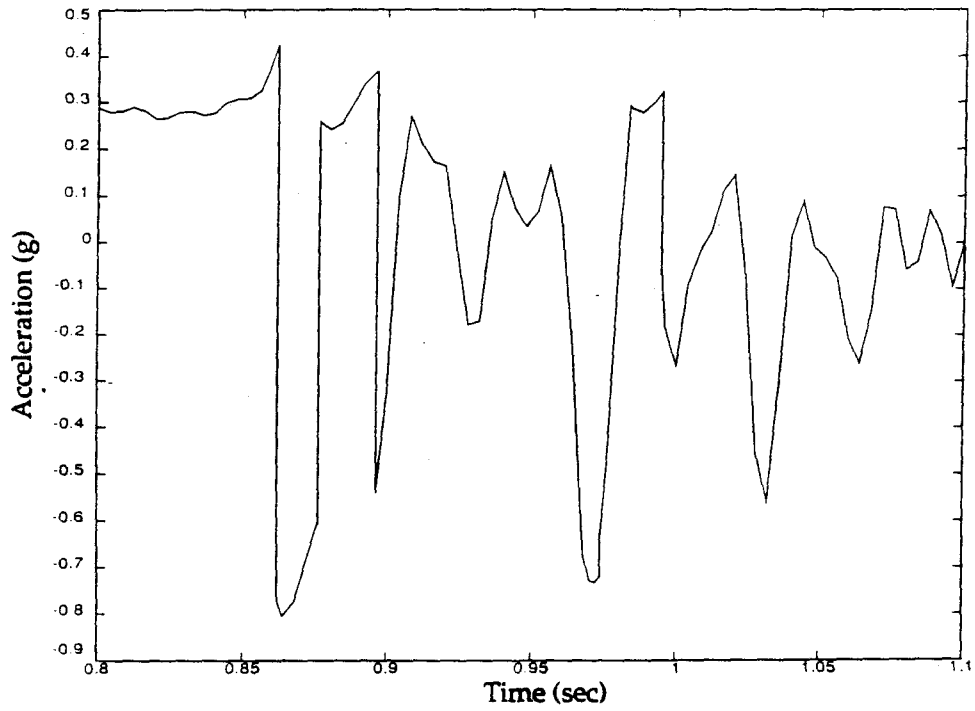

(b)

Figure 3.22 Test G1-E2: (a) record of A_3; and (b) simulated block acceleration.

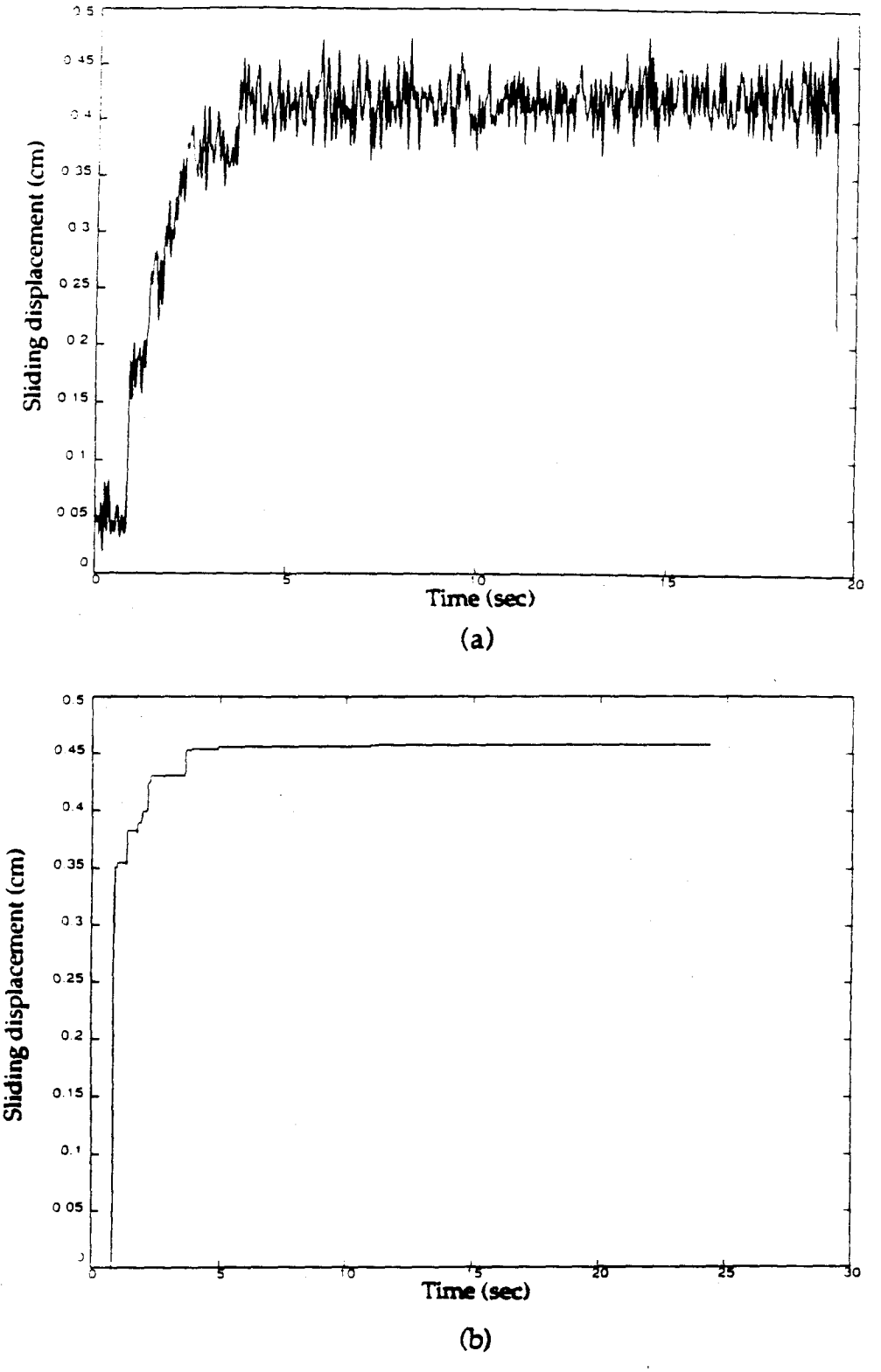

Figure 3.23 Test G1-E2: (a) record of displacement transducer; and (b) simulated sliding displacement.

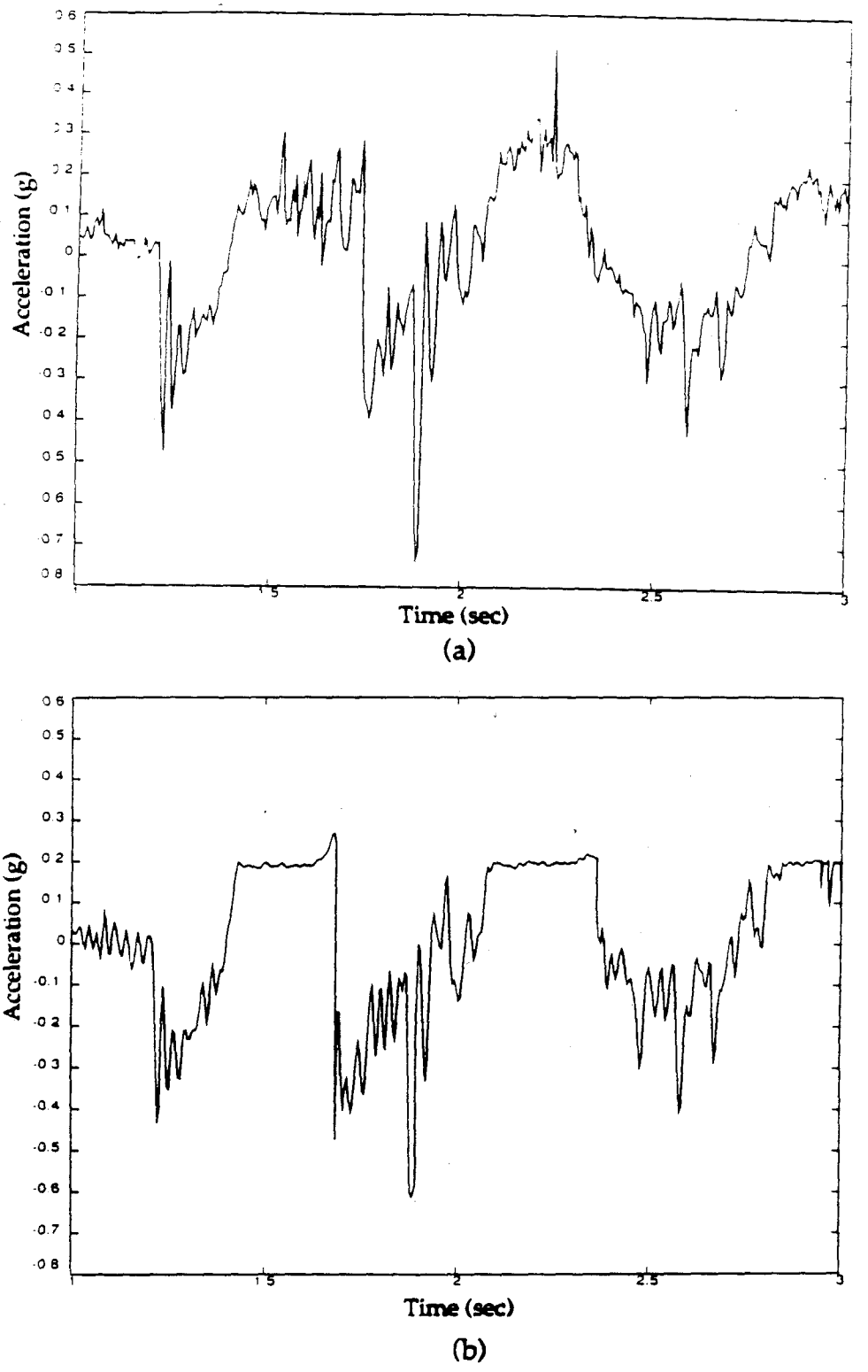

Figure 3.24 Test G1-E3: (a) record of A_3; and (b) simulated block acceleration.

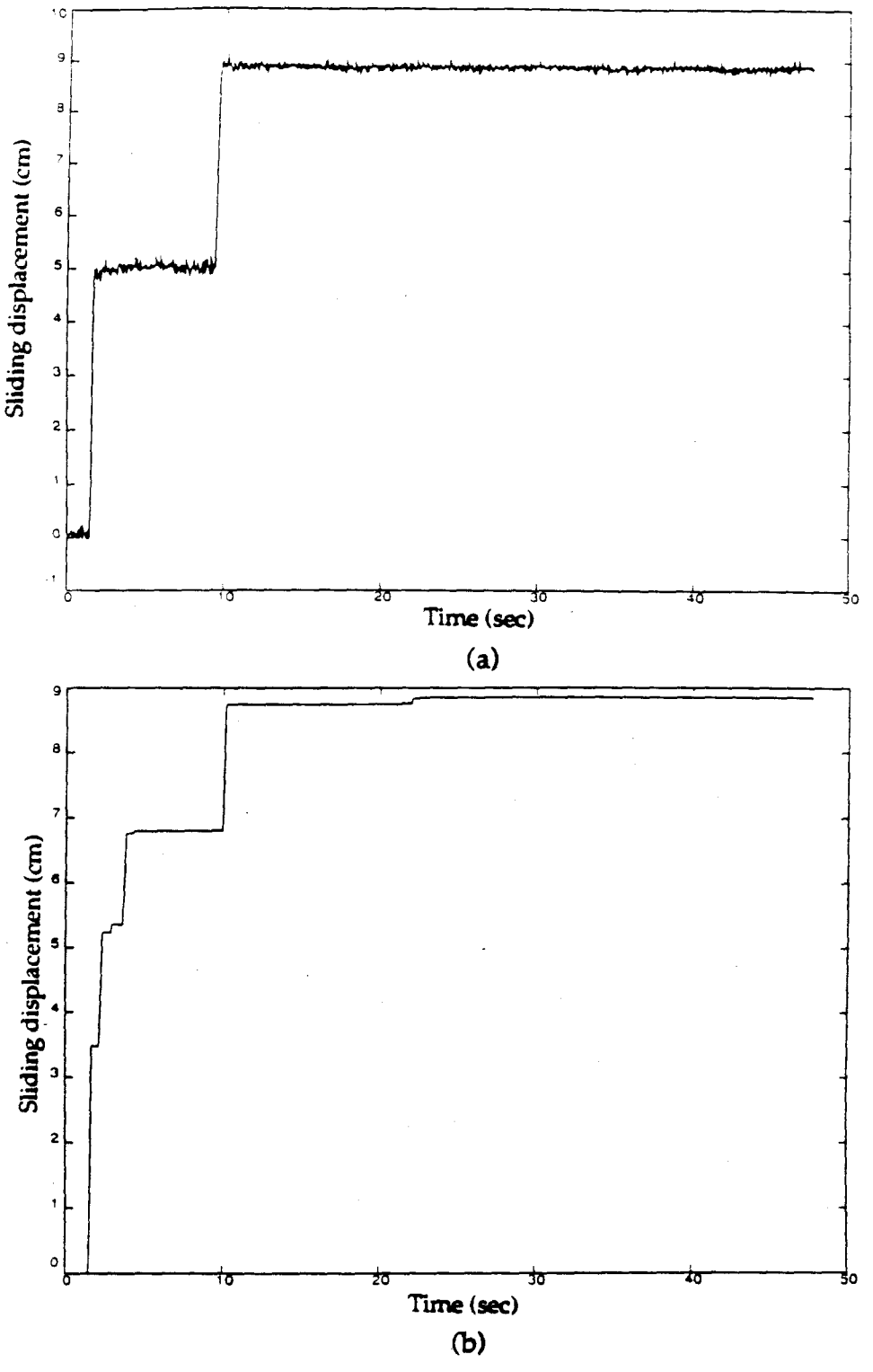

Figure 3.25 Test G1-E3: (a) record of displacement transducer; and (b) simulated sliding displacement.

Chapter 4

ANALYSIS OF LA VILLITA DAM

4.1 Introduction

The objectives of this chapter are to: 1) understand the dynamic characteristics of La Villita Dam in the Mexico earthquake on September 19, 1985, based on the results of the analysis of the recorded accelerograms; 2) perform deformation analysis on La Villita Dam by applying the rigid sliding block model; and 3) evaluate the performance of La Villita Dam and propose an explanation for the unusual phenomena observed in the accelerogram recorded at the crest of the dam.

4.2 La Villita Dam

La Villita Dam is located on the Balsas River in the State of Guerrero, Southern Mexico, 13 km upstream from the mouth of the river, which empties into the Pacific Ocean, and 55 km downstream of El Infiernillo Dam (Figure 4.1). Construction was started in August, 1965 and completed in December, 1967. The dam was built to exploit a large potential for power generation, irrigation and flood control. After the completion of the dam, the power plant had a rated capacity of 304 MW; the storage capacity of the

reservoir was equal to 710×10^6 m^3; and the discharge capacity of the spillway was 13900 m^3/s (Comision Federal de Electricidad, 1976).

The project consists of an earth-and-rockfill embankment, a powerhouse, a spillway, an irrigation outlet and intake works. Figure 4.2 shows a layout. The embankment dam is 60 m high with external slopes of 2.5 : 1, and it is slightly concave toward downstream. The canyon where the dam is built is 300 m wide at the base and 425 m at the crest. The dam has a symmetrical cross-section with a central compacted impervious core, well-graded filters and transition zones and rockfill shells, the latter compacted with four passes of a D-8 tractor. The core was built with a highly plastic clayey material (liquid limit $w_L = 56\%$ and plastic limit $w_P = 24\%$, as an average), which was placed in layers 15-cm thick and compacted with 8 to 10 passes of a sheepsfoot roller, to reach a degree of compaction of 96% with respect to the Standard Proctor Test. For the filters and transitions a sand and gravel material borrowed from alluvial deposits was used, which were protected by rockfill shells. The maximum cross-section of the dam with the different zoned materials is shown in Figure 4.3.

The same figure also shows the geological profile along the dam axis. The dam is founded on a deep alluvial deposit of varying thickness up to a maximum thickness of 70 m which is formed by boulders, gravel, sand and silt. In view of the great thickness of the alluvial deposit, a 0.6-m thick ICOS type concrete cut-off wall was provided down to a depth of 74 m to control water seepage through the alluvium. Moreover, in order to reduce settlement under the core and to provide a second line of defense against breakage of the upper portion of the cut-off wall, a block of alluvium underlying the core was

grouted down to 26 m in depth. A summary of material properties is presented in Table 4.1.

The dam was constructed in two stages. The first was built above water in the dry between stations 0 + 300 and 0 + 490 (Figure 4.4). The second stage began on November 17, 1966 by dumping soil underwater between stations 0 + 150 and 0 + 300. In January 1967, an extraordinary flood eroded the riverbed between these stations and made it necessary to replace the eroded material with fill that was more compressible in this zone (between stations 0 + 150 and 0 + 300) than elsewhere. This inhomogeneous compressibility, the alluvial layer of variable thickness, and the zoned cross section (Figure 4.3) which encourages silo action and localized arching (Casagrande 1950; Sherard 1986), have all probably contributed to the evolution of localized zones of low strength and differential settlements that were further aggravated by seismic shaking as investigated in this study. Detailed information on the dam has been obtained from various references (Comision Federal De Electricidad, 1980, 1985, 1987).

4.3 Instrumentation of La Villita Dam

During construction, a total of 188 instruments and several rows of surface reference points were installed. The instrumentation in the dam was placed along the dam axis and at several planes parallel to the river (refer to Figure 4.5). The instruments include inclinometers, vertical and horizontal extensometers, and accelerographs. The accelerographs are established at five locations. One is on the right bank in sound rock at a distance of 150 m from the embankment, and four are on the downstream slope of the dam. Three

of these are close to the center axis of La Villita Dam: one on the right bank, one on the left bank and one at a station near the crest; and the other one is near the berm at elevation 13.5 m. The readings of the vertical and horizontal movements from the instrumentation furnish information on the deformation history and dynamic responses of the dam since the time of construction, as described later.

4.4 Seismicity of Lower Balsas River Zone

4.4.1 Seismic Activity at the Dam Site

La Villita Dam is located close to the Pacific Ocean coastline and lies within the American continental plate of high seismicity associated with the subduction of the Pacific Plate. From the geological point of view, the formations of the dam site belong to the Tertiary, consisting mainly of extrusive rocks, tuffs and continental alluvial sediments. At the canyon mouth, these Tertiary formations consist of stratified layers of andesite and andesitic breccias, showing a NE-SW strike and pronounced dip towards the SE (refer to Figure 4.3). The strata, varying in thickness from a few centimeters to several meters, are affected by intense fracturing with a NE-SW general direction and a dip towards the NW. The alluvial deposit at the river bottom reaches a thickness of 70 m and it is formed by boulders, gravel, sand and silt. The whole region has been subjected to a strong tectonism and it constitutes one of the most active seismic areas in Mexico.

4.4.2 Earthquake History and Deformation of La Villita Dam

The dam has experienced many earthquakes. Table 4.2 lists the strongest seismic events that occurred within 100 km of the dam between 1975 and 1985. It is worth noting the variation of the seismic activity from 1975 to 1985. The increases of activity in the years 1979, 1981 and 1985 are very prominent. The most important earthquakes in the area took place on October 11, 1975, November 15, 1975, March 14, 1979, October 25, 1981, September 19, 1985 and September 21, 1985. These six earthquakes are identified by the symbols S_1, S_2, S_3, S_4, S_5 and S_6. Their parameters are summarized in Table 4.3.

Settlement and horizontal deformations have occurred over the years in the upstream and downstream shells, as well as in the central clay core (see Comision Federal de Electricidad, 1980, 1985, 1987 for a comprehensive description). Attention in this section will be focused on the downstream slope. The settlement history of the dam is shown in Figure 4.6. Horizontal displacements are shown in Figure 4.7.

The discussion here concentrates on the event S_5. A detailed study of the records of other earthquakes and corresponding yielding accelerations has been presented in the reference (Elgamal et al., 1990).

4.5 Earthquake of September 19, 1985

The earthquake of September 19, 1985 was one of the most destructive in this century in Mexico in terms of damage to structures (EEFIT, 1986). It had magnitude 8.1 on the Richter scale. The epicenter was located at latitude 18.108°N and longitude 102.707°W. The focal depth was 30 km. At Mexico

City, which is about 400 km ENE of the epicenter, the earthquake caused a large amount of damage in the central city area primarily to modern structures between 6 and 20 stores high, which was attributed to the amplification of the ground excitations due to the resonance of the old lake bed on which Mexico City lies. Over 200 buildings collapsed, thousands were damaged and an estimated 5 to 20 thousand people were killed, mainly by being crushed or entombed in collapsed structures.

4.5.1 Effects on the Dam

The distance from La Villita Dam to the epicenter is 58 km. The dam was severely shaken by the earthquake. The instruments recorded the settlements and horizontal displacements induced by the excitation, which showed that the maximum settlement was more than 30 cm occurring along with lateral translation of about 14 cm (Figures 4.6 and 4.7). Longitudinal cracks also appeared along the crest as shown in Figure 4.8. In addition, offset on the crest and bulging near the toe on the downstream were observed.

4.5.2 Earthquake Records

Unfortunately, not all the accelerographs worked properly. Only the accelerographs at the dam crest and on the right bank recorded the accelerograms during the earthquake. Each record consists of three components, which are shown in Figures 4.9 and 4.10. The unit of acceleration used here is the gal (980 gals = 9.8 m/sec/sec = 1 g). In all of these records, it is quite conspicuous that the strong shaking occurs in two episodes. In the transverse component of the acceleration recorded at the crest of the

dam (Figure 4.10(b)), by comparison with other components, the accelerogram appears to be abnormal, since the positive part of the accelerogram has much higher peak accelerations than does the negative part. Also the peaks in the positive part are very sharp spikes (see Figure 4.11, which is a stretched piece of Figure 4.10(b)). The similar abnormal phenomenon appears on the vertical component too (Figure 4.10(c)), although it is not as pronounced as on the transverse component.

The Fourier amplitude spectra of all the recorded accelerations are obtained by utilizing a Fast Fourier Transform algorithm (Hall, 1982). Figures 4.12 and 4.13 show the Fourier amplitude spectra of the transverse accelerations recorded at the right bank and on the dam crest in the earthquake of September 19, 1985. The Fourier amplification spectrum for the transverse component, computed by dividing the Fourier amplitude spectrum from the dam crest by that from the right bank is shown in Figure 4.14. The high peaks in the amplification spectrum are spurious and result from chance values near zero in the amplitude spectrum from the right bank, i.e., in the denominator for the amplification spectrum computation. However, the lower but wider peak centered at about 1.25 Hz in Figure 4.14 is real and indicates that this frequency is the fundamental frequency of response in the dam vibration.

4.6 Analysis of Deformations

The deformations which have occurred at La Villita Dam could have resulted from settlement by densification. It is also possible that slip planes have developed inside the dam, and that some portion of the deformation

can be attributed to sliding on these slip planes. Evidence which suggests the possibility of sliding includes the bulging near the toe on the downstream side and the asymmetrical acceleration record obtained near the crest on the downstream side. Recall from Chapters 2 and 3 that accelerations of a sliding mass can show similar asymmetry.

It is of interest to determine whether a slip plane, with a reasonable choice of parameters, can produce the observed deformation which occurred during the September earthquake and if the asymmetric accelerations can be reproduced. This investigation is restricted to the downstream side of the dam and will focus on the maximum resultant displacement of 22.5 cm (5.7 cm horizontal, 21.8 cm vertical) measured near the crest, all of which will be assumed to have been a result of sliding. The transverse acceleration will be assumed to be positive in the downstream direction (toward downslope) and the vertical acceleration to be positive upward. This choice for the transverse component is consistent with the asymmetry in the transverse acceleration record being caused by a sliding mechanism, while positive upward is conventional for the vertical component.

The analysis is hampered by the lack of an appropriate base excitation for the sliding mass. In the absence of anything better, the transverse and vertical components recorded at the right bank were scaled up in amplitude by a factor of 6.385 for the transverse and 5.166 for the vertical. The resulting transverse excitation component has the same peak acceleration as the transverse component recorded on the dam crest (772 gals), although this peak is negative for one and positive for the other. Also the resulting vertical

excitation component has the same peak acceleration as the vertical component recorded on the dam crest (297 gals).

4.6.1 Inclined Plane Slip Surface Assumed

First the sliding surface is assumed to be an inclined plane, passing through the downstream toe of the dam. Computations are carried out with the computer program *NAN-P*.

When the inclined angle θ is constant (18^o), the variation of permanent displacement with internal friction angle ϕ is shown in Table 4.5. It can be seen that the dam material property greatly affects the downslope displacements.

Keeping the value of the soil's internal friction angle ϕ constant (at the value of 34.4^o) and letting the slip plane have various inclined plane angles θ, the corresponding displacements have been calculated and are summarized in Table 4.6. It is very apparent that the displacement increases very rapidly with increasing of the slip plane angle. The angle $\theta = 22^o$ is the angle of the slope of the dam faces.

Figures 4.15 shows the time histories of sliding acceleration, sliding velocity, absolute horizontal acceleration and sliding displacement of the block for the case $\phi = 34.4^o$ and $\theta = 22^o$. For these parameters, the computed displacement of 22.6 cm matches the measured one. However, the components of the computed displacement (i.e., settlements and transverse or horizontal displacements) are not in agreement. It is also of interest that almost all the displacement developed in the first interval of strong motion.

The computed absolute horizontal acceleration of the sliding mass (Figure 4.15 (c)) does exhibit some asymmetry in the initial part of the record, which is in the correct direction as expected, but some of the sharpest spikes of the recorded horizontal acceleration at the crest (Figure 4.10(b) and Figure 4.11) are not reproduced.

4.6.2 Circular Arc Slip Surface Assumed

Now a circular slip surface is assumed with an angle β at the crest chosen so that the direction of the computed displacement of the sliding mass at the crest matches the measured one. Figure 4.16(a) shows Circular arc 1, which is a part of a circle with a radius R = 80.4 m; also R_c = 61.14 m and R_i = 31.0 m. The slip surface goes through the dam crest at point 1 and is tangent to the baseline at point 2. The slope of this circular slip surface where it emerges at the crest of the dam is β (= 14.7^o) with respect to vertical; also $\theta_o = 21.8^o$.

Figure 4.17 shows the computed time histories for sliding acceleration, sliding velocity, sliding displacement, absolute horizontal acceleration and absolute vertical acceleration. All computed motions are at the crest, and the sliding motions are tangential to the slip surface. The match in crest displacement was obtained with $\phi = 25.0^o$, a fairly low value for the friction angle. With $\beta = 14.7^o$, the computed components of crest displacement (5.7 cm horizontal and 21.8 cm vertical) also match the measured ones.

The absolute horizontal acceleration of the sliding mass at the crest (Figure 4.17(d)) does not exhibit the desired asymmetry and, in fact, is almost identical to the horizontal component of the input excitation (Figure 4.9 (b)

scaled by 6.385). The reason for this is that the steep slope of the sliding surface at the crest ($\beta = 14.7^{o}$) gives a very small horizontal component to the sliding motions. It is the vertical acceleration (Figure 4.17(e)) which is affected most, and the most pronounced feature is a large positive spike associated with the largest sliding episode. This spike is in the wrong direction to correlate to the slight asymmetry in the recorded vertical acceleration (Figure 4.10(c)).

Another slip surface, Circular arc 2 as shown in Figure 4.16(b), is used to try a geometry intermediate between the previous inclined plane and Circular arc 1. The circle goes through the dam crest at point 1 and the dam toe at point 2. Also the circle makes a tangent with the baseline at point 2. The geometric parameters are: R = 217.5 m, R_c = 208.2 m, R_i = 36.5 m; $\beta = 46.4^{o}$ and $\theta_o = 21.8^{o}$.

Table 4.7 shows the relationship between sliding displacement at the dam crest and the value used for the internal friction angle ϕ of the dam. When the friction angle is 32.45^{o}, a more realistic value of friction angle, the computed sliding displacement (22.50 cm) is close to the measured resultant displacement (22.53 cm), although now the components do not match. Figure 4.18 shows computed time histories for sliding acceleration, sliding velocity, sliding displacement, absolute horizontal acceleration and absolute vertical acceleration. All computed motions are at the crest, and the sliding motions are tangential to the slip surface. The absolute horizontal acceleration with its asymmetry in the initial part (Figure 4.18(d)) is similar to that obtained for the sliding mass on the inclined plane (Figure 4.15(c)), and the absolute vertical acceleration (Figure 4.18(e)) is not much different from that obtained for the sliding mass on Circular arc 1 (Figure 4.17(e)). Thus, the use of Circular arc 2

shows a somewhat better agreement with the recorded accelerations. Finally, Figure 4.19 shows the computed absolute horizontal acceleration from Figure 4.18(d) with an expanded time scale. The positive asymmetric acceleration peaks between 7 seconds and 12 seconds lack the sharpness of the peaks in the recorded accelerations shown in Figure 4.11 with a similarly expanded time scale. This occurs in part because the peaks in the positive side of the calculated result are, in fact, exactly those from the amplified abutment input. There is nothing in the analysis (elastic behavior, for example) which can cause any change in the positive accelerations. However, on the expanded time scale of Figure 4.11, the positive peaks do appear to be unusual in character as compared to those observed in other strong motion records.

4.7 Summary

From the analysis of the recorded accelerograms, it is found that the fundamental frequency of La Villita Dam seems to be about 1.25 Hz. The frequency content of the bedrock motions in the vicinity of La Villita Dam in the Mexico earthquake on September 19, 1985 is rich in the range of this fundamental frequency of vibration of the dam.

The attempt to reproduce features of the motions recorded at La Villita Dam during the September 1985 earthquake through sliding block analysis was partially successful. The analysis with the inclined plane sloping at $\theta = 22^{o}$ and the moderately deep Circular arc 2 reproduce the 22.5 cm crest resultant displacement for friction angles ϕ of 34.7^{o} and 32.5^{o}, respectively, when a base excitation with peak horizontal acceleration of 772 gals is used. These friction angles are in the typical range for the granular material of the

dam. For the deeper Circular arc 1 (the only slip surface which could match the direction of crest displacement), ϕ has to be reduced to 25^{o}, a relatively low value. Absolute horizontal accelerations from the inclined plane and Circular arc 2 analysis show some asymmetry in the accelerations, but the number and sharpness of the positive spikes in the measured horizontal accelerations are not reproduced. The horizontal acceleration from the Circular arc 1 analysis and vertical accelerations from all three analyses do not correlate with the measured records.

The lack of better agreement between analysis results and the observations could be due to 3-dimensional action, inadequacy of the scaled right bank record as appropriate input, and the role of other deformation mechanisms such as settlement by densification, the observed cracking and possible slumping near the crest. Other possible explanations for the asymmetric spikes in the recorded crest accelerations include the repeated closing of an undetected vertical crack in the dam near the accelerograph, rolling debris colliding with the accelerograph, slipping of the hut in which the accelerograph was located, or accelerograph malfunction. Alfaro and Lopez investigated the slipping of the hut and got very little movement of the hut; but the results were inconclusive (Alfaro and Lopez, 1986).

In spite of the above, the numerical analysis with the rigid sliding block model indicates that permanent localized deformations related to the formation of the slip surfaces in both upstream and downstream slopes of the dam are possible during strong earthquake motions. Thus, the observed permanent deformations on both slopes of La Villita warrant a careful evaluation of its current condition and its susceptibility to future seismically-

induced deformations. The apparent condition of the dam in any case necessitates additional monitoring instrumentation and close surveillance. Also it would be desirable to perform a more detailed deformation analysis using elasto-plastic finite element or finite element computer codes, which might more realistically represent the real dam movements.

	UU shear strength (t/m^2)	Effective friction angle (degree)	Unit weight: dry (t/m^3)	Unit weight: saturated (t/m^3)
clay core	7.0	0.0	1.55	2.0
filter and transitions	--	35.0	2.1	2.18
compacted rockfill	--	45.0	2.0	2.08
foundation alluvium	--	35.0		2.08
grouted alluvium	--	--		2.2
concrete cut-off	--	--		2.3

Table 4.1 Material properties of La Villita Dam

Year	Richter magnitude				Number of annual event
	$M_S<3$	$3\leq M_S<4$	$4\leq M_S<5$	$M_S\geq 5$	
1975	1	1	4	3	9
1976	0	6	26	5	37
1977	0	10	28	9	47
1978	3	8	21	9	41
1979	0	14	77	13	104
1980	1	28	21	2	52
1981	21	84	36	3	144
1982	2	55	9	0	66
1983	0	21	5	1	27
1984	1	25	2	0	28
1985	79	291	28	4	402
Total	108	543	257	49	957

Table 4.2 Earthquakes within 100 km of La Villita Dam.

Seismic event	Date	M_s	Duration (sec)	Focal depth (km)	Epicentral distance (km)	Maximum acceleration (gals) recorded at	
						bedrock	crest
S_1	Oct. 11, 75	4.9	14.1	33	52	73	348
S_2	Nov. 15, 75	5.9	19.5	33	10	41	204
S_3	Mar. 14, 79	7.6	31.3	60	121	–	389
S_4	Oct. 25, 81	7.3	71.6	33	31	85	421
S_5	Sep. 19, 85	8.1	76.1	30	58	118	772
S_6	Sep. 21, 85	7.5	63.9	33	61	41	210

Table 4.3 Parameters of major earthquakes that have occurred in the vicinity of La Villita Dam.

	Upstream	Crest	Downstream
Settlement (cm)	31.80	12.00	21.80
Transverse disp. (cm)	13.50	–	5.70
Resultant disp. (cm)	34.55	–	22.53

Table 4.4 Deformation recorded at La Villita Dam's crest during the earthquake of September 19, 1985.

ϕ (degree)	25	30	35	40
Displacement (cm)	75.75	23.41	9.13	4.37

Table 4.5 Inclined plane assumed: displacement vs. friction angle ($\theta = 18^o$).

θ (degree)	18	20	22	24
Displacement (cm)	10.18	15.01	22.60	34.71

Table 4.6 Inclined plane assumed: displacement vs. inclined angle ($\phi = 34.4^o$).

ϕ (degree)	31.50	32.00	32.45	33.00	34.00
Displacement (cm)	27.41	24.68	22.50	20.16	16.63
$R = 217.5$ m, $R_c = 208.2$ m, $R_i = 36.5$ m; $\theta_o = 21.8^o$, $\beta = 46.4^o$					

Table 4.7 Circular arc 2 assumed: displacement vs. friction angle.

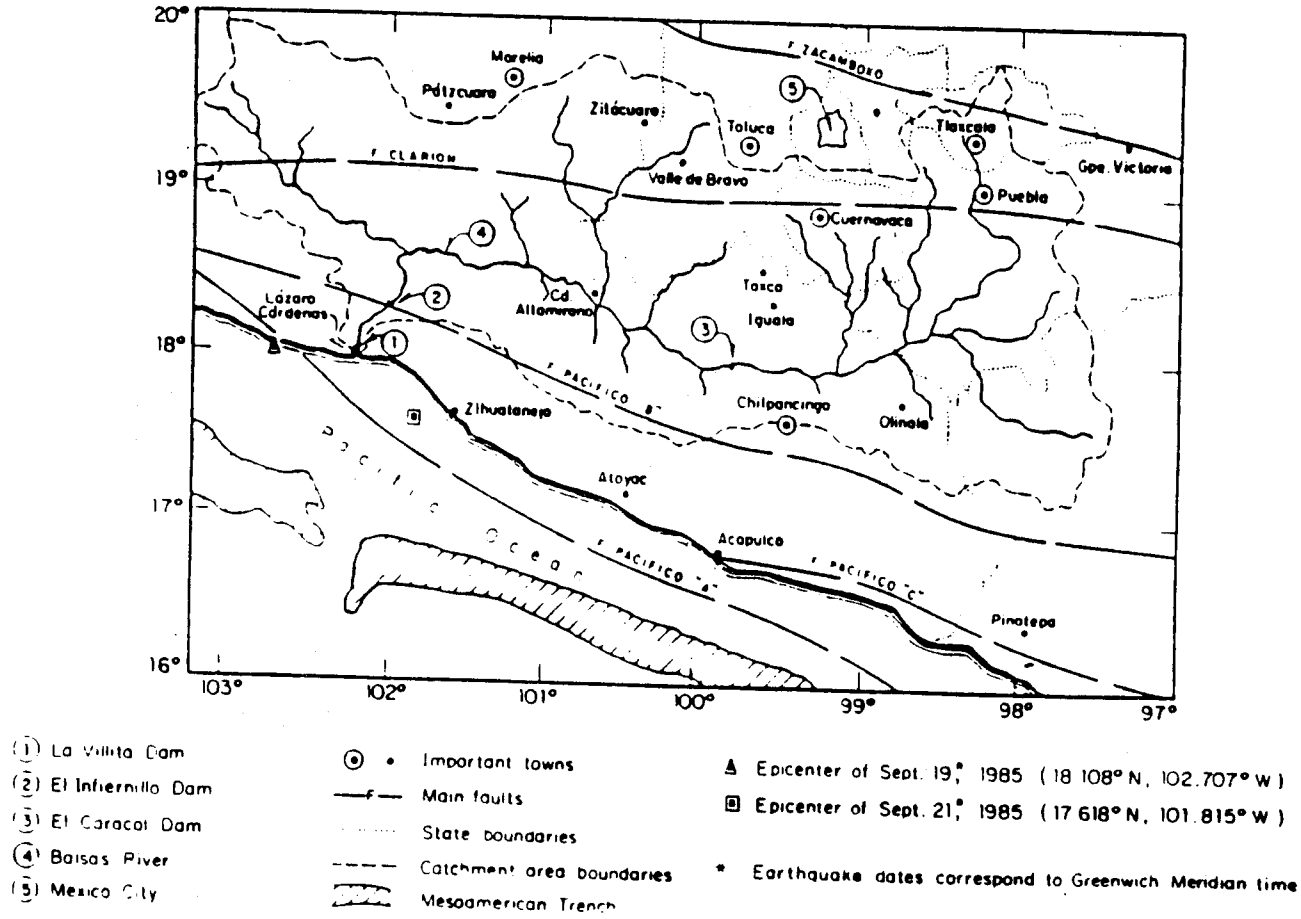

Figure 4.1 Location of dams and epicenters of the September 1985 earthquakes.

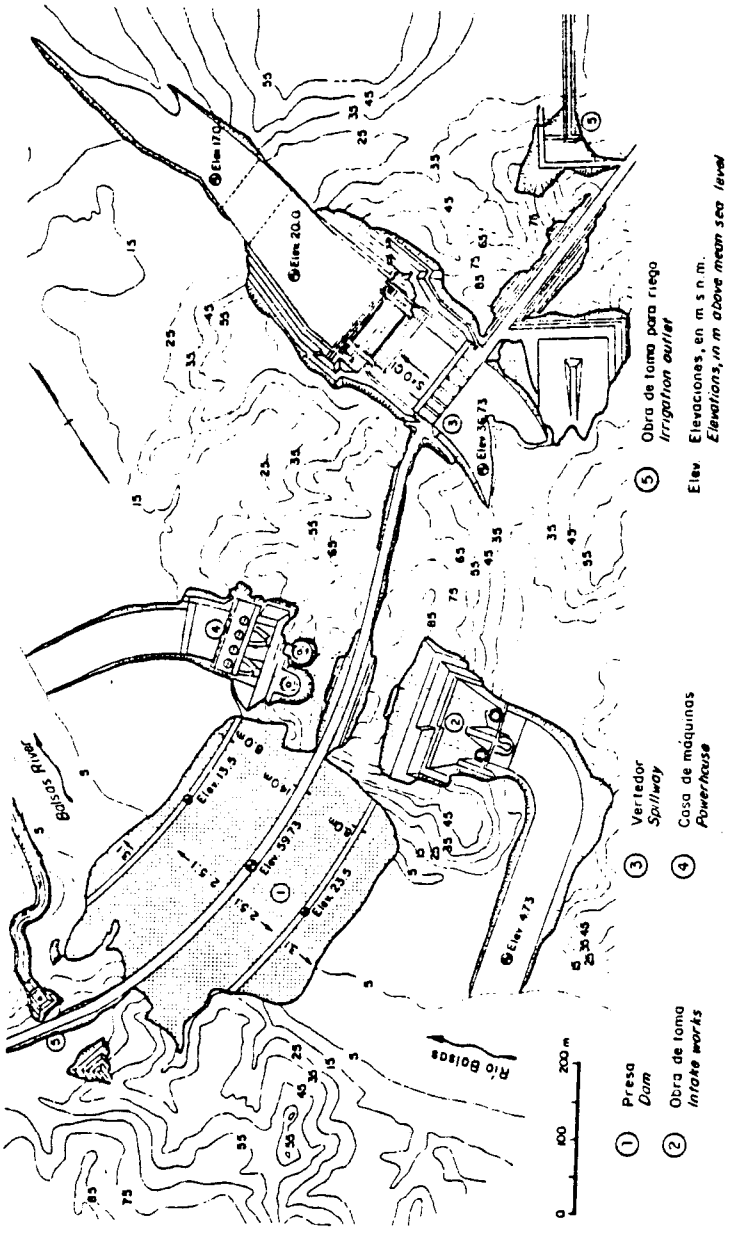

Figure 4.2 La Villita Dam: General layout.

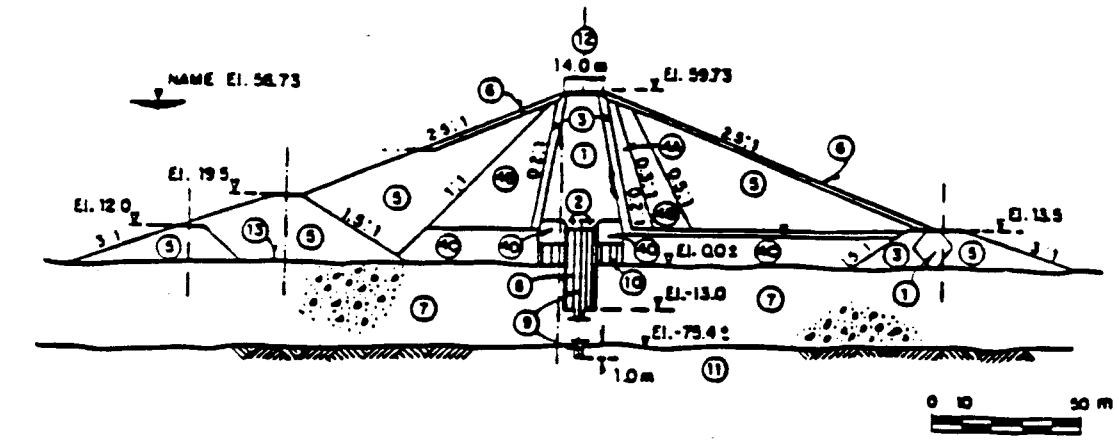

(1) Compacted impervious material
(2) Highly plastic clay
(3) Sand filters
(4A) Well graded gravel and sand
(4B) Gravel and sand
(4C) Dumped gravel and sand
(4D) Compacted gravel, sand and muck
(5) Rockfill
(6) Selected rockfill
(7) Alluvium (gravel and sand)
(8) Grout curtain
(9) ICOS-type concrete cut-off wall
(10) Consolidation grouting
(11) Andesitic breccia
(12) Dam axis
(13) Original ground surface
El. Elevation, in meters
NAME Maximum water level

(a)

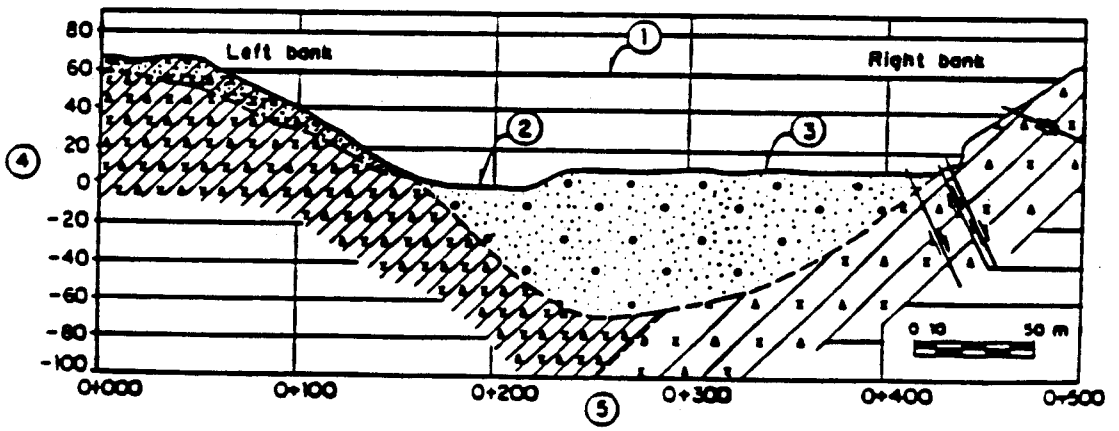

Thinly bedded pseudo-stratified andesitic breccia
Pseudo-stratified andesitic breccia
Highly weathered zone
Alluvium
Fault
(1) Dam crest
(2) Balsas River-main channel
(3) Original ground surface
(4) Elevation, in meters
(5) Stations, in meters

(b)

Figure 4.3 La Villita Dam: (a) maximum cross section; and (b) geological profile.

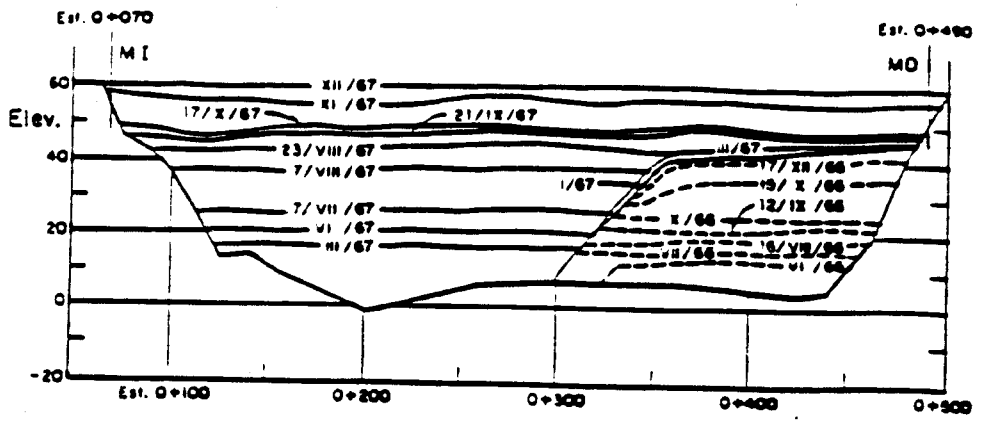

Figure 4.4 La Villita Dam: stages of construction.

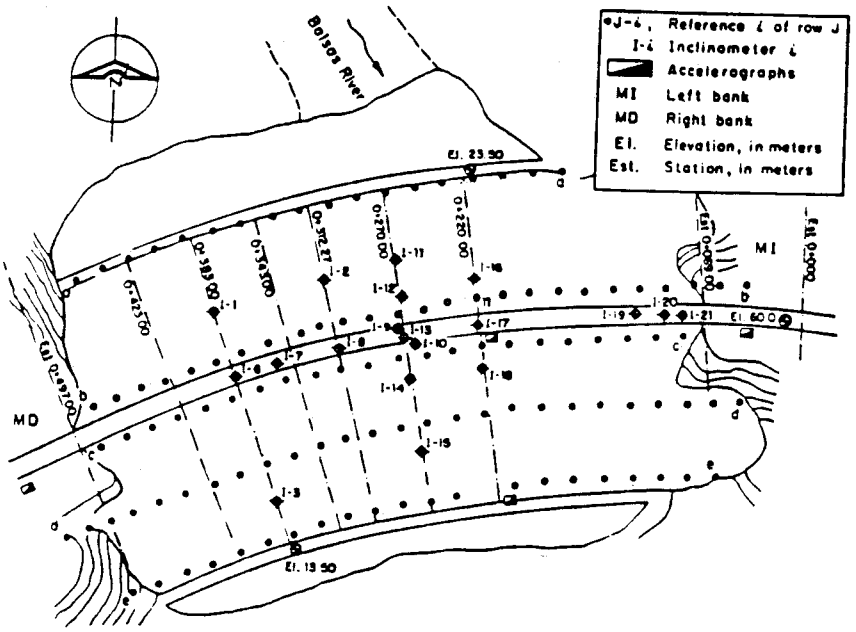

Figure 4.5 La Villita Dam: location of instrumentation.

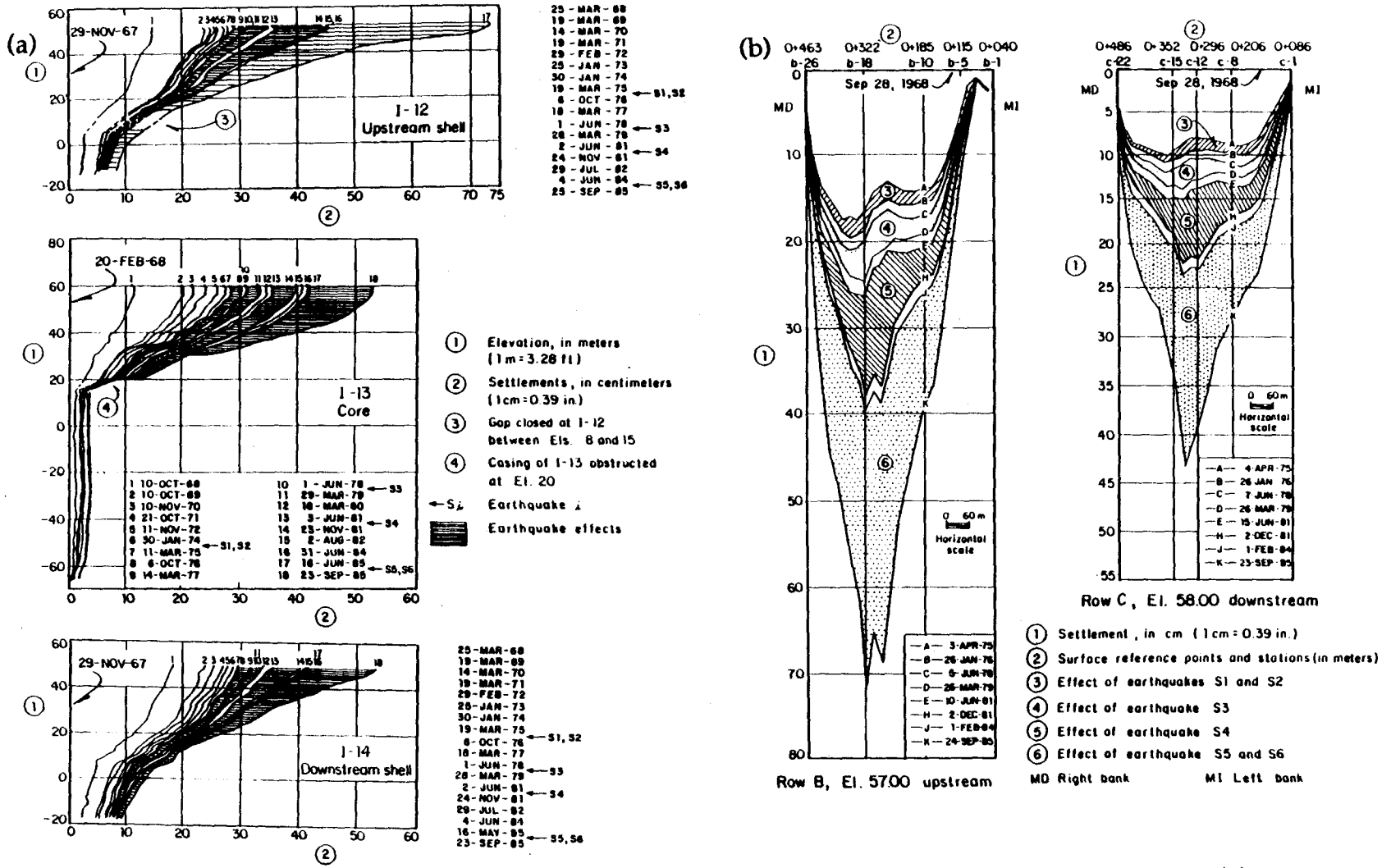

Figure 4.6 Permanent settlement history of La Villita Dam: (a) settlement sampled at Reference Points I-12, I-13 and I-14; and (b) settlement along Rows B and C.

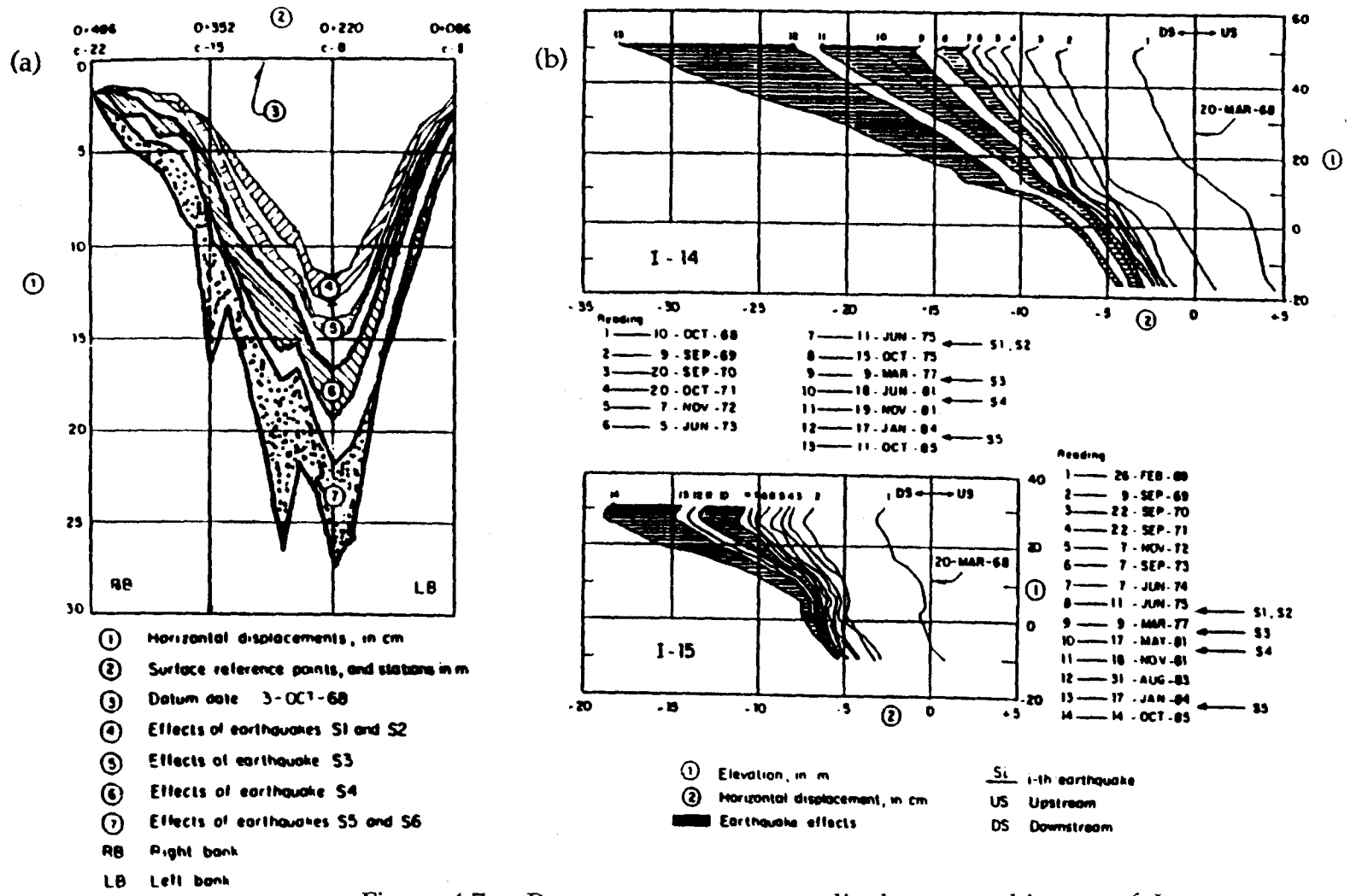

Figure 4.7 Permanent transverse displacement history of La Villita Dam: (a) displacement along Row C; and (b) displacement sampled at Reference Points I-14 and I-15.

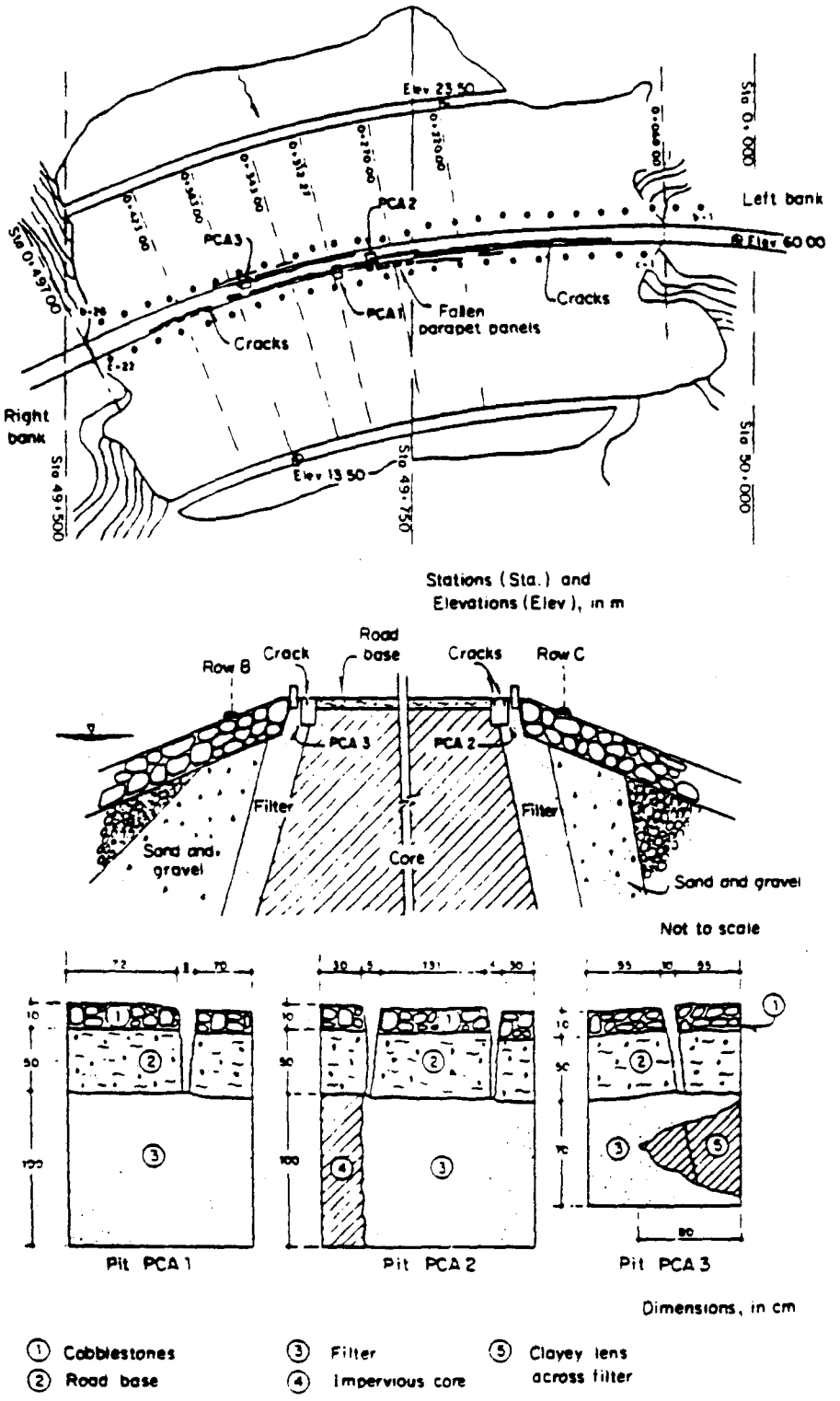

Figure 4.8 Cracks produced by the earthquake of September 19, 1985, at La Villita Dam.

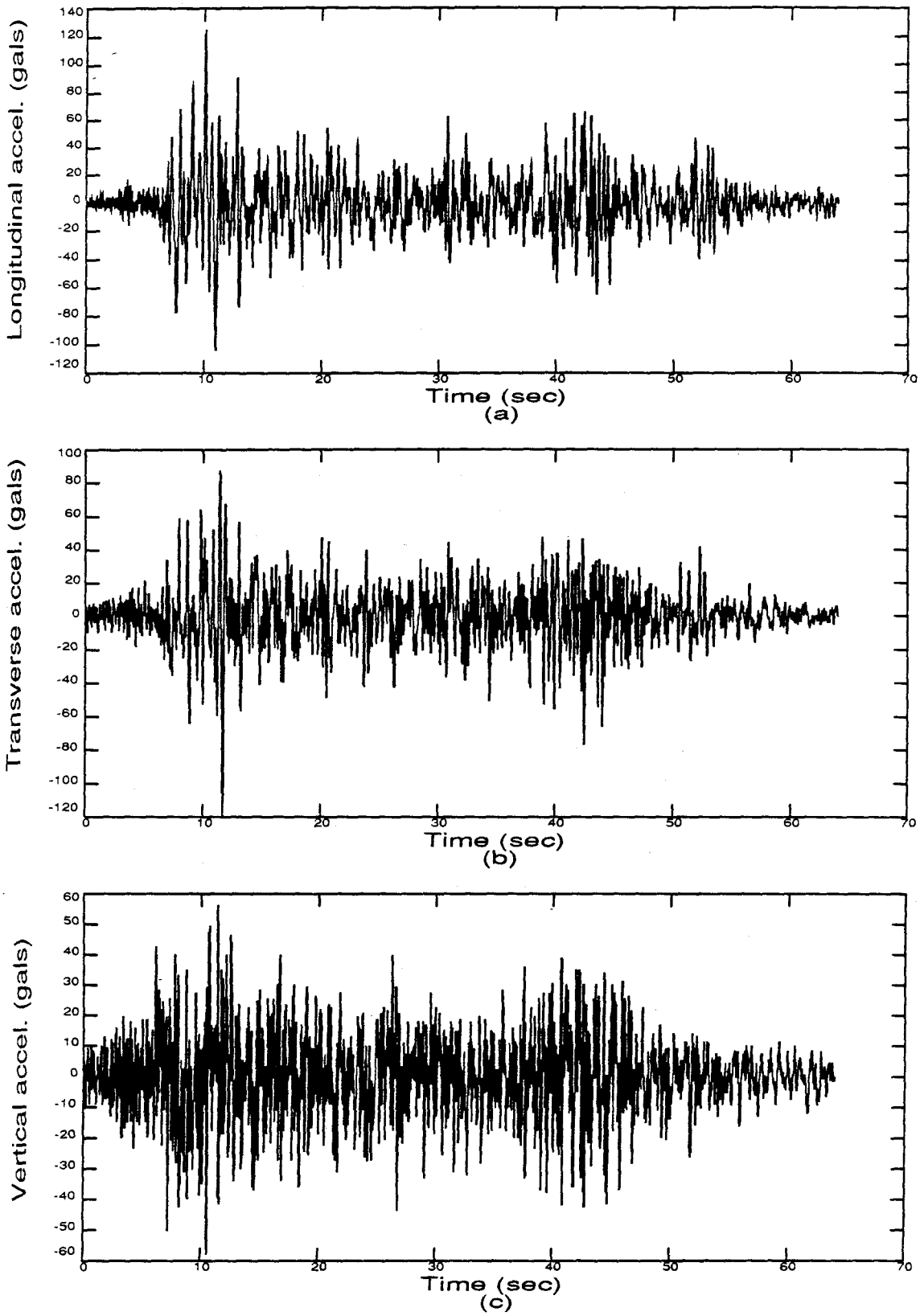

Figure 4.9 Earthquake of Sep.19, 1985: accelerograms recorded at La Villita Dam's right bank.

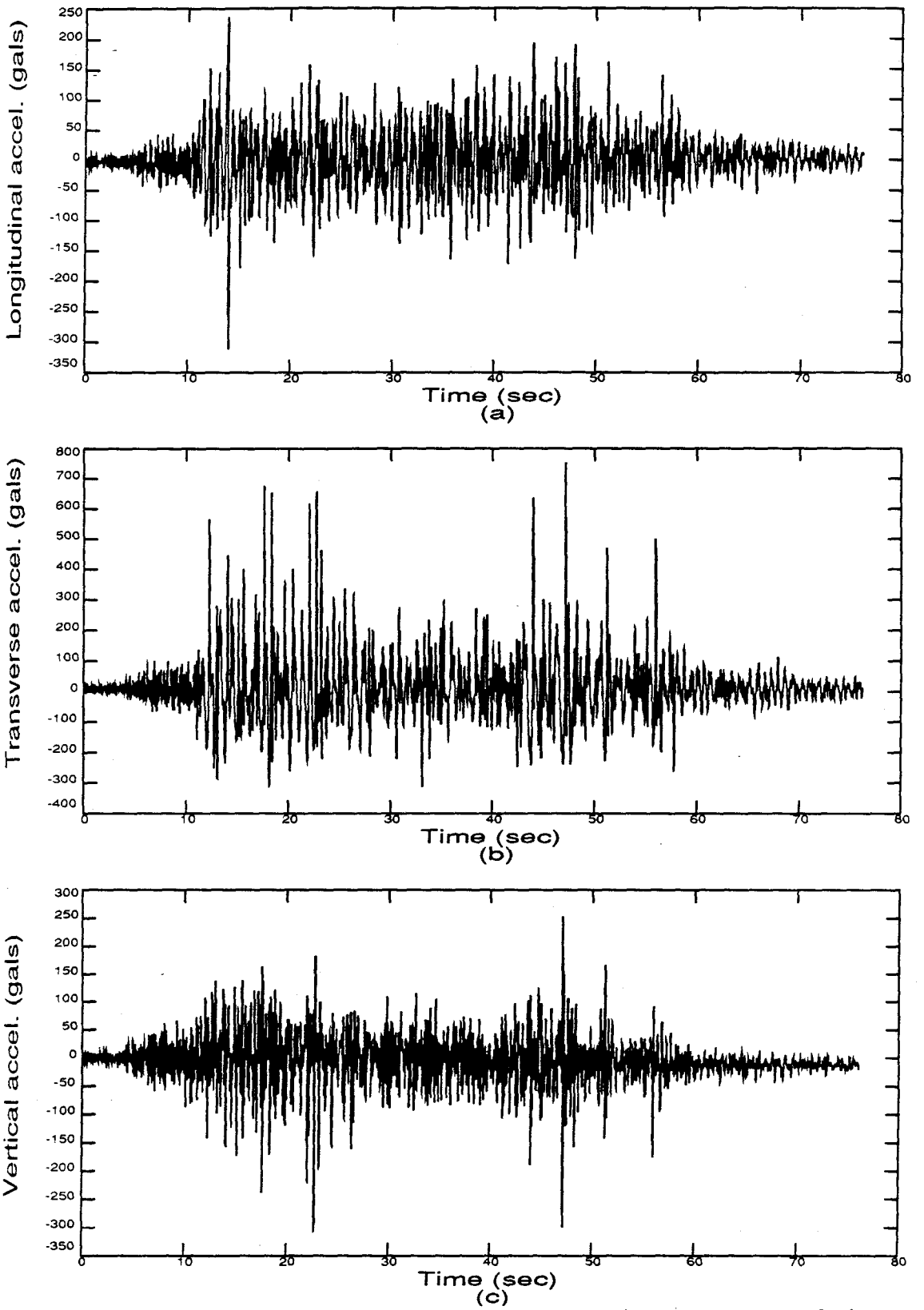

Figure 4.10 Earthquake of Sep.19, 1985: accelerograms recorded at La Villita Dam's crest.

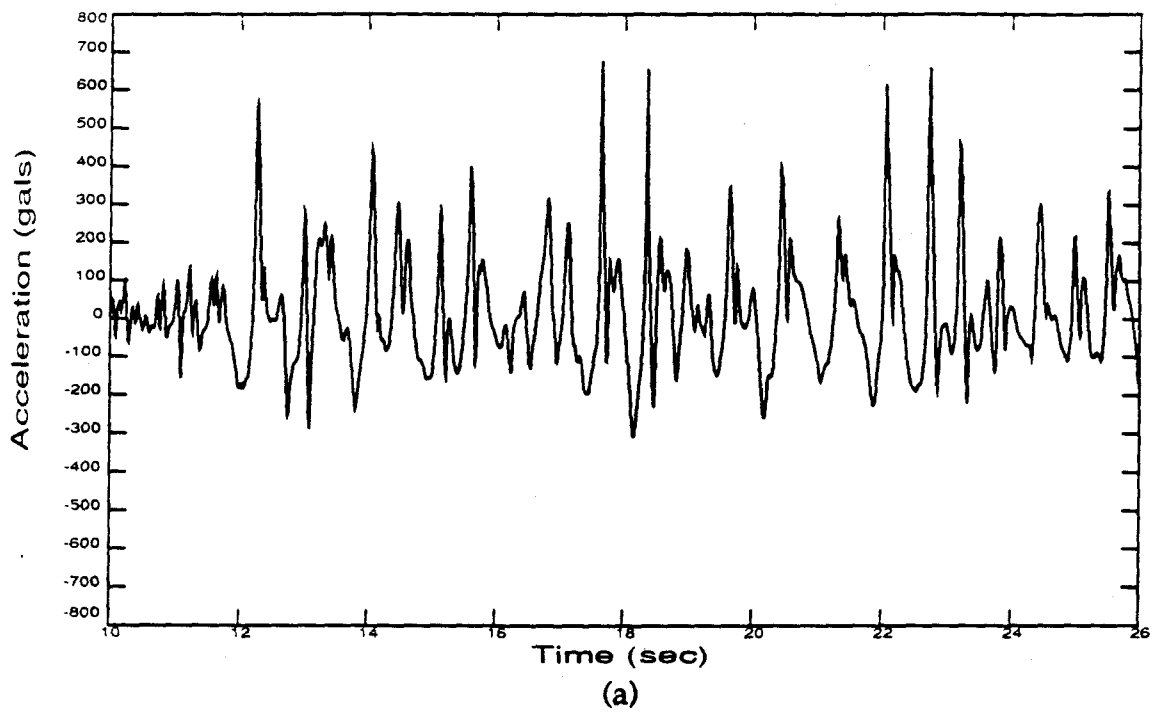

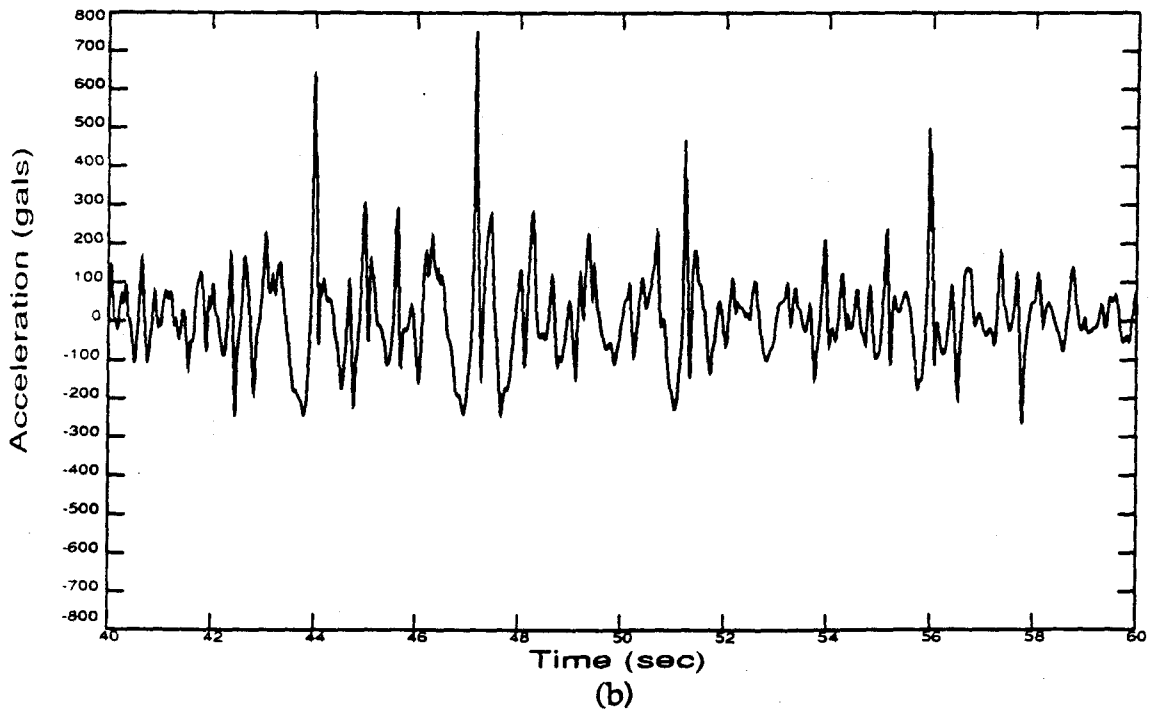

Figure 4.11 Earthquake of Sep.19, 1985: expanded plot of transverse accelerogram recorded at La Villita Dam's crest.

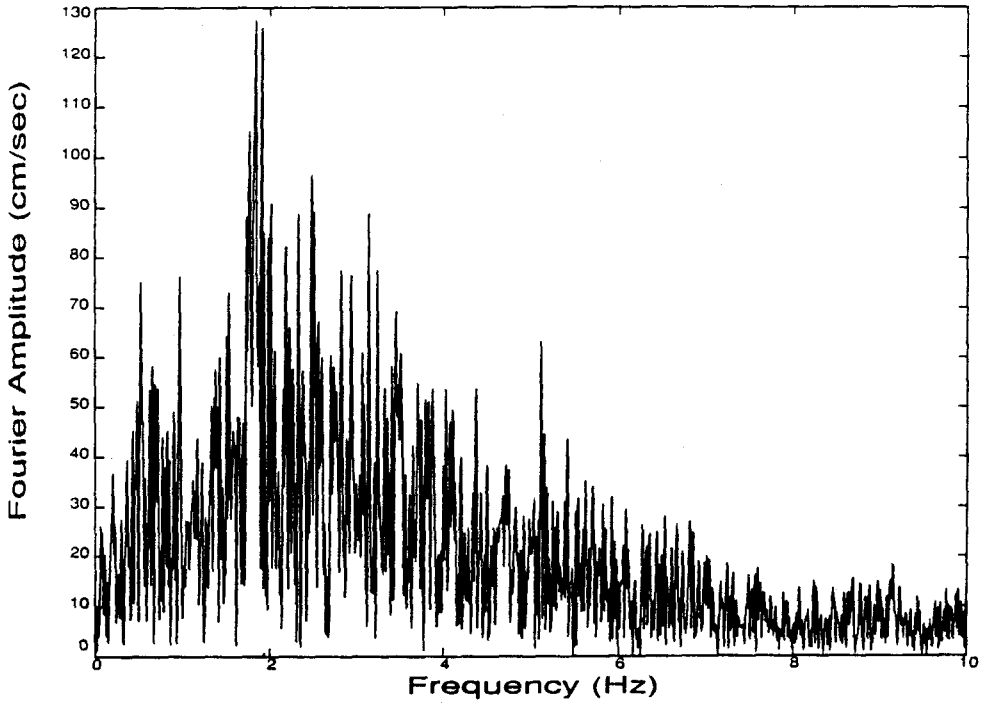

Figure 4.12 The Fourier amplitude spectrum of the transverse acceleration recorded at La Villita Dam's right bank.

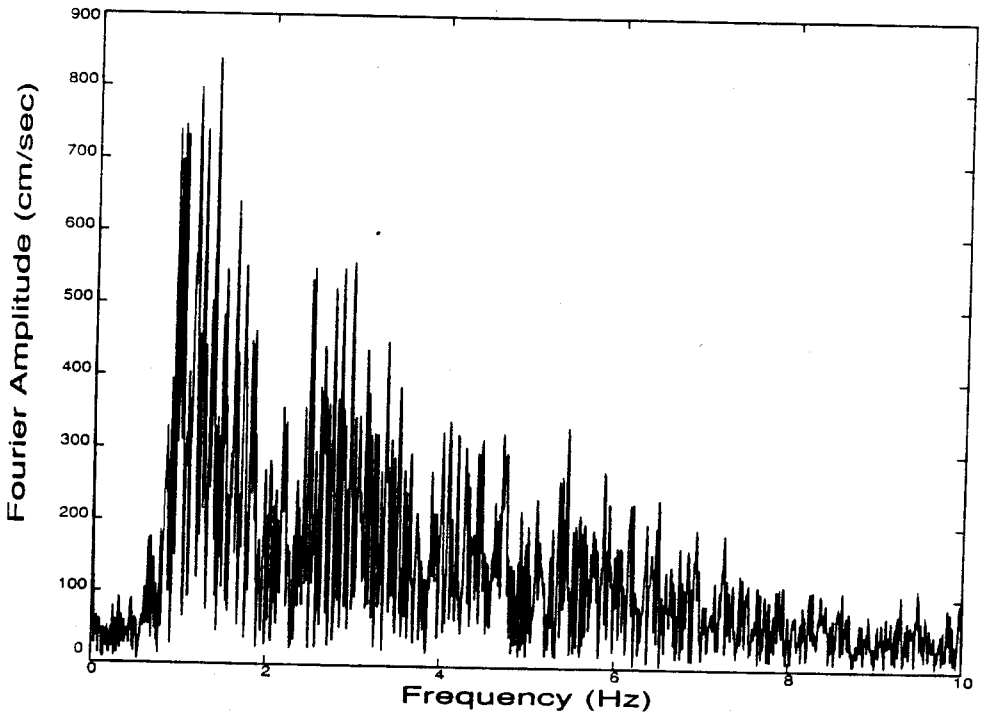

Figure 4.13 The Fourier amplitude spectrum of the transverse acceleration recorded at La Villita Dam's crest.

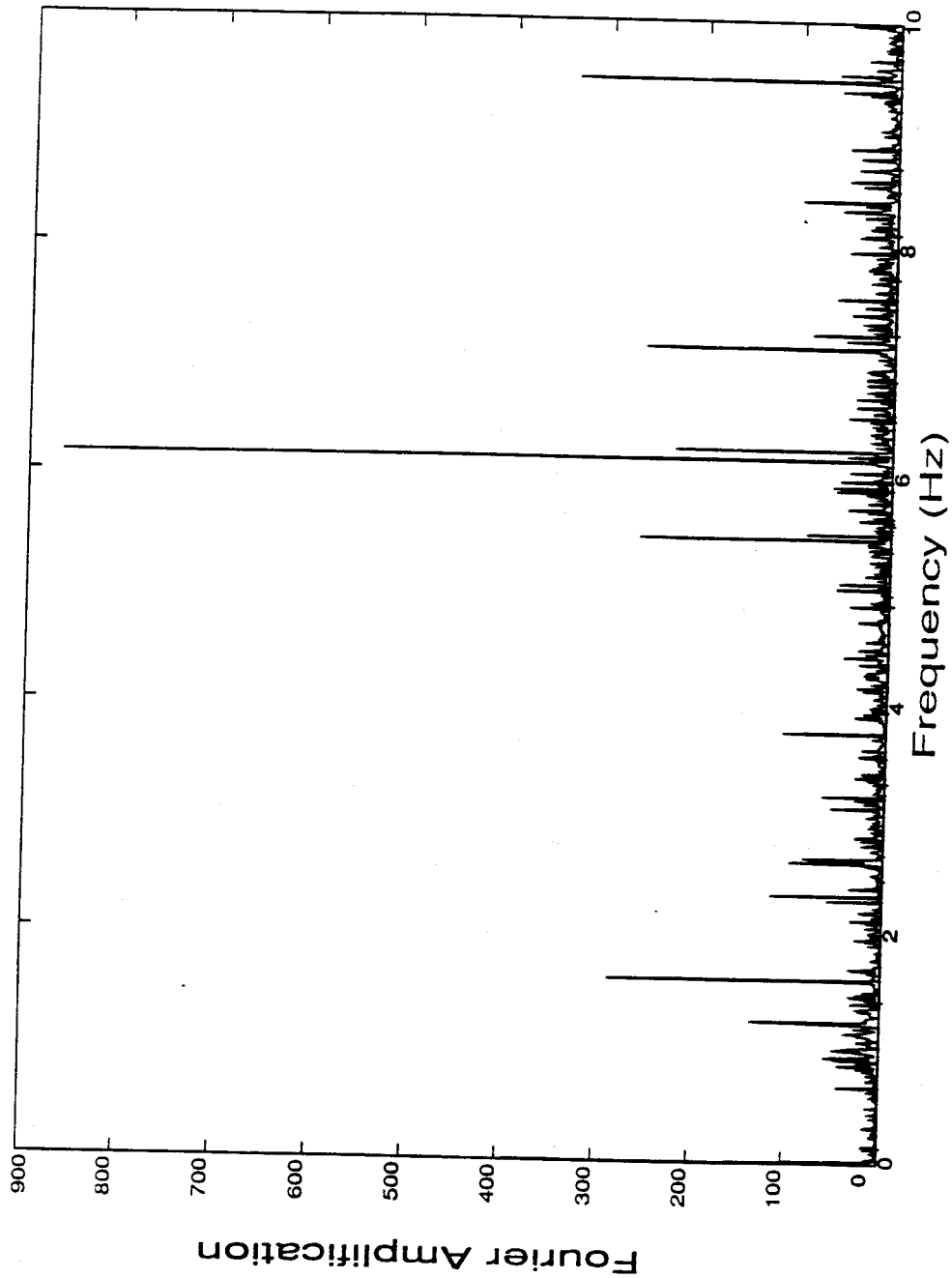

Figure 4.14 The Fourier amplification spectrum for the transverse accelerations.

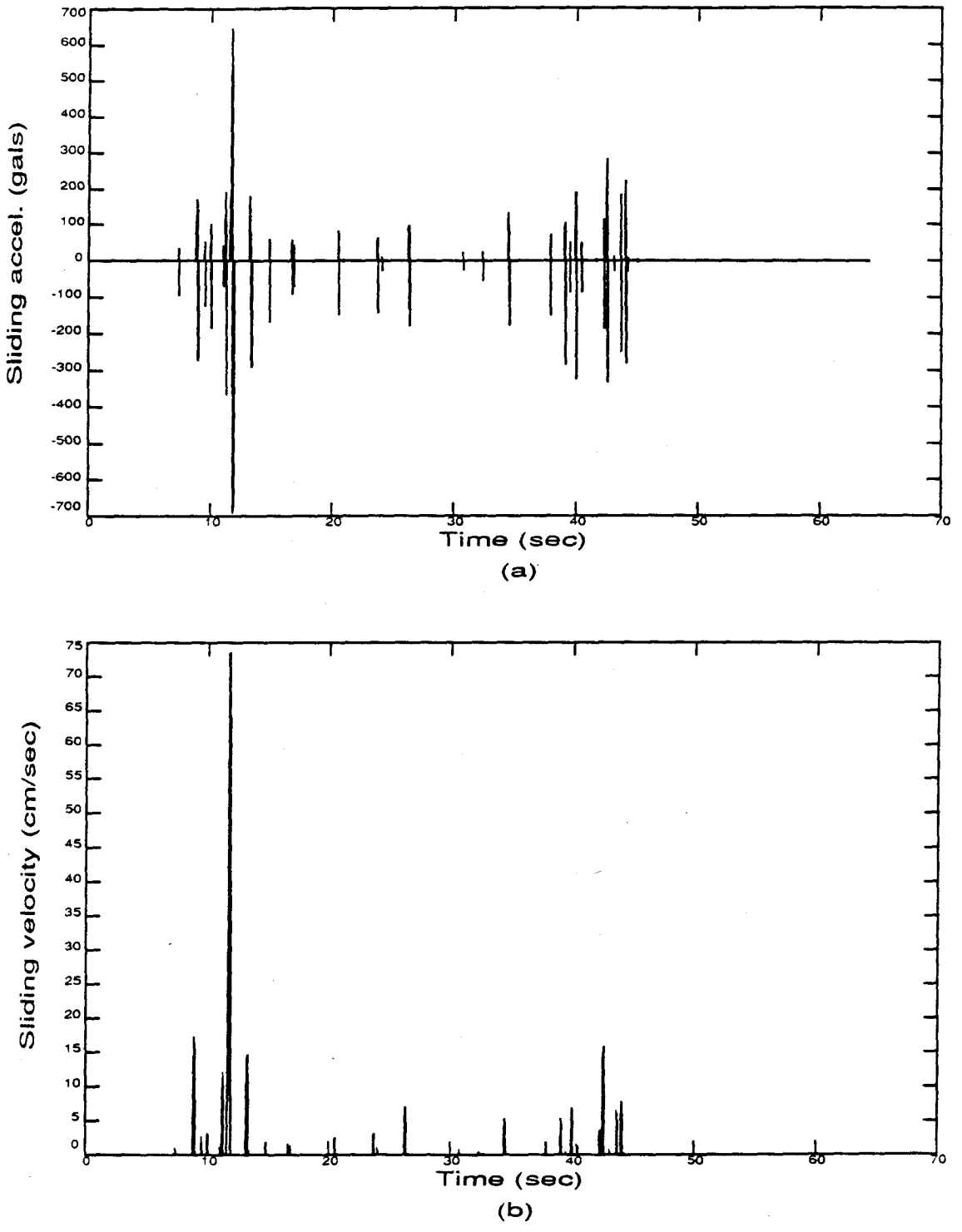

Figure 4.15 Computed motion of sliding mass using an inclined plane at $\theta = 22°$: (a) sliding acceleration (tangential); and (b) sliding velocity (tangential).

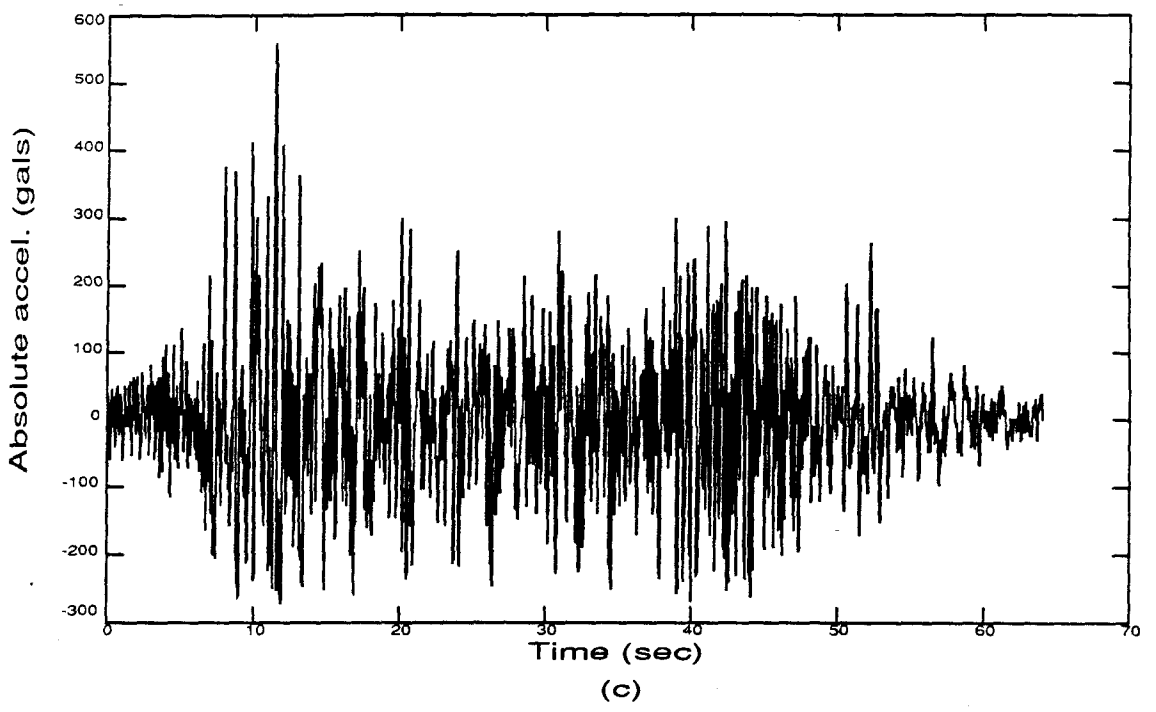

(c)

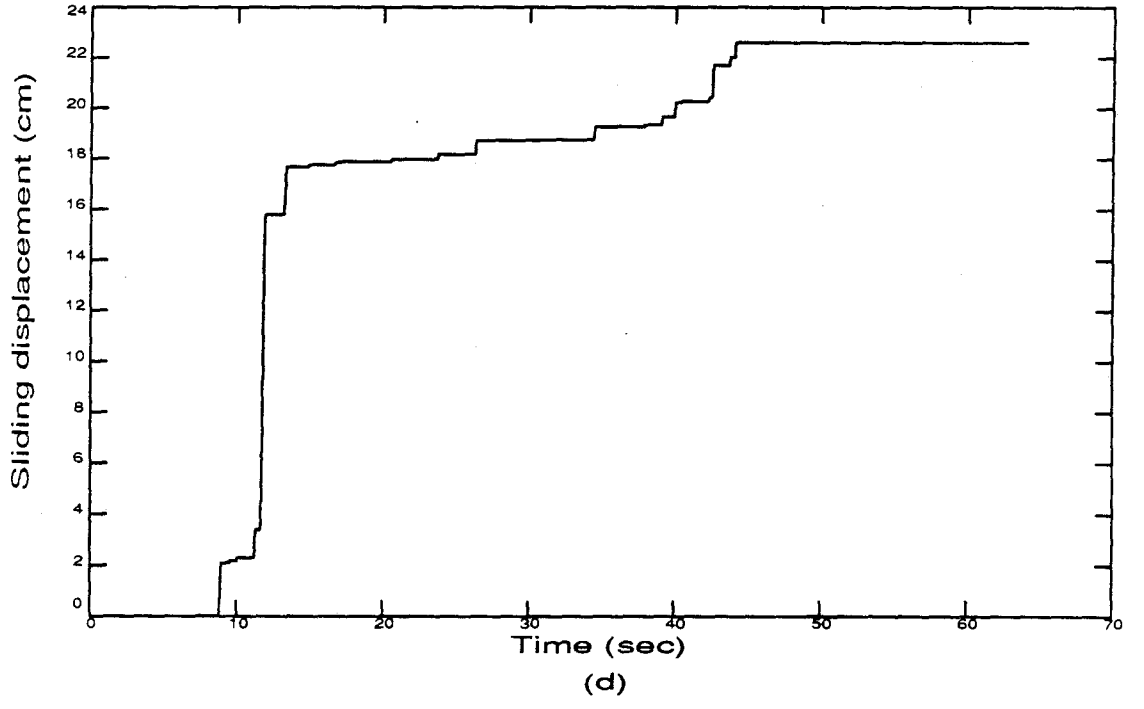

(d)

Figure 4.15 (continued): (c) absolute acceleration (horizontal); and (d) sliding displacement (tangential).

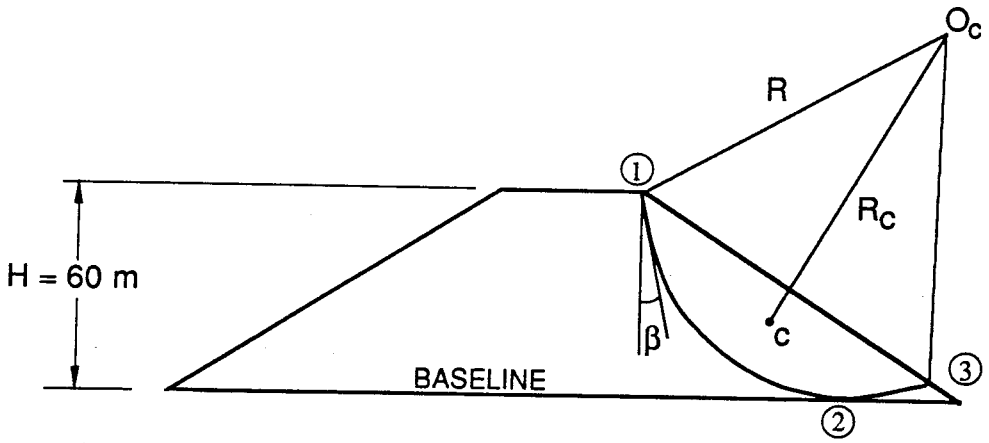

(a) Circular arc 1 assumed

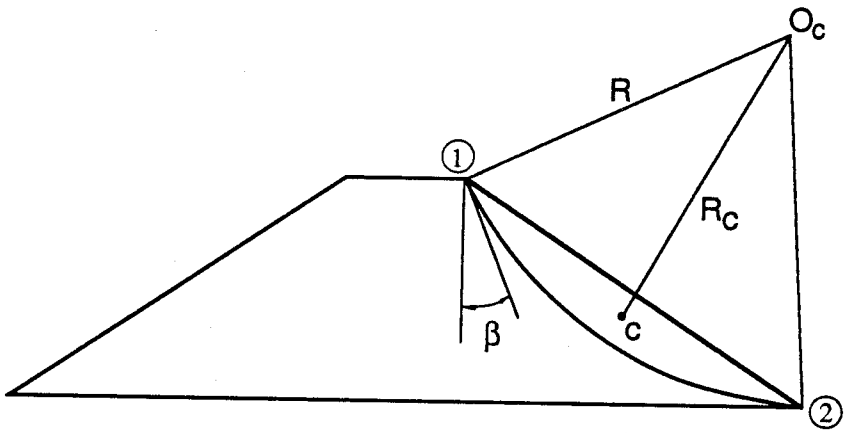

(b) Circular arc 2 assumed

Figure 4.16 La Villita Dam :
assumed circular slip surfaces (not scaled).

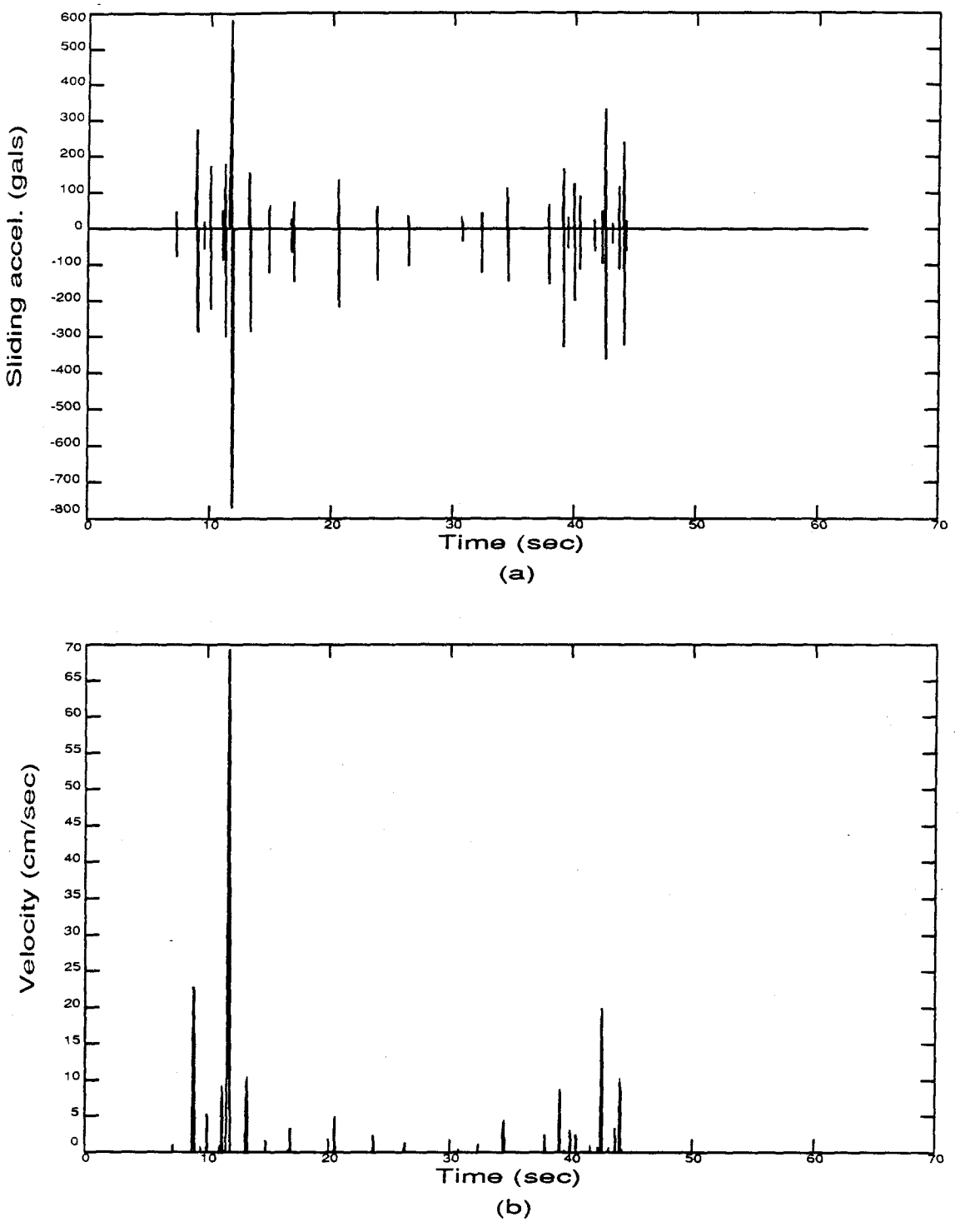

Figure 4.17 Computed motion of sliding mass at the crest using Circular arc 1: (a) sliding acceleration (tangential to slip surface); and (b) sliding velocity (tangential).

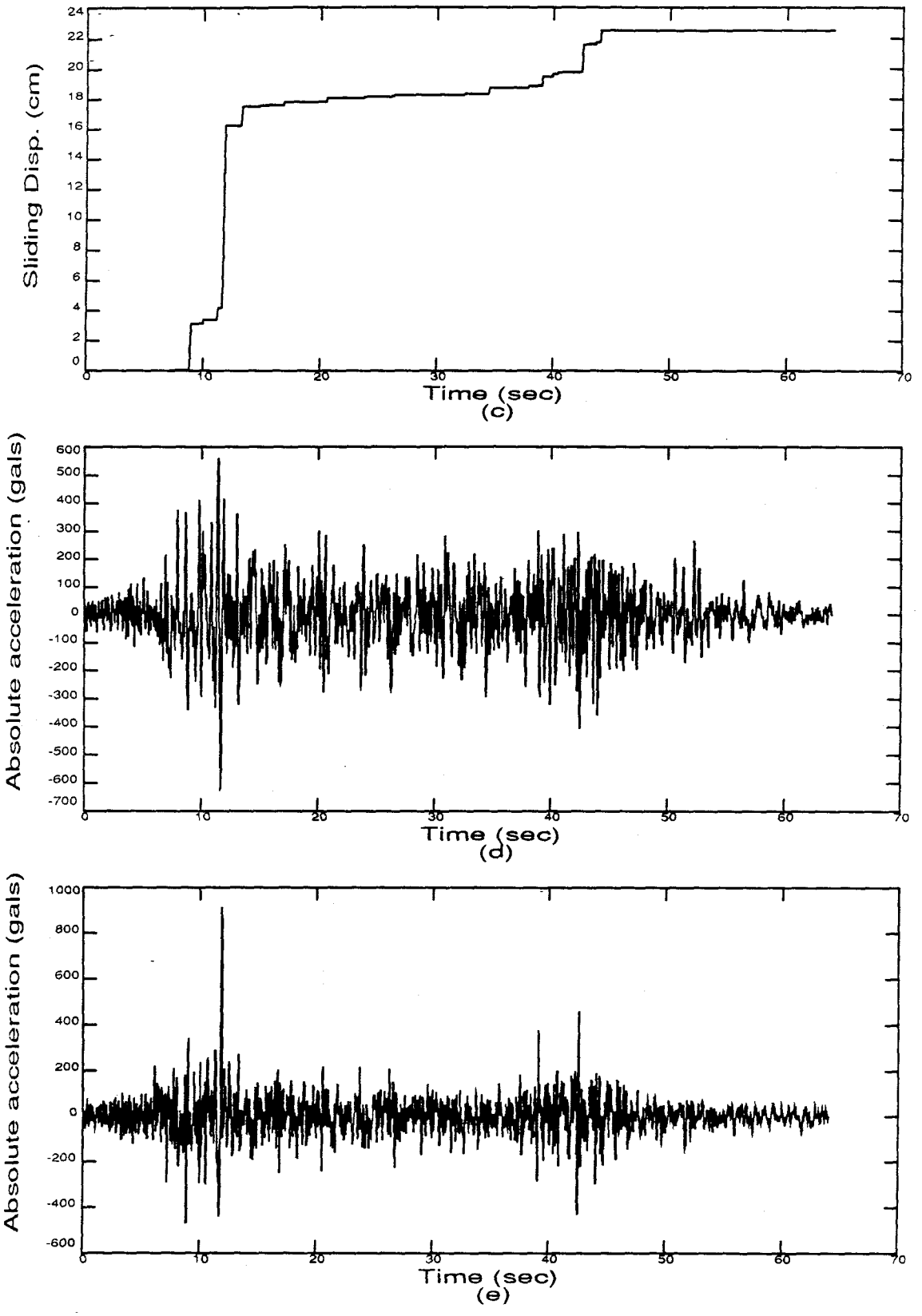

Figure 4.17 (continued): (c) sliding displacement (tangential);
(d) absolute acceleration (horizontal); and
(e) absolute acceleration (vertical).

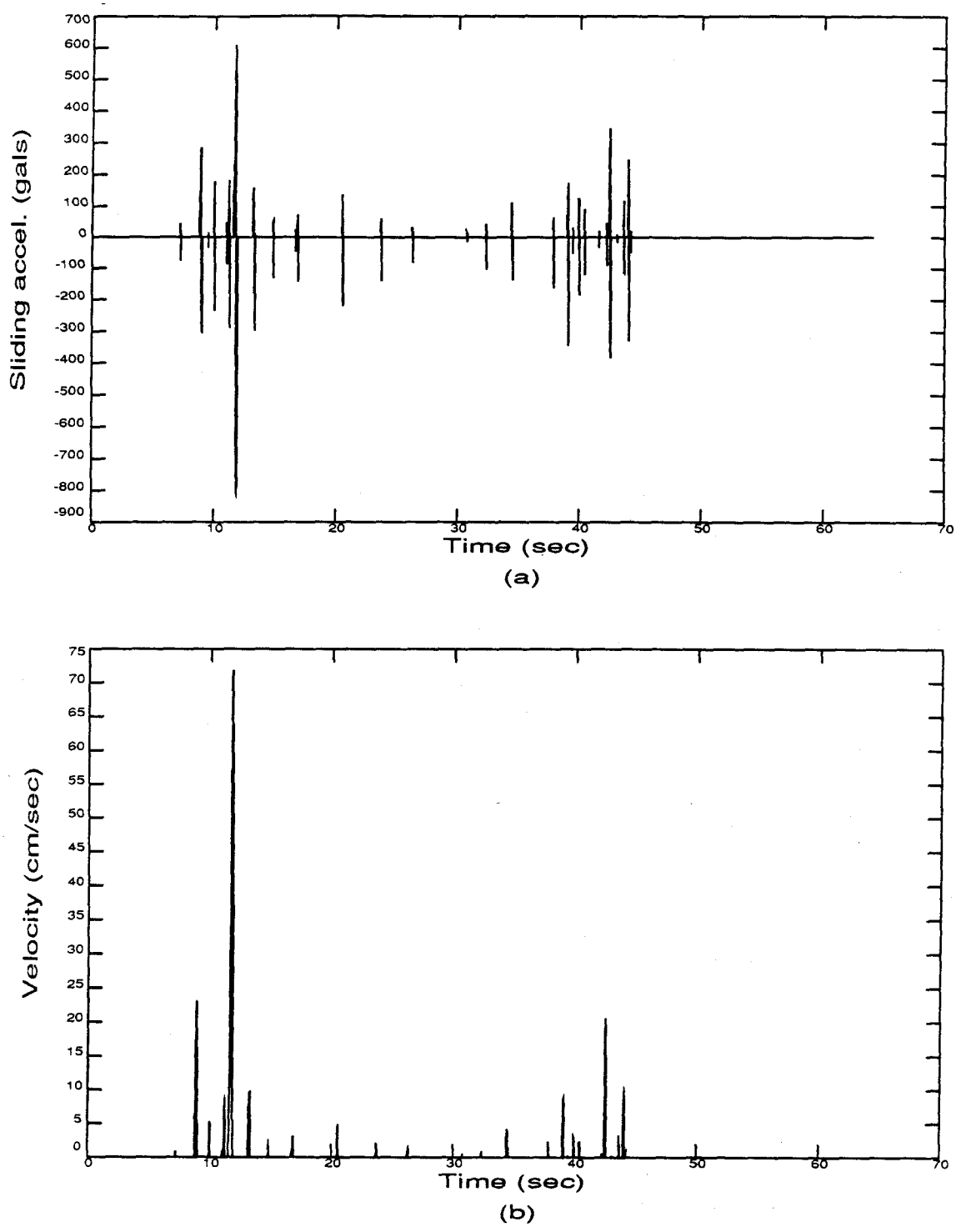

Figure 4.18 Computed motion of sliding mass at the crest using Circular arc 2: (a) sliding acceleration (tangential to slip surface); and (b) sliding velocity (tangential).

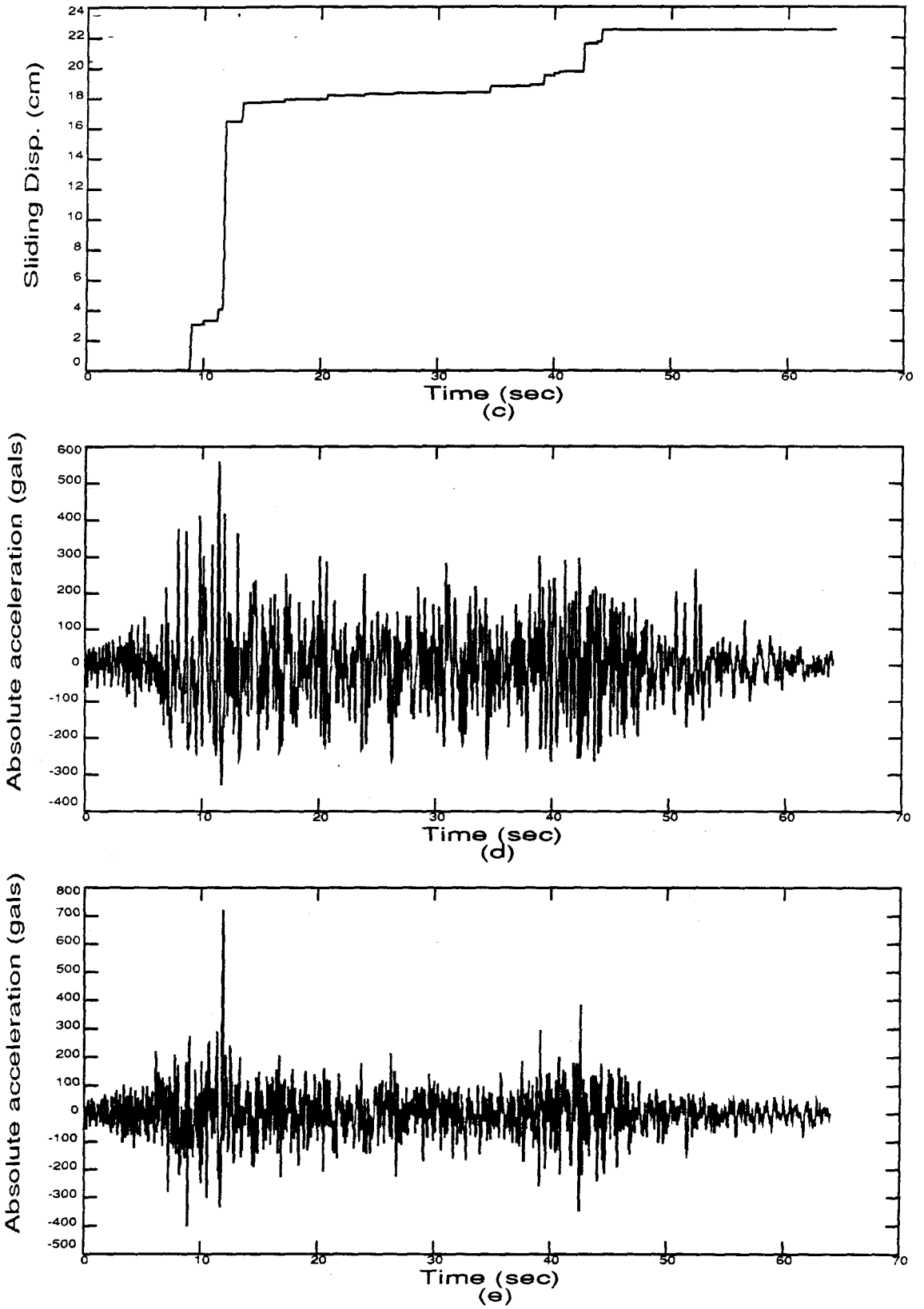

Figure 4.18 (continued): (c) sliding displacement (tangential);
(d) absolute acceleration (horizontal); and
(e) absolute acceleration (vertical).

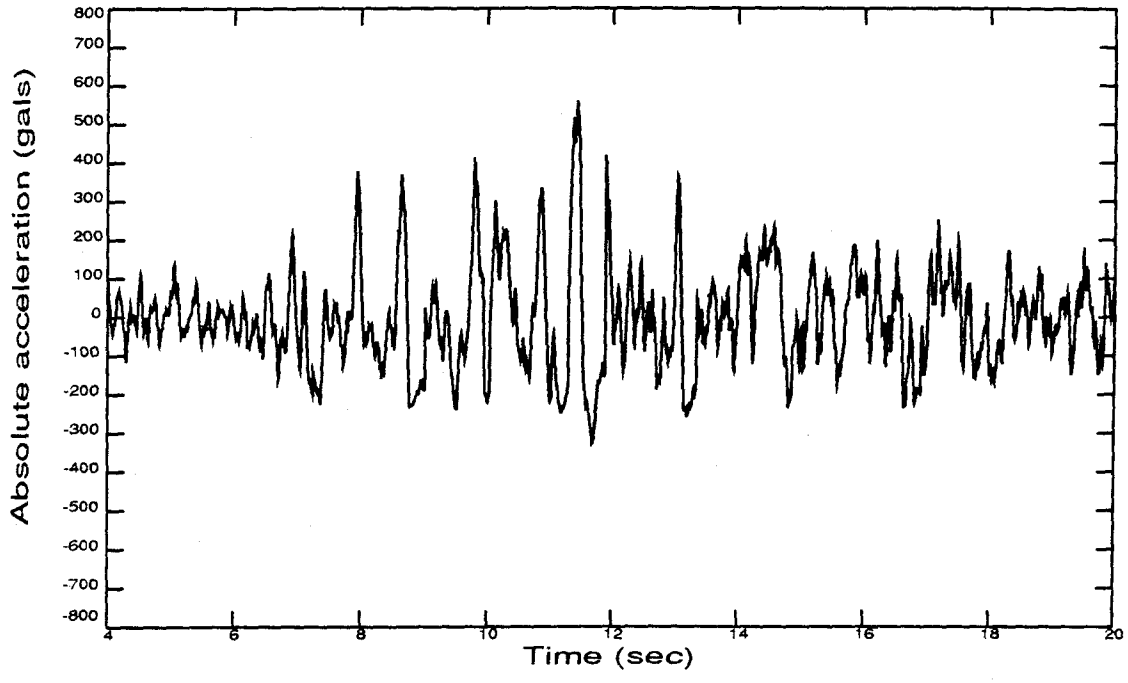

Figure 4.19 Circular arc 2 assumed: expanded absolute horizontal acceleration plot for time of interest.

Chapter 5
PRELIMINARY ANALYSIS OF EL INFIERNILLO DAM

5.1 Introduction

El Infiernillo Dam is larger than La Villita Dam. It also experienced some deformations during the September 1985 earthquake. However, there were no special indications that these were caused by sliding on a slip plane. Its behavior is much more complicated than the latter. Since it is in a relatively narrow canyon, the effect from the boundary is significant. Therefore in this chapter, only a preliminary analysis is performed and the dam is modeled in a plane strain state. More comprehensive study of a 3-dimensional analysis is needed in the future.

5.2 Background

The Federal Commission of Electricity (CFE) of Mexico in 1960 started the construction of El Infiernillo Hydroelectric Project at a site located 68 km upstream from the mouth of the Balsas River and 300 km to the SW of Mexico City (Comision Federal de Electricidad, 1985). As a part of the project,

El Infiernillo Dam was built at an approximately constant rate during a period of 15 months (August 1962 through December 1963). The dam site was selected at a place where the Balsas River flows along a south-north direction approximately; immediately downstream of the site the river makes a sharp bend toward the SW. The design took advantage of this situation to locate conveniently the various appurtenant structures as shown in the plan view of Figure 5.1.

El Infiernillo Dam is higher than La Villita Dam with a short crest length, so that its behavior is expected to be more 3-dimensional than the latter. Being located in a relatively narrow canyon, the boundary effects are significant.

5.2.1 Dam Structure

The geometric features of the structure are presented in Figure 5.2(a). The zoned fill dam is 146-m high with external slopes of 1.85:1, berms inclusive. It can be considered as a rather steep embankment since the outer shells have an average slope of 1.8:1, both upstream and downstream, and a symmetrical thin core with 0.089: 1 slopes.

The embankment has a volume of 5.5×10^6 m^3, of which 5×10^6 m^3 consist of rockfills, transitions, and filters. The dam impounds 12,000 million cubic meters of water that operates an underground powerhouse with an installed capacity of 920 MW.

The central impervious core was constructed with a clayey soil of medium to high plasticity (w_L = 49%; w_p = 29%, on the average), placed in 15-

cm thick layers with a moisture content 3% above optimum and compacted with a sheepsfoot roller to a degree of compaction of about 94% with respect to the standard proctor test. For the filters, sand extracted from alluvial deposits was used whereas rock fines resulting from underground excavations were placed in the transition zones; in both zones the material was compacted with a vibratory roller in layers 30-cm thick. Rockfill shells were constructed with the silicified conglomerates borrowed from nearby quarries, compacted in layers 1-m thick with a D-8 bulldozer. The protective rockfill was distributed with a bulldozer in 2-m thick layers.

Because this dam is located in a highly seismic zone, a freeboard of 6.5 m was adopted (the difference between crest elevation and pool level) when a flood of 28,000 m^3 per second is discharging into the reservoir.

5.2.2 Geology

Figure 5.2(b) illustrates the main geological features of the dam site. This geology is characterized by silicified conglomerates dipping 30° to the NE, at both banks. The components of this originally sedimentary formation were melted by the heat produced by an intrusion of diorite. The rock, although competent, is brittle and sensitive to blasting.

The main system of fractures is oriented north to south with an inclination of 70^{o} toward the west. Occasionally these fractures are filled with clay. Weathering is superficial to a depth varying from 1 to 2 m and it is concentrated on the higher elevations of the canyon. There exists a shear zone in the right bank between elevation 90 and 140 which had to be

excavated down to a depth of 15 m in some sections. Several basaltic dikes cross the conglomerates, one of them at the river bed, following a direction parallel to the fault system; the dykes fill some fractures of the main system.

5.2.3 Instrumentation

The instrumentation installed on the dam, part of which is shown in Figure 5.3, consists of accelerographs, inclinometers, cross-arms, extensometers and Casagrande-type piezometers. There are five 70-mm film recording accelerographs: one at the centerline of the core's crest; two on the downstream face; one 400 m downstream of the toe on the right bank; and one 240 m from the left abutment inside the underground powerhouse.

5.3 Seismic Activity at the Dam Site

Like La Villita Dam, El Infiernillo Dam is also located in the high seismicity zone associated with the subduction of the Pacific Ocean Plate under the American Continent. The site of the dam has also been subjected to many seismic events. Table 5.1 lists the earthquakes recorded in the vicinity of the dam, from 1975 to 1985. The most significant earthquakes are the same as those for La Villita Dam, which have been denoted as S_1 to S_6. The strongest earthquake in the life span of El Infiernillo Dam has been that which occurred in September 19, 1985 (S_5). Distances from the epicenters of the most significant earthquakes to the dam site are greater than those for La Villita Dam (Table 5.2). The peak accelerations recorded at El Infiernillo Dam during the occurrence of these earthquakes are also listed in Table 5.2.

The history of vertical and horizontal deformations recorded at the dam can be found in the reference (Comision Federal de Electricidad, 1985).

5.4 Effect of Earthquake of September 19, 1985

5.4.1 Seismic Damage

Cracking

The earthquake of September 19, 1985 induced the formation of two longitudinal cracks running along the entire length of the dam crest, and they coincide with the contact of the sidewalks in both parapets with the embankment, having an opening ranging from 2 to 150 mm (Figure 5.4). Two intermediate cracks also formed as well as some small transverse cracks in the vicinity of both abutments. From the observations made at open pits, it could be determined that the depth of the most conspicuous cracks was of only 30 cm.

Since no transverse cracks were observed at the crest which would have led to piping, the impervious core was not damaged by the seismic action.

Deformations

The maximum settlement caused by the earthquake was 11.8 cm recorded at the crest near the downstream side; 11.4 cm occurred near the upstream side.

The maximum horizontal displacement caused by the earthquake at upstream side of the crest was 1 cm, while 6 cm occurred at the downstream side of the crest.

The deformations that occurred are small compared with those observed at La Villita Dam.

5.4.2 Strong Motion Records

Unfortunately, of the five accelerographs installed at the site, only two operated. The accelerograms recorded during earthquake S_5 by these two accelerographs (one at the right bank founded on the abutment rock mass and the other at the berm of elevation 120 m), are shown in Figures 5.5 and 5.6. The longitudinal component for the accelerogram recorded at the right bank is not available. It is worth observing in these figures that for the records corresponding to elevation 120 m, the peak accelerations of the vertical component are almost equal to those of the transverse component (about 300 gals); furthermore, the longitudinal component (dam axis) contains the largest acceleration (about 400 gals). This contrasts to the case of La Villita Dam (Chapter 4) where the transverse accelerations were largest. The peak transverse acceleration recorded at the right bank of El Infiernillo Dam equalled to 140 gals.

5.4.3 Analysis of Records

The Fourier amplitude spectra of the recorded transverse accelerations, obtained by utilizing the FFT algorithm, are shown in Figure 5.7. The Fourier

amplification spectrum is computed by dividing the Fourier amplitude spectra of the acceleration recorded at the berm at elevation 120 m by that recorded at the right bank. Figure 5.8 shows the Fourier amplification spectrum for the transverse component. Disregarding the sharp peaks which are spurious, it is still hard to identify the fundamental frequency of dam vibration. Had the crest record been available, this identification may have been possible. Also, the motions in other than the transverse direction need to be investigated, since the fundamental mode may not be in the transverse direction.

5.5 Deformation Analysis with the Simplified Method

As shown in Figure 5.9, the slip surface is assumed to be a circular arc, which has a radius R = 110.2 m, Rc = 99.5 m, Ri = 27.7 m. It goes through the berm at Elevation 120 m and the dam crest with a sloping angle with the vertical $\beta = 27^{o}$; $\theta_o = 29.7^{o}$. Using *SLIP-C*, a two-dimensional computation has been performed. The horizontal and vertical input excitations used are the records at the berm at elevation 120 m, since this accelerograph is not on sliding mass. Table 5.3 shows sliding displacement versus value of ϕ. When ϕ is chosen to be 30.37^{o}, the time histories for the computed sliding acceleration and sliding velocity; sliding displacement, absolute transverse acceleration and absolute vertical acceleration are shown in Figures 5.10 and 5.11. All computed motions are at the dam crest, and the sliding motions are tangential to the slip surface. It is found that the sliding displacement is 13.21 cm, which is close to the recorded resultant displacement (13.24 cm).

5.6 Summary

El Infiernillo Dam had a more complicated behavior than La Villita Dam during the September 19, 1985 earthquake. In the deformation analysis, when the dam material is assumed friction angle $\phi = 30.4^{o}$. The calculated displacement agrees with the recorded one.

No comparison of the calculated acceleration history on the sliding block with measured values can be made, because of the absence of the crest record; but the transverse record exhibits the same asymmetry as observed at La Villita Dam, although this is not strongly evident in the recorded transverse acceleration at the berm (Figure 5.6(b)).

Because of the 2-dimensional nature of the analysis, whereas a more appropriate computation would involve three dimensions for El Infiernillo Dam, the analysis performed is very conservative and not representative of the real deformational conditions. However, it represents a first attempt at determining the seismically-induced deformations of the dam, and should be followed by a 3-dimensional finite element or finite difference elasto-plastic calculation.

Year	Richter magnitude				Number of annual event
	$M_S<3$	$3\leq M_S<4$	$4\leq M_S<5$	$M_S\geq 5$	
1975	1	1	4	3	9
1976	0	6	19	3	28
1977	0	8	20	7	35
1978	0	6	15	9	30
1979	0	10	56	9	75
1980	2	23	18	3	46
1981	20	55	18	4	97
1982	2	36	6	0	44
1983	0	16	1	1	18
1984	1	19	2	0	22
1985	54	210	21	4	289
Total	80	390	180	43	693

Table 5.1 Earthquakes within 100 km of El Infiernillo Dam.

Seismic event	Date	M_S	Duration (sec)	Epicentral distance (km)	Maximum acceleration (gals) recorded at		
					bedrock	elev. 120-m berm	crest
S_1	Oct. 11, 75	4.9	14.1	79	84	–	–
S_2	Nov. 15, 75	5.9	19.5	23	87	–	270
S_3	Mar. 14, 79	7.6	31.3	134	–	–	355
S_4	Oct. 25, 81	7.3	71.6	54	–	–	–
S_5	Sep. 19, 85	8.1	76.1	68	132	379	–
S_6	Sep. 21, 85	7.5	63.9	79	37	–	–

Table 5.2 Parameters of major earthquakes that have occurred in the vicinity of El Infiernillo Dam.

ϕ (degree)	29.50	30.00	30.37	31.00	32.00
Displacement (cm)	24.21	17.05	13.21	8.50	4.07
$R = 110.2$ m, $R_c = 99.5$ m, $R_i = 27.7$ m; $\theta_o = 29.7^o$, $\beta = 27^o$					

Table 5.3 Circular arc assumed: displacement vs. friction angle.

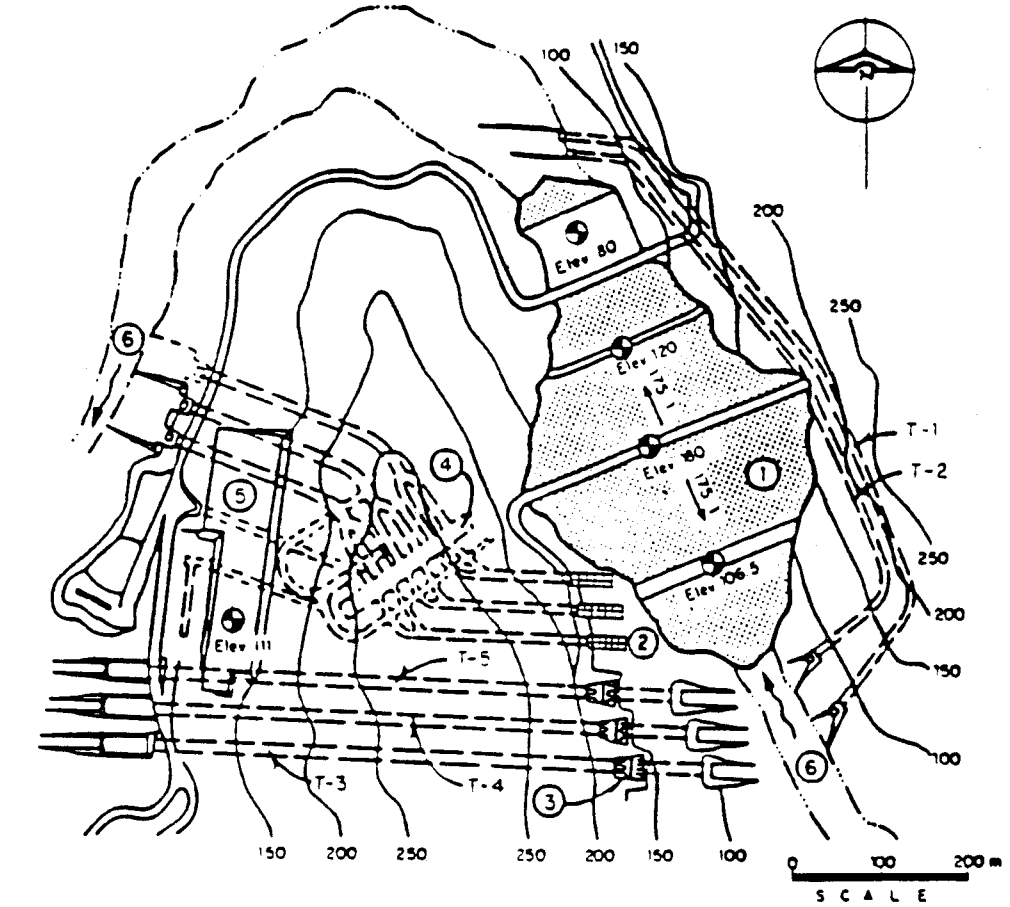

Figure 5.1 El Infiernillo Dam: plan view.

(a)

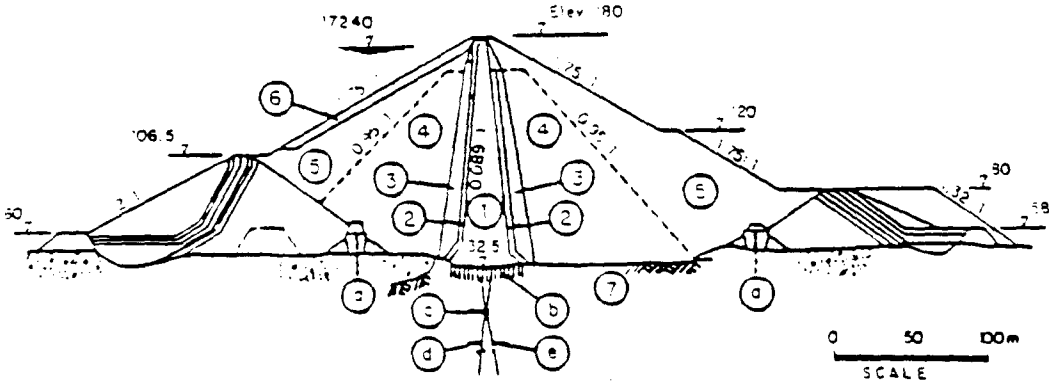

① Impervious core
② Filters
③ Transitions
④ Banded rockfill
⑤ Dumped rockfill
⑥ Riprap
⑦ Sound rock
ⓐ Concrete cut-off wall (secant piles)
ⓑ Grout blanket
ⓒ Gallery G-4
ⓓ Grout holes
ⓔ Drainage holes
Elev Elevation, in m

(b)

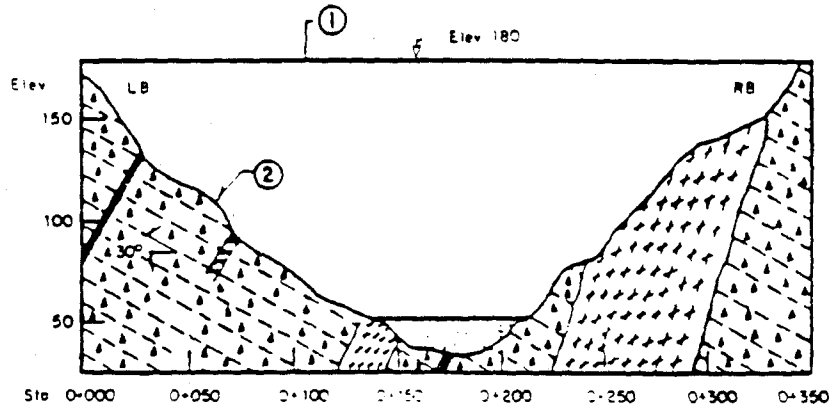

Alluvial deposit
Dike
Shear zones
Breccias and conglomerates
Basalt dike
① Dam crest
② Profile of excavated rock
RB Right bank
LB Left bank
Elev Elevation, in m
Sta Station, in m

Figure 5.2 El Infiernillo Dam: (a) maximum cross-section; and (b) geological features of the dam site.

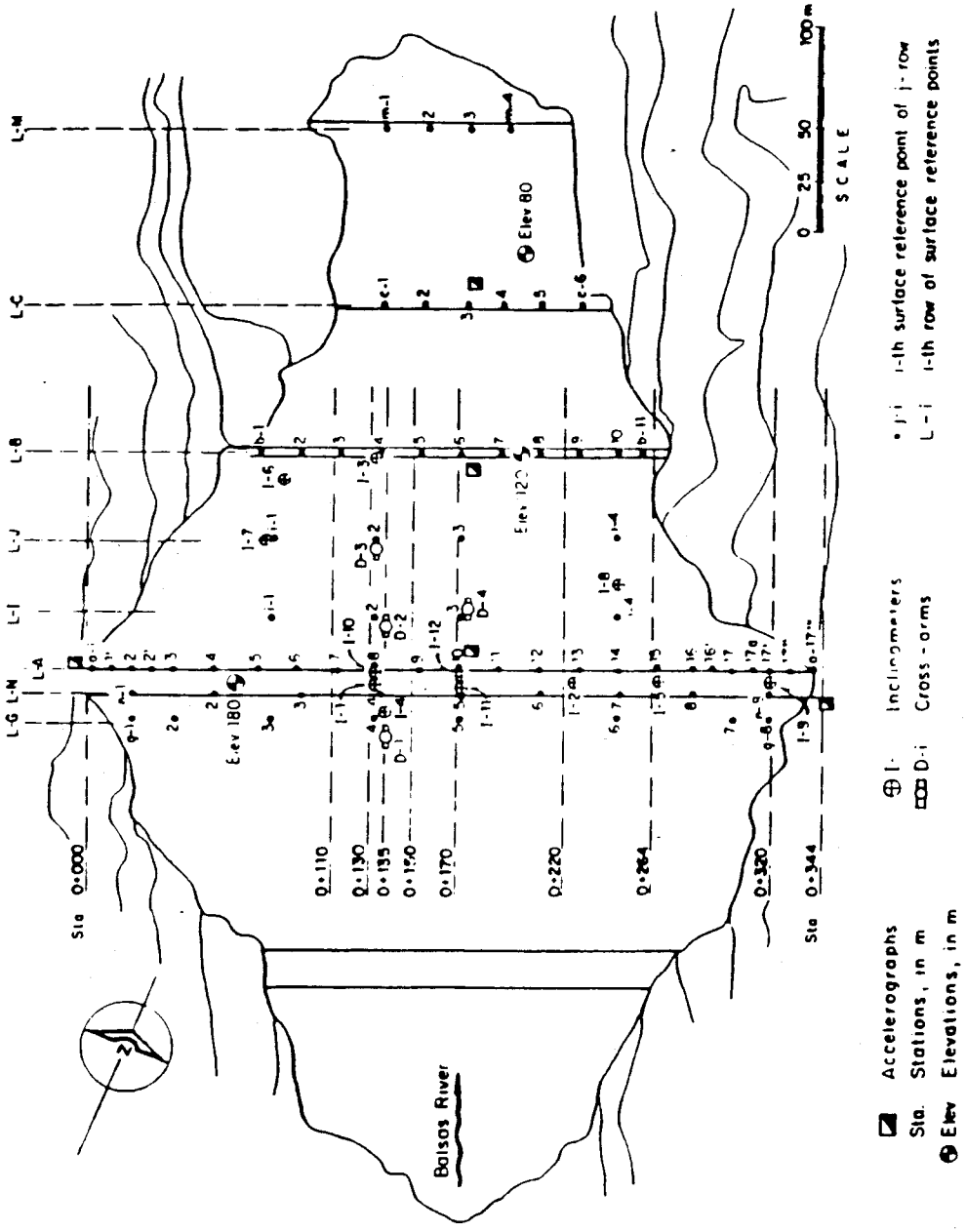

Figure 5.3 Part of the instrumentation installed on El Infiernillo Dam.

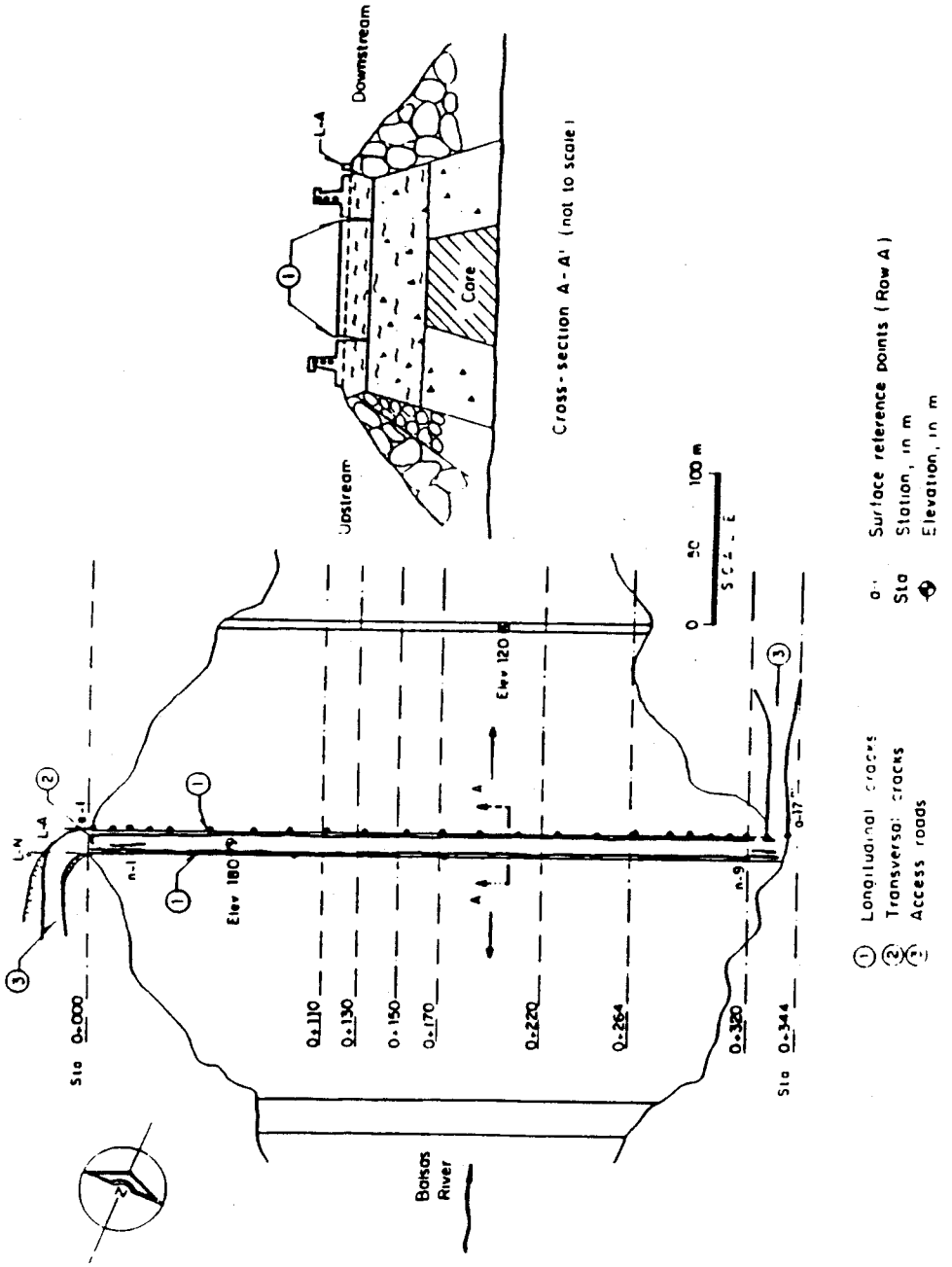

Figure 5.4 Cracks induced by the earthquake of September 19, 1985 at El Infiernillo Dam.

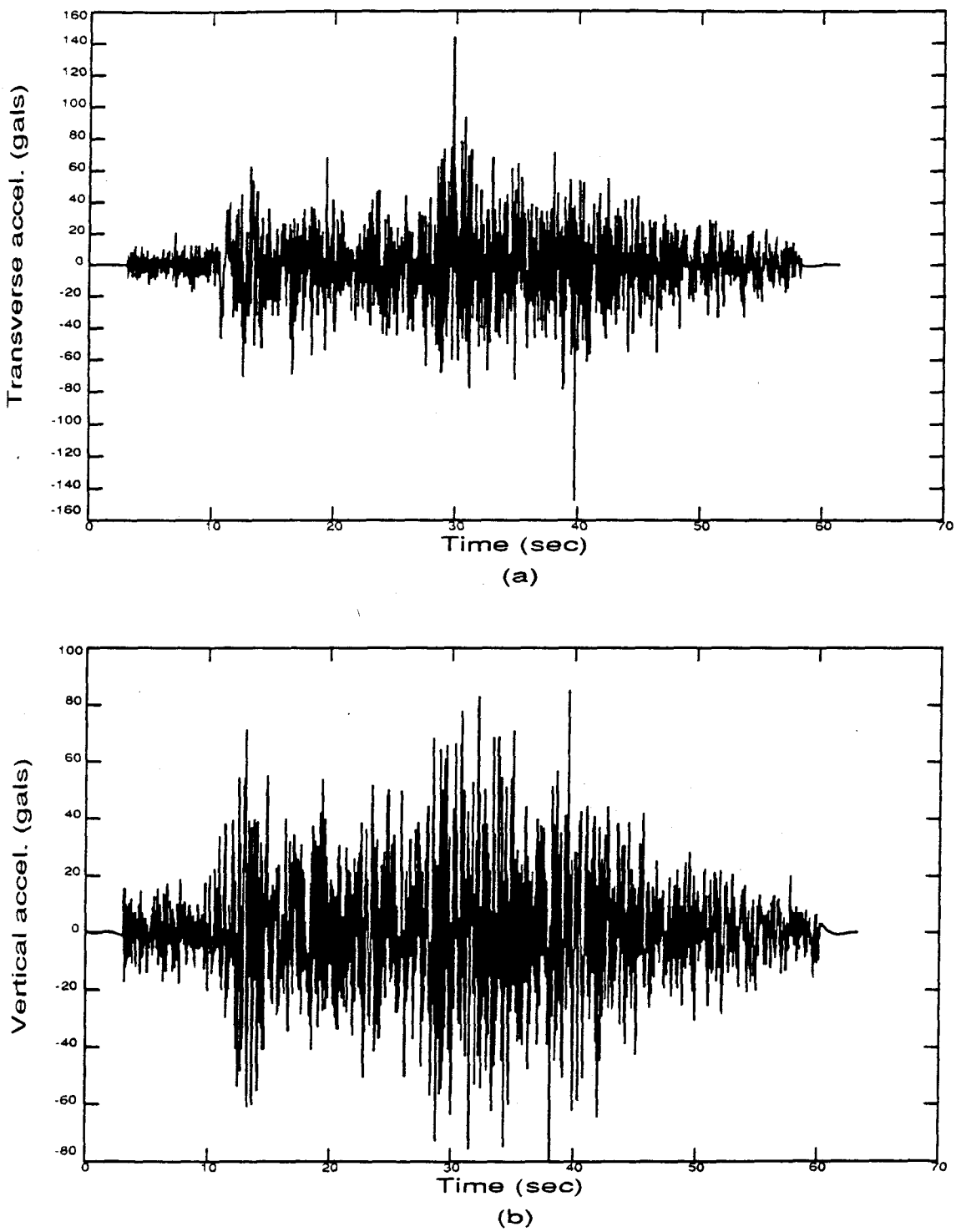

Figure 5.5 Accelerograms recorded at the right bank of El Infiernillo Dam.

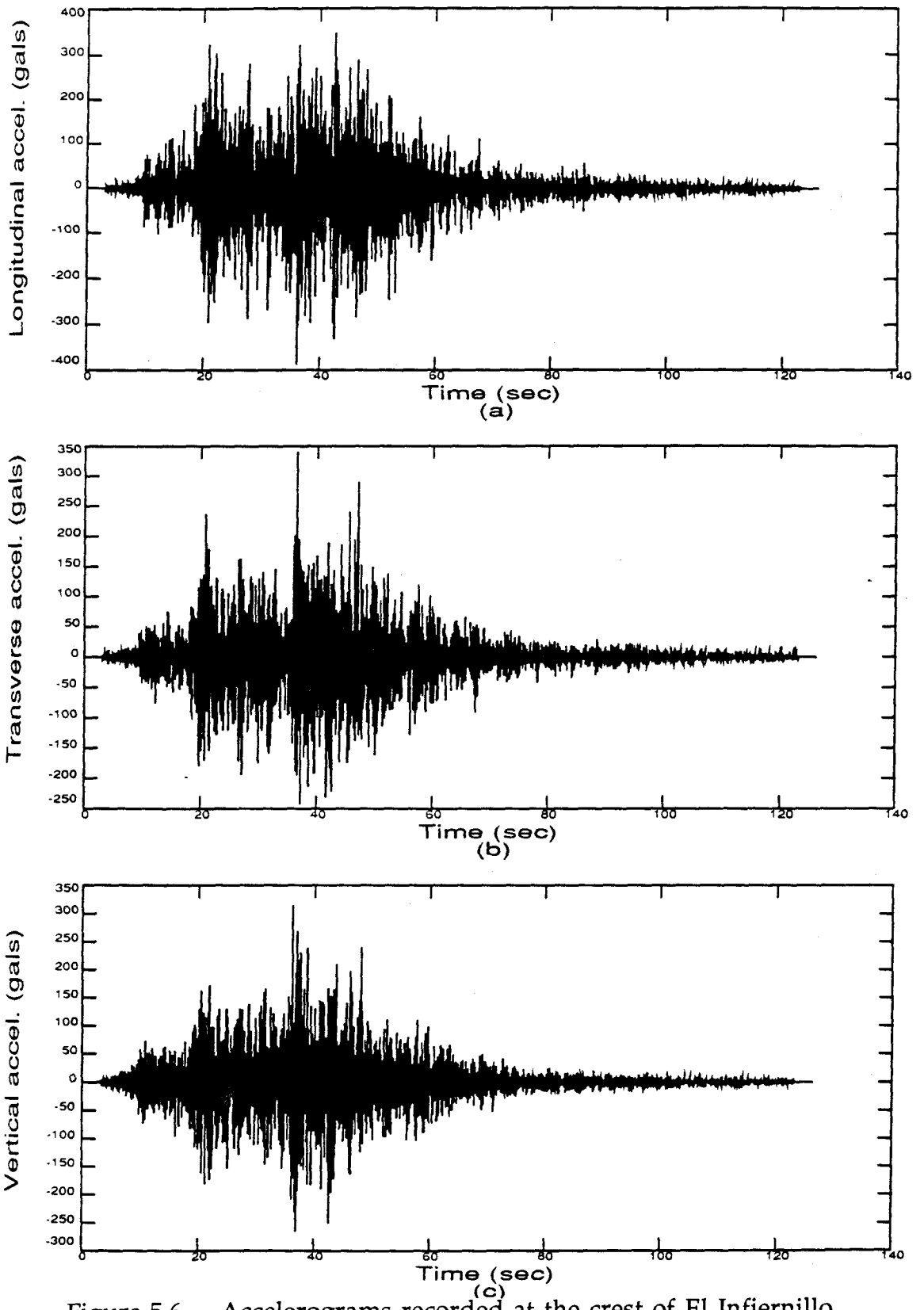

Figure 5.6 Accelerograms recorded at the crest of El Infiernillo Dam.

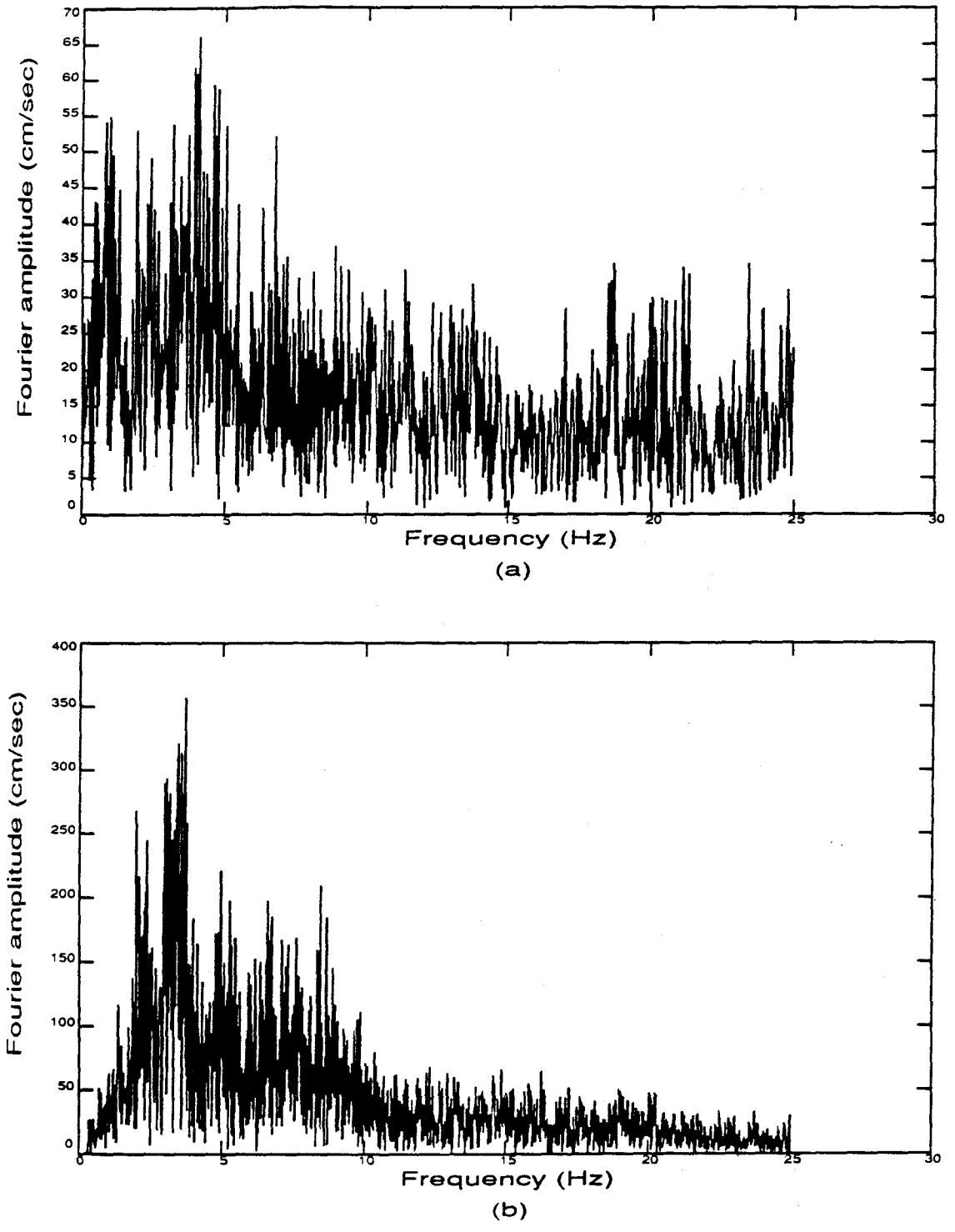

Figure 5.7 Fourier amplitude spectra for the transverse accelerations recorded at (a) the right bank; and (b) elevation 120-m berm.

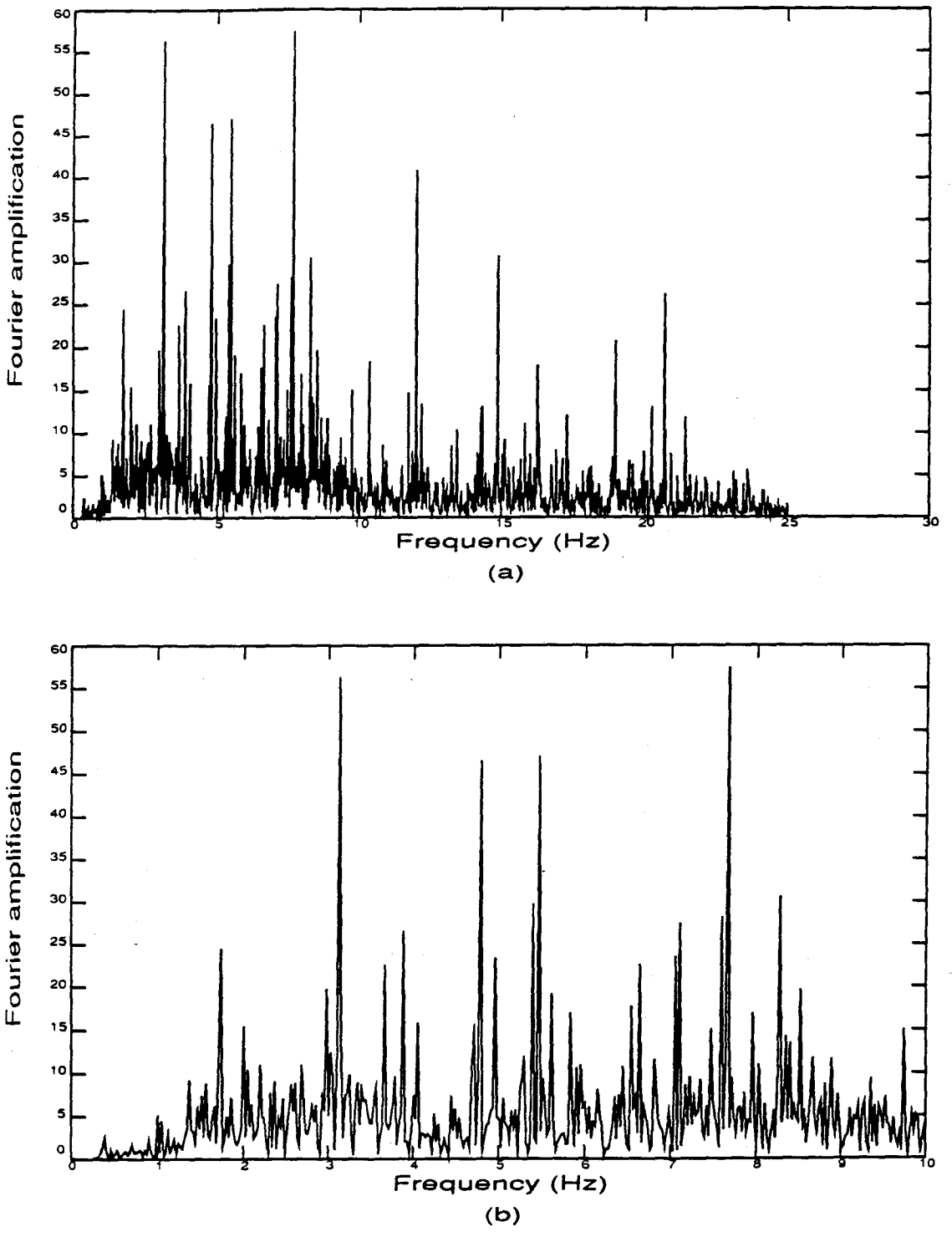

Figure 5.8 Fourier amplification spectrum for the transverse acceleration component: (a) 0 - 25 Hz; and (b) 0 - 10 Hz.

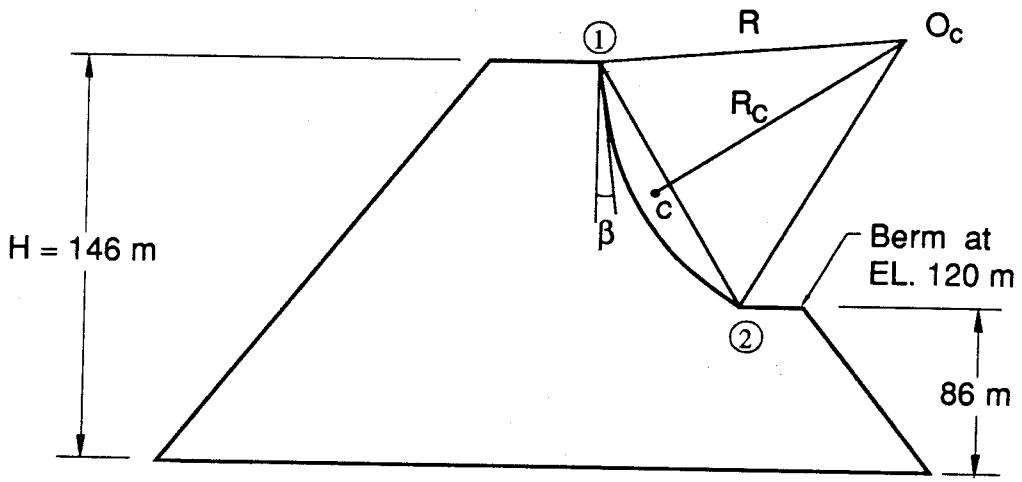

Figure 5.9 El Infiernillo Dam: assumed circular slip surface (not scaled).

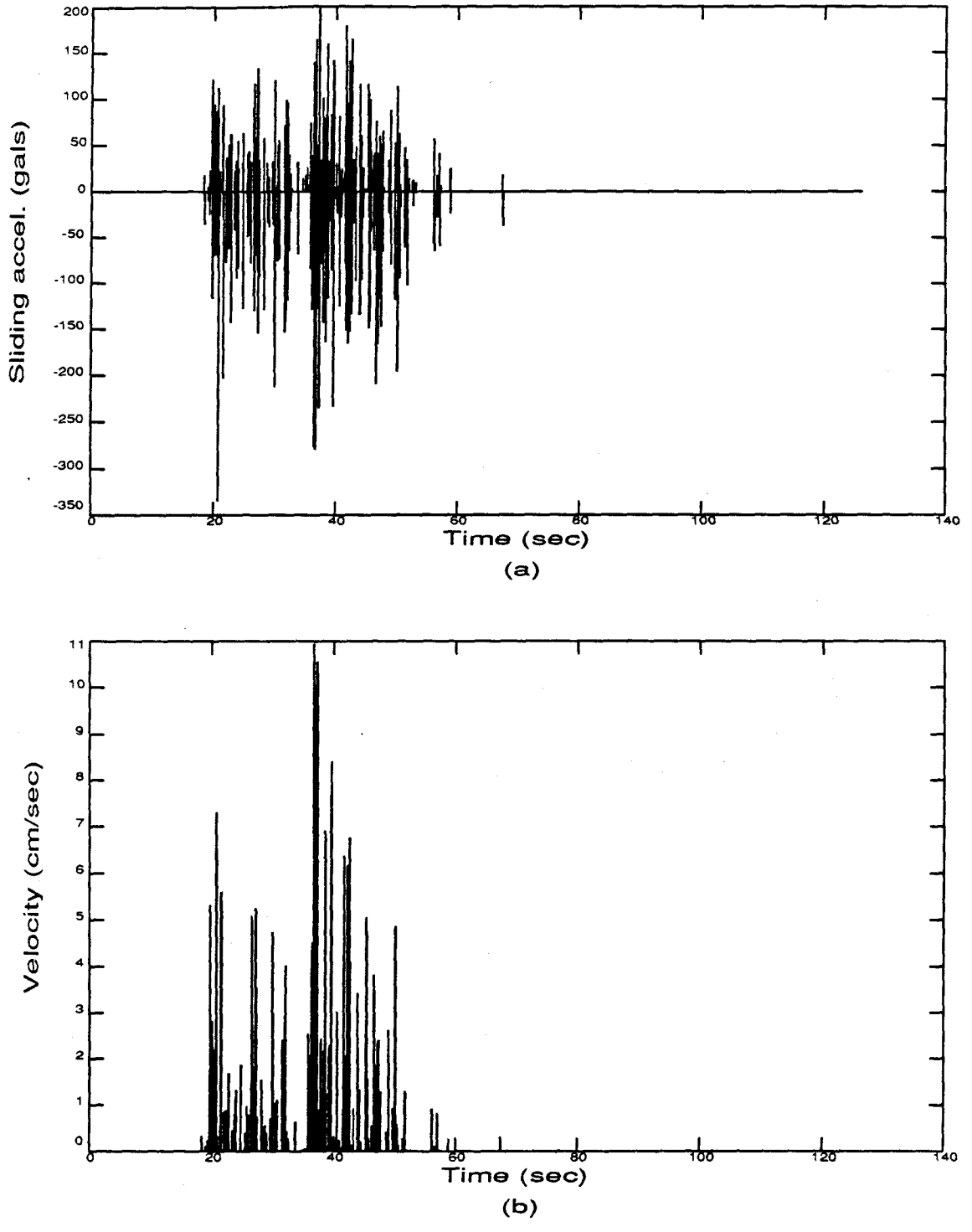

Figure 5.10 Circular arc assumed: (a) sliding acceleration; and (b) sliding velocity.

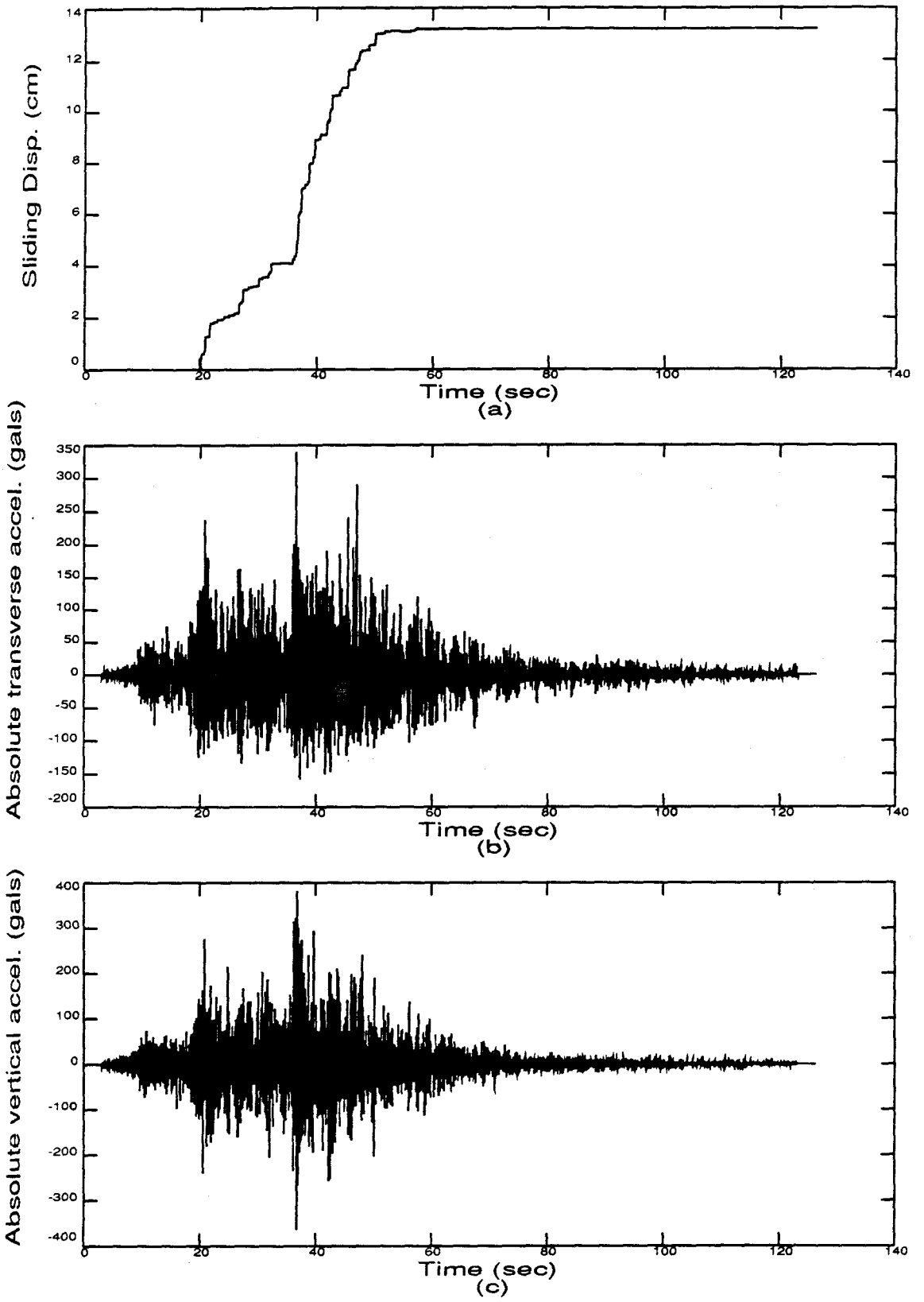

Figure 5.11 Circular arc assumed: (a) sliding displacement; (b) and (c) absolute acceleration.

Chapter 6
CONCLUSIONS AND RECOMMENDATIONS

6.1 Conclusions

The simplified method for performing seismic deformation analyses of earth dams has been extended by including vertical ground motion and a circular sliding plane. Confidence in the computational features of the numerical algorithm dealing with sliding has been achieved through comparison with shaking table tests of a rigid block sliding on an inclined plane. Results indicate that the slip displacements are sensitive to parameters of the analysis, especially friction angle, slope of slip plane, and radius of slip plane. This finding has important implications for practical application.

Sliding block analyses of La Villita Dam were able to explain to some extent the recorded displacements and accelerations there, and it has been shown that displacement of the magnitude which occurred could have resulted from a sliding mechanism. The attempt to reproduce the asymmetry in the crest acceleration records could not generate the exact number and sharpness of the observed acceleration spikes. The results indicate that the actual behavior is more complicated than what is modeled by the 2-

dimensional sliding block analysis, even with the improvements mentioned above.

Since there were no definite indications that El Infiernillo Dam underwent sliding movement, only a preliminary deformation analysis is presented. Because of the absence of a crest record and the indefinite nature of the Fourier amplification spectrum for the available transverse component in the lower part of the dam, the fundamental frequency of El Infiernillo Dam could not be identified.

6.2 Recommendations

The results of numerical simulations and shaking table tests have contributed to a better understanding of the seismic deformation behavior of earth dams. But since an earth dam is a complicated structure, more considerations are needed.

1) An earth dam's dynamic behavior largely depends on its geometry. The effect of the canyon usually results in some 3-dimensional behavior, which is not covered in the present study for a plane strain state.

2) Since sliding is very sensitive to the material properties of soil, it is very important to have a correct value of friction angle used in the model. More studies on the determination of friction angle is desired. Also the material properties of soil change during a dynamic process; therefore, there is a need to incorporate such change.

3) More complex means of assessment are needed which appropriately consider the sensitivities of the analysis to material and geometric parameters.

REFERENCES

Alfaro, J. P. and Lopez, G. C. (1986). "Estudio de Los Pulsos en Los Acelerogramas Registrados en La Corona de La Villita," Proyecto 4706, Instituto de Ingenieria, UNAM, Febrero.

Ambraseys, N. N. (1958). "The Seismic Stability of Earth Dams," Ph.D. Dissertation, University of London.

Ambraseys, N. N. (1960a). "On the Seismic Behavior of Earth Dams," Proc. 2nd World Conference on Earthquake Engineering, Tokyo, I, pp.331-354

Ambraseys, N. N. (1960b). "The Seismic Stability of Earth Dams," Proc. 2nd World Conference on Earthquake Engineering, Tokyo, II, pp.1345-1363.

Ambraseys, N. N. (1962). "The Seismic Stability Analysis of Earth Dams," Proc. 2nd Symposium on Earthquake Engineering, University of Roorkee, India.

Ambraseys, N. N. and Sarma, S. K. (1967). "The Response of Earth Dams to Strong Earthquakes," Geotechnique, Vol.17, No. 2. pp.181-213.

Bishop, A. W. (1955). "The Use of the Slip Circle in the Stability Analysis of Slopes," Geotechnique 5, No. 1, pp.7-17.

Burridge, P. B. (1987). "Failure of Slopes," Ph. D. Thesis, Report No. SML 87-01, Caltech.

Casagrande, A. (1950). "Notes on the Design of Earth Dams," Journal of Boston Society of Civil Engineering, Vol. 37, October.

Chopra, A. K. (1967). "Earthquake Response of Earth Dams," J. Soil Mech. and Found. Div., ASCE, 93.

Clough, R. W. and Chopra, A. K. (1966). "Earthquake Stress Analysis in Earth Dam," J. Engrg. Mech., ASCE, 92.

Clough, R. W. and Penzien, J. (1975). Dynamics of Structures, McGraw-Hill Publications, New York.

Comision Federal de Electricidad, (1976). "Behavior of Dams Built in Mexico," XII International Congress in Large Dams, Mexico.

Comision Federal de Electricidad, (1980). "Performance of El Infiernillo and La Villita Dams including the Earthquake of March 14, 1979," Mexico City, Mexico.

Comision Federal de Electricidad. (1985). "Behavior of Dams Built in Mexico (1974-1984)," XV Int. Congress on Large Dams, II, Lausanne, Switzerland.

Comision Federal de Electricidad. (1987). "Effects of the September 1985 Earthquakes on Dams Built on the Balsas River," Symp. on Dams and Earthquakes, Chinese National Committee on Large Dams, Beijing, China.

Cundall, P. A. (1976). "Explicit Finite Difference Methods in Geomechanics," Numerical Methods in Geomechanics (ed. C.S. Desai), New York: American Society of Civil Engineers, pp. 132-150.

Dakoulas, P. and Gazetas, G. (1985). "A Class of Inhomogeneous Shear Models for Seismic Response of Dams and Embankments," Soil Dynamics and Earthquake Engineering, Vol. 4, No. 4, pp.166-182.

Duron, Z. H. (1987). "Experimental and Finite Element Studies of a Large Arch Dam," Report No. EERL 87-02, Earthquake Engineering Research Laboratory, Caltech, Pasadena, September.

EEFIT, (1986). The Mexican Earthquake of 19 September 1985, A Field Report by EEFIT.

Elgamal, A.-W. M., Abdel-Ghaffar, A. M., and Prevost, J. H. (1984). Nonlinear Earthquake Response Analysis of Earth Dams, Princeton University, Research Report.

Elgamal, A.-W. M., Scott, R. F., Succarieh, M. F. and Yan, L.-P. (1990). "La Villita Dam Response during Five Earthquakes Including Permanent Deformation," Journal of the Geotechnical Engineering Division, ASCE, Vol. 116, No.10, October, pp. 1443-1462.

Gazetas, G. (1985). "Seismic Response of Earth Dams: Some Recent Developments," Keynote Address Presented at the 2nd International Conference on Soil Dynamics and Earthquake Engineering, 28 June/3 July.

Hall, J. F. (1982). "An FFT Algorithm for Structural Dynamics," Earthquake Engineering and Structural Dynamics, Vol. 10, pp.797-811.

Hall, J. F. and Chopra, M. (1982). "Hydrodynamic Effects in Earthquake Response of Embankment Dams," Vol. 108, No. GT4, April, pp. 591-597.

Hatanaka, M. (1955). "Fundamental Considerations on the Earthquake Resistant Properties of the Earth Dam," Disaster Prevention Research Institute, Bulletin No. 11, Kyoto University, December, pp. 1-36.

Hencher, S. R. (1981). "Friction Parameters for the Design of Rock Slopes to Withstand Earthquake Loading," Dam and Earthquake, London, pp. 79-87.

Hildebrand, F. B. (1974). Introduction to Numerical Analysis, Dover Publications, New York, pp.290-292.

Idriss. I. M., Lysmer, J., Hwang, R. and Seed H. B. (1973). QUAD-4 A Computer Program for Evaluating the Seismic Response of Soil Structures by Variable Damping Finite Element Procedures, Report No. EERC 73-16, Univ. of Calif., Berkeley.

Ishizaki, H. and Hatakeyama, N. (1962). "Considerations on the Vibrational Behaviors of Earth Dams, " Disaster Prevention Research Institute, Bulletin No. 52, Kyoto University.

Jones, N. P. and Shenton III, H. W. (1990). "Generalized Slide-Rock Response of Rigid Blocks during Earthquakes, " Pro. 4th U.S. National Conf. on Earthquake Engineering, Vol. 3, May , Palm Springs, CA, pp.31.

Kutter, B. L. (1979). "Behavior of Embankments Under Dynamic Loading," M. Phil. Thesis, Cambridge University.

Kutter, B. L. (1984). "Earthquake Deformation of Centrifuge Model Banks," Journal of the Geotechnical Engineering Division, ASCE, Vol. 110, No. 12, December, pp. 1697-1714.

Makdisi, F. I., Kagawa, T. and Seed, H. B. (1982). "Seismic Response of Earth Dams in Triangular Canyons," J. Geotech. Engrg., ASCE, 108, GT10, pp.1328-1337.

Makdisi, F.I . and Seed, H. B. (1978). "Simplified Procedure for Estimating Dam and Embankment Earthquake-Induced Deformations," Vol. 104, No. GT7, July, pp.849-867.

Martin, G. R. (1965). "The Response of Earth Dams to Earthquakes," Ph.D. Thesis, University of California at Berkeley, CA.

Medvedev, S. V. and Sinitsym, A. P. (1965). "Seismic Effects on Earth Fill Dams," Proc. 3rd World Conf. on Earthquake Engrg., New Zealand, Paper IV/M/18.

Mejia, L. H., Seed, H.B. and Lysmer, J. (1982). "Dynamic Analysis of Earth Dam in Three Dimensions," J. Geotech. Engrg., ASCE, Vol. 108. GT12, pp.1586-1604.

Mejia, L. H. and Seed, H. B. (1983). "Comparison of 2-D and 3-D Dynamic Analyses of Earth Dams," Journal of Geotechnical Engineering, ASCE, Vol. 109, No. 11, November, pp.1383-1398.

Mononobe, N., Takata, A. and Mutumura, M. (1936). "Seismic Stability of the Earth Dam," Proc. 2nd Congress on Large Dams, Washington D.C., IV, pp. 435-442.

Morgenstern, N. R. and Price, V. E. (1965). "The Analysis of the Stability of General Slip Surfaces," Geotechnique 15, No. 1, pp.79-93.

Naylor, D. J., Pande, G. N., Simpson B. and Tabb R. (1981). Finite Elements in Geotechnical Engineering, Pineridge Press, Swansea.

Newmark, N. M. (1959). "A Method of Computation for Structural Dynamics," Journal of the Engineering Mechanics Division, ASCE, Vol. 85, No. EM3, July, pp.67-94.

Newmark, N. M. (1965). "Effects of Earthquakes on Dams and Embankments," Geotechnique 15, No. 2, pp.139-160.

Oden, J. T. and Martins, J. A. C. (1985). "Models and Computational Methods for Dynamic Friction Phenomena," Computer Methods in Applied Mechanics and Engineering, 52, pp.527-634.

Prevost, J. H. (1985a). "A Simple Plasticity Theory for Frictional Cohesionless Soils," Soil Dynamics and Earthquake Engineering, Vol. 4. No.1, pp. 9-17.

Prevost, J. H., Abdel-Ghaffar, A. M., and Lacy, S. J. (1985b). "Nonlinear Dynamic Analyses of an Earth Dam, A Comparative Study," Journal of Geotechnical Engineering, Vol. 111, No. 7, July, pp. 882- 897.

Prevost, J. H. and Hughes T. J. R. (1981). "Finite-Element Solution of Elastic-Plastic Boundary-Value Problems," Journal of Applied Mechanics, 48, 69-74.

Qian, G. (1989). The Great China Earthquake, Foreign Languages Press, Beijing, China,

Roth, W. H., Scott, R. F. and Cundall, P. A. (1986). "Non-linear Dynamic Analysis of a Centrifuge Model Embankment," Proc. 3rd US Nat. Conf., Charleston. Earthquake Engineering Research Institute. August 24-28, Vol. I, , pp. 505-516.

Scott, R. F. (1971). "San Fernando Earthquake, 9 February 1971 Preliminary Soil Engineering Report," Engineering Features of the San Fernando Earthquake, February 9, 1971, (Paul C. Jennings, Editor), EERL 71-02, Caltech, June , pp. 299-331.

Seed, H. B. (1966). "A Method for Earthquake Resistant Design of Earth Dams," Journal of the Soil Mechanics and Foundations Division, ASCE, Vol.94, No. SM1, Proc. Paper 4616, Jan., pp.13-41.

Seed, H. B. (1979). "Considerations in the Earthquake-Resistant Design of Earth and Rockfill Dams," Geotechnique 29, No. 3, pp.215-263.

Seed, H. B. and Goodman, R. E. (1967). "Earthquake Stability of Cohesionless Soils," Journal of the Soil Mechanics and Foundations Division, ASCE, Vol. 90, No. SM6, November, pp. 43-73.

Seed, H. B., Idriss, I. M., Lee, K. L., and Makdisi, F. I. (1975a). "Dynamic Analysis of the Slide in the Lower San Fernando Dam during the Earthquake of February 9, 1971, " Geotechnical Engineering Division, ASCE, Vol. 101, No. GT9, September, pp. 829-357

Seed, H. B., Idriss, I. M., Lee, K. L., and Makdisi, F. I. (1975b). "The Slides in the San Fernando Dams during the Earthquake of February 9, 1971," Journal of the Geotechnical Engineering Division, ASCE, Vol. 101, No. GT9, July, pp. 651-689.

Seed, H. B., Lee, K. L. and Idriss, I. M. (1969). "Analysis of Sheffield Dam Failure," Journal of the Soil Mechanics and Foundations Division, ASCE, Vol.95, No. SM6, Proc. Paper 6906, Nov. , pp. 1453-1490.

Seed, H. B. and Martin, G. R. (1966). "The Seismic Coefficient in Earth Dam Design," J. Geotech. Engrg., ASCE, 92.

Sherard, J. L. (1986). "Hydraulic Fracturing in Embankment Dams," J. Geotech. Engrg., ASCE, 112(10), pp.905-927.

Sherard, J. L., Woodward, J. R., Gizienski, S. F., and Clevenger, W. A. (1963). Earth and Earth-Rock Dams--Engineering Problems of Design and Construction. John Wiley and Sons, Inc., New York.

Shibata, H. (1984). "Use of Shaking Table for Piping and Equipment, and Selection of Input Motions," Proc. of International Workshop on Earthquake Engineering, B-14, March, Shanghai, China.

Yan, L.-P. (1989). Report for the Course of CE180, Experimental Methods in Earthquake Engineering, May, Caltech, Pasadena.

Zhang, K. X. and Tamura, C. (1984). "Influence of Dam Materials on the Behavior of Earth Dams during Earthquakes," in Report of Japan-China Cooperative Research on Engineering Lessons from Recent Chinese Earthquakes including the 1976 Tangshan Earthquake (Part 2), edited by Tamura, C., Okada, T., Katayama, T. and Tatsuoka, F., Institute of Industrial Science, University of Tokyo, September.

Zienkiewicz, O. C., Leung, K. H., Hinton, E. and Chang, C. T. (1980). "Earth Dam Analysis for Earthquakes: Numerical Solution and Constitutive Relations for Non-linear (Damage) Analysis," Design of Dams to Resist Earthquake, ICE, London, pp.141-156.